

**Analysis of $p\bar{p}$ annihilation at rest into
 $K_S K^\pm \pi^\pm$**

Technical Report Mark Lakata

Abstract

We report on an analysis of the reaction $p\bar{p} \rightarrow K_S K^\pm \pi^\pm$, with data taken by the Crystal Barrel with the kaonic trigger of April 1996. The final dalitz plot contains 60K events, much larger than the combined statistics of all previous experiments. The partial wave analysis uses P and S -wave annihilation. Contributions from $a_0(980)$, $a_0^\pm(1450)$, $K_2^*(1430)$ and $\rho(1450, 1700)$ are discussed. If the well-known $K_2^*(1430)$ is included in the fit, it perfectly recreates the $K\bar{K}$ threshold enhancement without an explicit resonance, i.e. the $a_0(980)$ is no longer needed. A $I = 1$ resonance is suggested at roughly $m = 1500$ MeV, but the spin is not well determined, so it may be either $\rho(1450)$ or $a_0(1450)$.

Contents

1	Introduction	4
2	Physics background	6
2.1	$p\bar{p}$ Annihilation at rest	6
2.2	Capture and Cascade in Hydrogen	6
2.3	Isobar model	7
2.4	The reaction $K_S K^\pm \pi^\pm$	7
2.5	Particles, Quantum Numbers and Selection Rules	8
2.5.1	Final-state particles	8
2.5.2	Intermediate state isobar particles	8
2.6	$p\bar{p}$ Initial states	9
2.7	Isospin and C -Parity Considerations	9
2.8	Kaon decays	10
2.9	Connecting initial $p\bar{p}$ states with isobar states	11
2.10	A discussion of the states used in the partial wave analysis	12
2.11	Resonances expected in $K_S K^\pm \pi^\pm$	13
2.11.1	$K^*(892)$ resonance	13
2.11.2	$K - \pi$ S wave	14
2.11.3	$K_2^*(1430)$	15
2.11.4	$a_0(980)$	15
2.11.5	$a_0(1450)$	17
2.11.6	$\rho(1450)$ and $\rho(1700)$	17
2.11.7	$a_2(1660)$	17
2.11.8	$K^*(1410)$	18
3	Software tools	19
3.1	cb1b1++	19
3.2	Vertex Fit	19
3.2.1	Introduction	19
3.2.2	TCVRHX	20
3.2.3	TCVER3	20
3.2.4	Hit Error Scaling	22
3.3	KinFit - General Kinematic Fitter	26
3.4	awp - Partial Wave Analysis	26
4	Data Selection	28
4.1	K_S Trigger	28
4.2	Reconstruction and Skimming Stage	30
4.2.1	Reconstruction Performance	30
4.2.2	Skimming cuts	30
4.3	Energy and momentum selection	34
4.3.1	Statistics	34
4.4	Vertex fitting	36
4.4.1	Statistics	38

4.5	Particle identification using Energy Loss (dE/dx)	38
4.5.1	$K_S K_L X^0$	38
4.5.2	$K_S K_S X^0$	38
4.5.3	$K_S K^\pm X^\mp$	40
4.5.4	dE/dx Theory	40
4.5.5	Corrections applied to data	41
4.5.6	Corrections applied to Monte Carlo	41
4.5.7	Curves used for Particle Identification	41
4.5.8	Particle Identification Logic	42
4.6	Corrections	44
4.6.1	Run by run momentum scaling	44
4.6.2	Error scaling	44
4.6.3	Energy loss Correction	46
4.6.4	JDC geometrical distortion	46
4.7	Kinematic Fit	50
4.7.1	Introduction	50
4.7.2	Reconstruction Accuracy	51
4.7.3	π^0 Suppression	53
4.8	Charge symmetry	53
5	Monte Carlo Simulation	58
5.1	Channels simulated	58
5.2	Parameters of the Monte Carlo	58
5.2.1	Vertex position	59
5.3	Background Estimation	60
5.3.1	$K_S K^\pm \pi^\mp$ ($K\pi$ swapped)	60
5.3.2	$K_S K_S [\pi^0]$	60
5.3.3	$K_S [K_L] \pi^\pm \pi^\mp$	61
5.3.4	$K\pi K_S [\pi^0]$	61
5.3.5	$4\pi^\pm [\pi^0]$	61
5.3.6	$K_S K_S [\eta]$	61
5.3.7	$K_S K_S$	61
5.4	Acceptance Correction	62
6	Absolute branching ratio measurement	66
7	Partial Wave Analysis	68
7.1	Introduction to Partial Wave Analysis	68
7.1.1	Dalitz plot	68
7.2	The total intensity	70
7.3	The matrix element	70
7.4	The Zemach formalism	71
7.5	Two-body breakup momentum and phase space	75
7.6	Angular barrier factor	75
7.7	Dynamical functions $\hat{T}_r(m)$	75
7.7.1	Breit-Wigner	76
7.7.2	K -matrix	77
7.8	Fit algorithm	78
7.9	The reduced χ^2	78
7.10	Results	78
7.10.1	Standard Fit	79

8	Discussion	86
8.1	Systematic errors	86
8.1.1	Masses and widths	86
8.1.2	Goodness of fit	86
8.1.3	Toy Monte Carlo and branching ratios	87
8.2	The $K\pi$ wave	87
8.2.1	The $K\pi$ wave: The strange vector $K^*(892)$	87
8.2.2	The $K\pi$ wave: The strange tensor $K_2^*(1430)$	89
8.2.3	The $K\pi$ wave: The scalar $K_0^*(1430)$	91
8.2.4	Ratio of charged to neutral strange resonances	91
8.3	The $K\bar{K}$ wave	91
8.3.1	Is there an second isovector? Is there <i>any</i> isovector?	92
8.3.2	Where is the second isovector, $a_0(1450)$?	92
8.3.3	The Crystal Barrel Analysis of $K_L K^\pm \pi^\mp$	92
8.3.4	The OBELIX Analysis	93
8.3.5	Comparisons to $K_L K^\pm \pi^\mp$ and OBELIX	93
8.3.6	Two solutions, One χ^2 Minimum	94
8.3.7	3S_1 versus 1S_0	96
8.3.8	$a_2(1320)$	98
8.3.9	The Branching ratio of $a_0(980) \rightarrow K\bar{K}$	98
8.4	Branching Ratios from $p\bar{p}$	100
8.4.1	Determination of $f_0(1500) \rightarrow K\bar{K}$	101
8.4.2	Absence of 3P_2	101
8.5	Comparison to earlier Crystal Barrel Fit	102
9	Conclusion	103
10	Appendix Kinematic Fitting	104
10.0.1	Introduction	104
10.0.2	KinFitHypothesis	104
10.0.3	KinFitPermutation, description of fitting algorithm	104
10.0.4	Final Errors and pulls	106
10.0.5	Conversion of Rectangular to Helix Parameters	107
10.0.6	PED parameters to Rectangular	107
11	Appendix Steering Cards	109
12	Appendix Data	111

Chapter 1

Introduction

The study of $p\bar{p}$ annihilations is a useful method for the spectroscopy of low mass mesons in the 1-2 GeV/ c^2 mass spectrum. Annihilations into three scalar particles are especially useful, because of the simplicity of describing the complete kinematics with only two variables, which can be nicely plotted in a Dalitz plot. Three body channels involving pions and etas have been well studied and have resulted in many new discoveries of mesons. The true nature of these mesons, however, is still not well understood.

Some of the various $q\bar{q}$ meson nonets are fairly well established, including the pseudoscalars (i.e. π , η , η' , K), vectors (i.e. ρ , ω , ϕ and K^*) and tensors (i.e. $a_2(1320)$, $f_2(1270)$, $f'_2(1525)$, $K_2^*(1430)$). The scalar nonet is not well established. In fact, none of the members are assigned without controversy (except perhaps the $K_0^*(1430)$). But the scalar sector is where the lowest mass glueball is predicted. A glueball is a bound state of two or three gluons; the only hard predictions are from the lattice QCD community[20] and [43] who predict the scalar glueball to be in the 1.4-1.8 GeV range.

Two of the new mesons discovered in pionic and eta-mesonic physics are the $f_0(1500)$ and the $a_0(1450)$. The $f_0(1500)$ is believed to be either the glueball alone or a mixed state of glueball and $q\bar{q}$ meson, while the $a_0(1450)$ is rumored to be the $I = 1$ member of the 0^{++} meson nonet[44, 9, 41]. The best evidence for the glueball nature of the $f_0(1500)$ is its decays into channels of different flavor, i.e. up, down and strangeness. Its decays into non-strange channels is well known, but its decays into strange channels is less so. It is crucial to know the coupling into strangeness, because this will aid in determining whether it is a flavor-blind glueball or if it is the $s\bar{s}$ member of the $q\bar{q}$ nonet.

The first measurement of the branching ratio of $f_0(1500) \rightarrow K\bar{K}$ was done in an analysis of $p\bar{p} \rightarrow K_L K_L \pi^0$ [2]. In this case, the $f_0(1500)$ was seen decaying into $K_L K_L$. However, the $a_0(1450)$ (if it exists) can also decay this way, and it was seen that it was difficult to separate the contributions of these two scalar mesons. What was needed was a channel where only one of these scalar mesons was allowed, in order to definitively measure their strangeness couplings without interference. Even without a constraint on the $a_0(1450)$ the $s\bar{s}$ coupling of the $f_0(1500)$ was “small”, making it low in $s\bar{s}$ content. This means that another meson must be the $s\bar{s}$ meson, e.g. the $f_J(1700)$ or some other undiscovered f_0 meson. A better constraint on the $\text{BR}(f_0(1500) \rightarrow K\bar{K})$ value requires a precise measurement of $\text{BR}(a_0(1450) \rightarrow K\bar{K})$ from another channel.

One such channel is $p\bar{p} \rightarrow K^0 K^\pm \pi^\mp$ where the neutral kaon is either K_S or K_L . The reaction with K_L has been studied in a previous work; however, because the K_L is virtually undetected by our experiment, the resolution of this study was not ideal. The alternative, with K_S decaying in its charged mode, $K_S \rightarrow \pi^+ \pi^-$, has higher resolution because the event is fully reconstructed, and also allows a trigger to enrich the data sample. The only drawback is that in order to get high statistics, a K_S trigger requires a secondary vertex outside of the vertex detector. This requirement makes a large effect on the momentum-dependent efficiency, cutting on low momentum kaons that decay inside the vertex detector, thus vetoing the trigger. With proper Monte Carlo simulations, this trigger effect can be corrected.

There were three aims of this analysis.

1. The first goal was to determine which resonances make up the $p\bar{p} \rightarrow K_S K^\pm \pi^\mp$ annihilation channel. Besides the well known mesons ($K^*(892)$ and $a_2(1320)$ which are visually apparent), there is some confusion over the contributions from $a_0(1450)$, $a_2(1650)$, $\rho(1450)$, and $\rho(1700)$. The $K\bar{K}$ threshold enhancement (typically called the $a_0(980)$ resonance) needs to be better understood.
2. The second goal was to describe the properties of the $a_0(1450)$ (if it exists) including its mass, width

and branching ratios from $p\bar{p}$ annihilation. Knowledge of the $a_0(1450)$ will help in determining the $K\bar{K}$ decay mode of the $f_0(1500)$.

3. The third goal was to determine the properties of the $a_0(980)\rightarrow K\bar{K}$ decay with high statistics.

In the process of doing this experiment, several new results were found. First, the contribution from $K_2^*(1430)$ was surprisingly important in the fits. The statistical significance of this channel is much greater than the evidence for the “expected” resonances, such as the $a_0(980)$ or $a_0(1450)$. Second, the unique shape of the $K_2^*(1430)$ mimics the *exact* shape of the $K\bar{K}$ threshold enhancement, and can entirely replace the $a_0(980)$ intensity. This means that the $a_0(980)\rightarrow K\bar{K}$ branching ratio can be much smaller than previously measured, consistent with zero. The true nature of the $a_0(980)$ has been a mystery since its discovery (see Cahn’s “Mystery of the [$a_0(980)$]”[27] for a discussion about how the $a_0(980)$ ’s branching ratios seem to be dependent on the production), and this discovery may aid in developing a consistent picture of this “particle”. Finally, the statistical evidence for the $a_0(1450)$ is not as high as previously thought, and the signal may be instead the $\rho(1450)$.

Chapter 2

Physics background

2.1 $p\bar{p}$ Annihilation at rest

Theoretical understanding of $p\bar{p}$ annihilation is lagging far behind experimental observations, mostly because quantum chromo-dynamics (QCD) is not directly calculable at this energy scale because the color coupling-constant becomes too large for perturbation calculations. The limited theoretical guidance comes from conservation of quantum numbers, including angular momentum, parity, charge parity, isospin and G-parity. Some success has been had by treating the quarks as confined in bags [32] or a harmonic oscillator potential[30, 38, 39].

In $p\bar{p}$ annihilation at rest, the three antiquarks of the \bar{p} , the three quarks of the p and all the gluons and other sea-quarks interact with each other. This quark gas of energy 2 GeV evaporates into an average of five pions, and may be thought of as a statistical thermodynamic process. There are similarities between this low energy process and that of the quark-gluon plasma sought in high energy experiments (such as RHIC) [15]. Within this color-rich environment, bound states of gluons, called “glueballs”, and other exotic mesons are expected to be formed. An exotic meson is one that is not formed by a simple $q\bar{q}$ pair, but by $q\bar{q}g$ or $qq\bar{q}\bar{q}$.

2.2 Capture and Cascade in Hydrogen

In liquid or gaseous hydrogen, very slow antiprotons (200 MeV/c) eventually come to a stop and are captured by protons in a hydrogen-like atom called protonium. For a complete description of $p\bar{p}$ annihilation at rest, see [22]. The capture states usually have a quantum number of $n \sim 30$ and high angular momentum of $L \sim 30$. Eventually this excited state decays to a low angular momentum state through the emission of x-rays. Typically, annihilation does not occur until $L < 2$, because the orbital wave-functions do not overlap sufficiently.

In rare gaseous hydrogen, the $1P$ ($L = 1$) state is arrived at first in the cascade, and thus annihilation occurs primarily from the P wave. This contrasts the situation in the liquid where S ($L = 0$) wave annihilation dominates. Due to the higher density of liquids, the increased collisions with neighboring H_2 atoms cause significant Stark mixing of levels. The Stark effect causes transitions to the S state to occur faster than annihilation in P states. In fact, annihilation in liquid is nearly 90% due to S-wave. The exact ratio of P to S wave annihilation is still not understood because the ratio depends on the final state observed. Historically, P wave annihilation in LH_2 annihilation at rest has been ignored to simplify the partial wave analysis calculations, and this has been successful to a large extent based on the quality of the final fits. However, in this analysis with its high statistics, including P wave annihilation in the fits improves the χ^2 significantly.

Because the cascade process involves interaction with the surrounding medium, the quantum coherence between different states is lost. Essentially the constant bumping of neighboring hydrogen atoms and the emission of real X-rays has “measured” the state of the protonium, and thus collapsed the wave-function before annihilation takes place. Thus channels that proceed from different initial states do not coherently interfere with each other. The initial state is defined by the J^{PC} of the $p\bar{p}$ state, listed in section 2.6.

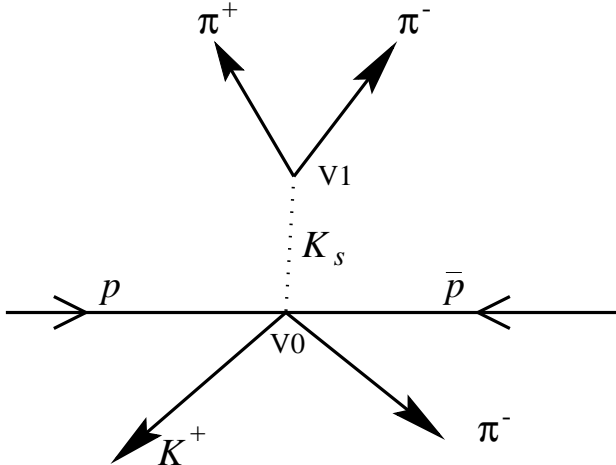


Figure 2.1: The topology for the reaction, starting with $p\bar{p}$ annihilation at vertex V0 into K_S , K^\pm and π^\mp , with subsequent $K_S \rightarrow \pi^+\pi^-$ at vertex V1.

2.3 Isobar model

In the two-body isobar model[37, 17], $p\bar{p}$ annihilation proceeds primarily through two-meson intermediate states. In a three-body final state, $p\bar{p}$ proceeds through a short-lived resonance, called the *isobar*, and a spectator meson. The isobar then further decays to two mesons.

The dynamics and angular momentum of the isobar dictates the final form of the Dalitz plot. For a particular isobar in a Dalitz plot, one axis of the intensity is described by the dynamical form, usually a Breit-Wigner or K -matrix. The perpendicular axis is described by the spin-parity function, a function of the various angular momenta of the particles, the total angular momentum and Clebsch-Gordan coefficients. Spinless particles have a flat distribution in this perpendicular axis, while vector and tensor particles have variations similar to the shapes of the letter “U” or “W.”

This analysis is concerned with analyzing the $KK\pi$ system. In this three body reaction, there are two possible classes of isobars, the non-strange KK isobar and the strange $K\pi$ isobar. The particular choice of $KK\pi$ system determines which isobars are present and which initial states are allowed.

In particular, the reaction

$$p\bar{p} \rightarrow K^0 K^\pm \pi^\mp$$

is the physical reaction of interest. This channel is unique in that the $K\bar{K}$ system must have isospin $I = 1, I_3 = \pm 1$ because it is recoiling against the π^\mp which has isospin $I = 1, I_3 = \mp 1$. This rules out contributions from $I = 0$ states such as ϕ , $f_0(980)$, $f_0(1300)$, $f_0(1500)$, and $f_2(1525)$, leaving only $I = 1$ states such as $\rho(1700)$, $a_0(980)$, $a_2(1320)$ and $a_0(1450)$. Also, the strange $K\pi$ states include both charged and neutral combinations of K and π . This makes for interesting interference patterns where the two combinations cross in the Dalitz plot.

2.4 The reaction $K_S K^\pm \pi^\pm$

The K^0 meson is the strong eigenstate, but it is not observed. It is a linear combination of two other states, the K_1 and K_2 , which are CP eigenstates and are nearly the observed states. The observed states are actually $K_S \sim K_1$ and $K_L \sim K_2$; the small CP violating differences are not important in this analysis. Because the K^0 is then half K_S and half K_L , the branching ratios that are quoted for states with K^0 are usually double that quoted for states with K_S or K_L .

The specific reaction that is analyzed in detail in this report is

$$p\bar{p} \rightarrow K^\pm \pi^\mp K_S \rightarrow \pi^+ \pi^- .$$

Particle	I^G	J^{PC}
π^\pm	1^-	0^-
a_0	1	0^+
ρ^0	1	1^-
K^\pm	$\frac{1}{2}$	0^-
K_S	$\frac{1}{2}$	0^{-+}
$K^*(890)$	$\frac{1}{2}$	1^{--}
$K_0^*(1430)$	$\frac{1}{2}$	0^+
$K_2^*(1430)$	$\frac{1}{2}$	2^+

Table 2.1: The quantum numbers for some mesons. G is not defined for strange mesons and C is not defined for charged particles.

where annihilation occurs at the primary vertex V0 and the K_S decay occurs at the secondary vertex V1 (see figure 2.1). The displacement of the secondary vertex ($c\tau = 2.68$ cm) allows a fast experimental trigger (see section 4.1) as well as a clean event tag on the K_S .

The resultant four charged particles can be directly measured via their ionization tracks in the Jet Drift Chamber (JDC). Because the trigger also required long tracks, low energy tracks have lower efficiency because they can curl up. Also, the charged kaon can decay ($K^+ \rightarrow \mu^+ \nu$) within the JDC fiducial volume at low energy. Neglecting these minor losses, the complete event is reconstructed.

2.5 Particles, Quantum Numbers and Selection Rules

In this section, we discuss the properties of the particles involved and the appropriate selection rules for $p\bar{p}$ annihilation.

2.5.1 Final-state particles

In this reaction, there 5 distinct final-state mesons,

$$\pi^+, \pi^-, K^+, K^- \text{ and } K_S.$$

These are all pseudoscalar mesons, meaning

$$J^P = 0^-.$$

2.5.2 Intermediate state isobar particles

The isobar decays into pairs of final-state particles. To determine allowed isobars, we shall combine the final pseudoscalar mesons together pairwise with a relative angular momentum $l = 0, 1, 2$. Using $P_l = -1^l$ and the fact that the pseudoscalars have no spin, we see that the intermediates can only be

$$J^P = 0^+, 1^-, 2^+ \dots$$

Next, considering isospin I , the pair πK can have isospin $1/2$ or $3/2$. However, if we limit our analysis to intermediates that can be described by the quark model, $I = 3/2$ is eliminated because it can not be constructed with only two quarks (3-quark baryons are eliminated by insufficient energy from $p\bar{p}$ annihilation). In addition, the spin-parity structure is the same for $I = 1/2$ and $I = 3/2$. Thus we limited ourselves to $I = 1/2$ for πK resonances. The allowed quantum numbers for πK resonances are

$$IJ^P = \frac{1}{2}0^+, \frac{1}{2}1^-, \frac{1}{2}2^+.$$

These correspond to the known resonances $K_0^*(1430)$, $K^*(890)$, and $K_2^*(1430)$.

For the pair KK , we can get $I = 0$ or $I = 1$. In the next section, we will show that $I = 0$ is not allowed in this particular annihilation channel. $G = -1^{L+S+I} = -1^{L+1}$ for $S = 0$ and $I = 1$. So the allowed quantum numbers for KK resonances are

$$I^G J^P = 1^- 0^+, 1^+ 1^-, 1^- 2^+,$$

corresponding to the known states $a_0(980, 1450)$, $\rho(1400, 1700)$ and $a_2(1320)$. Of course, there can be additional energy poles with the same quantum numbers.

2.6 $p\bar{p}$ Initial states

The allowed quantum numbers for $p\bar{p}$ annihilation states can be easily enumerated by combining all possible values of $L' = 0, 1$ (the prime is to distinguish this L' from the L used later on) with all possible values of spin. We know that $p\bar{p}$ annihilation at rest proceeds dominantly from $L' = 0$ and somewhat from $L' = 1$. Since the spin of the proton is $\frac{1}{2}$, the total spin of $p\bar{p}$ is either 0 or 1. Then J can take on 0, 1 or 2. The parity of a fermion-antifermion pair is calculated using

$$P = -1^{L+1}$$

while the charge-parity is calculated using

$$C = -1^{L+S}.$$

L'	S	$^{2S+1}L_J$	J^{PC}
0	0	1S_0	0^{-+}
0	1	3S_1	1^{--}
1	0	1P_1	1^{+-}
1	1	3P_0	0^{++}
1	1	3P_1	1^{++}
1	1	3P_2	2^{++}

The isospin can be either $|II_3\rangle = |10\rangle$ or $|II_3\rangle = |00\rangle$. Note that the I_3 component must be zero. Assuming annihilation through the two-body model, one of the bodies is a spectator meson and the other is a shorter-lived intermediate resonance. In this analysis, the spectator is one of the mesons π^\pm , K^\pm , or K_S , or in other words, a 0^{-+} pseudoscalar, with $I^G = 1^-$ or $I = 1/2$. If the spectator is the π^\pm with $|II_3\rangle = |1\pm 1\rangle$, the intermediate must have $I_3 = \mp 1$, requiring $I = 1$. This explains why $I = 0$ KK intermediates are not allowed, as mentioned in the preceding section.

To see which states are accessible from $p\bar{p}$, we make all combinations of spectator pseudoscalar and intermediate, in relative spin-states of L . This L is between the isobar and spectator, not to be confused with the L' in the previous table which was between the proton and antiproton.

PS + Inter.	$L = 0$	$L = 1$	$L = 2$
$(0^- + 0^+)_L$	0^-	1^+	2^-
$(0^- + 1^-)_L$	1^+	$0^-, 1^-, 2^-$	$1^+, 2^+, 3^+$
$(0^- + 2^+)_L$	2^-	$1^+, 2^+, 3^+$	$0^-, 1^-, 2^-, 3^-, 4^-$

2.7 Isospin and C -Parity Considerations

Because the initial states are well defined J^{PC} states, the intermediates need to be written in eigenstates of P and C . This process coincidentally puts the intermediates in eigenstates of I , even though the initial $p\bar{p}$ state is not an eigenstate of I . In the notation of $|I I_3\rangle$,

$$|p\bar{p}\rangle = |\frac{1}{2} \frac{1}{2}\rangle \oplus -|\frac{1}{2} -\frac{1}{2}\rangle = -\sqrt{\frac{1}{2}}(|1 0\rangle + |0 0\rangle).$$

The isospin doublets and triplets used in the following discussion are defined as follows. The assignment is true for excited states (e.g. K^*) as well.

$$\begin{pmatrix} \frac{1}{2} \\ -\frac{1}{2} \end{pmatrix} \rightarrow \begin{pmatrix} p \\ n \end{pmatrix}, \begin{pmatrix} \bar{n} \\ -\bar{p} \end{pmatrix}, \begin{pmatrix} K^+ \\ K^0 \end{pmatrix}, \begin{pmatrix} \bar{K}^0 \\ -K^- \end{pmatrix}$$

$$\begin{pmatrix} 1 \\ 0 \\ -1 \end{pmatrix} \rightarrow \begin{pmatrix} \pi^+ \\ \pi^0 \\ \pi^- \end{pmatrix}, \begin{pmatrix} a^+ \\ a^0 \\ a^- \end{pmatrix}, \begin{pmatrix} \rho^+ \\ \rho^0 \\ \rho^- \end{pmatrix}$$

Isospin $I I_3$	P	C	BR Factor	Wave-function
$ 0\ 0\rangle$	-1^{L+1}	+	3/2	$\sqrt{\frac{1}{3}}(a^+\pi^- \rangle + a^-\pi^+ \rangle - a^0\pi^0 \rangle)$
$ 1\ 0\rangle$	-1^{L+1}	-	1	$\sqrt{\frac{1}{2}}(a^+\pi^- \rangle - a^-\pi^+ \rangle)$
$ 2\ 0\rangle$	-1^{L+1}	+	3	$\sqrt{\frac{1}{6}}(a^+\pi^- \rangle + a^-\pi^+ \rangle + 2 a^0\pi^0 \rangle)$
$ 0\ 0\rangle$	-1^L	-	3/2	$\sqrt{\frac{1}{3}}(\rho^+\pi^- \rangle + \rho^-\pi^+ \rangle - \rho^0\pi^0 \rangle)$
$ 1\ 0\rangle$	-1^L	+	1	$\sqrt{\frac{1}{2}}(\rho^+\pi^- \rangle - \rho^-\pi^+ \rangle)$
$ 2\ 0\rangle$	-1^L	-	3	$\sqrt{\frac{1}{6}}(\rho^+\pi^- \rangle + \rho^-\pi^+ \rangle + 2 \rho^0\pi^0 \rangle)$
$ I\ 0\rangle$	-1^{L+1}	C	3/2	$-\frac{1}{2} \left[K^{*+}K^- \rangle + (-1)^I K^{*0}\overline{K^0} \rangle \right. \\ \left. + C \left(K^{*-}K^+ \rangle + (-1)^I \overline{K^{*0}}K^0 \rangle \right) \right]$

Table 2.2: The isospin and C -parity eigenstates. The BR Factor is described in section 2.7

The C -parity operation gives the following:

$$C|a^+\pi^- \rangle = +|a^-\pi^+ \rangle$$

$$C|\rho^+\pi^- \rangle = -|\rho^-\pi^+ \rangle$$

$$C|K^{*0}\overline{K^0} \rangle = -|K^{*0}\overline{K^0} \rangle$$

$$C|K^{*+}K^- \rangle = -|K^{*-}K^+ \rangle.$$

The intermediate states $p\bar{p} \rightarrow a\pi$ and $p\bar{p} \rightarrow \rho\pi$ are mixtures of $I = 0, 1, 2$. The initial states $p\bar{p} \rightarrow K^*K$ are mixtures of $I = 0, 1$. However, the simplest isospin eigenstates of the later are not C -parity eigenstates, so linear combinations must be taken to arrive at C -parity eigenstates. The simple decompositions are

$$|1\ 0\rangle_a = \sqrt{\frac{1}{2}}(-|K^{*+}K^- \rangle + |K^{*0}\overline{K^0} \rangle) \quad (2.1)$$

$$|1\ 0\rangle_b = \sqrt{\frac{1}{2}}(-|K^{*-}K^+ \rangle + |\overline{K^{*0}}K^0 \rangle) \quad (2.2)$$

$$|0\ 0\rangle_a = \sqrt{\frac{1}{2}}(-|K^{*+}K^- \rangle - |K^{*0}\overline{K^0} \rangle) \quad (2.3)$$

$$|0\ 0\rangle_b = \sqrt{\frac{1}{2}}(-|K^{*-}K^+ \rangle - |\overline{K^{*0}}K^0 \rangle) \quad (2.4)$$

The C -parity linear combination of $|I\ 0\rangle_{a,b}$ is given in table 2.2, as well as the decompositions for $|a\pi\rangle$ and $|\rho\pi\rangle$. The quantity L is the relative orbital angular momentum between the isobar and its spectator.

What these wave-functions in table 2.2 tell us are the branching ratio scaling factors to be applied to the measured branching ratios to account for the entire wave-function, observed and unobserved. For instance, in the $I = 0$ decomposition of the $|a\pi\rangle$ state, we see that each of the charge variations ($|a^+\pi^- \rangle$, $|a^0\pi^0 \rangle$, $|a^-\pi^+ \rangle$) have equal coefficients. Since we only observe $|a^+\pi^- \rangle$ and $|a^-\pi^+ \rangle$, the final answer needs a factor of 3/2 to account for the unobserved $|a^0\pi^0 \rangle$. For the $I = 1$ decomposition, there is no $|a^0\pi^0 \rangle$, so there is no correction factor necessary. For the $|K^*K\rangle$, all charge variations are measured, so there is no correction for unobserved channels, but there is a 3/2 correction because of the way the K^* decomposes, which comes from (2.5). These scaling factors are given in the ‘‘BR Factor’’ column of table 2.2. In addition to these scaling factors, only half of the K^0 decays are seen as K_S , so there is another global factor of 2 applied to all channels. This net scaling factor is given in table 2.3.

2.8 Kaon decays

The strong decays of excited kaons are as follows. If they decay into a kaon and a pion, then we need to consider $1 \times 1/2$ Clebsch-Gordan coefficients. By conserving strangeness and observing the isospin sign

$I^G J^{PC}$	$^{2S+1}L'_J$	$\pi^\pm a_0$	$\pi^\pm \rho^\mp$	$\pi^\pm a_2$	$K^\pm K^{*0}$	$K^\pm K^*$	$K^\pm K^{*2}$
0^+0^{-+}	1S_0	0 (3)		2 (3)	0 (3)	1 (3)	2 (3)
1^-0^{-+}	1S_0		1 (2)		0 (3)	1 (3)	2 (3)
0^+1^{--}	3S_1		1 (3)			1 (3)	2 (3)
1^-1^{--}	3S_1			2 (2)		1 (3)	2 (3)
0^+1^{+-}	1P_1		0,2 (3)		1 (3)	0,2 (3)	1 (3)
1^-1^{+-}	1P_1	1 (2)		1 (2)	1 (3)	0,2 (3)	1 (3)
0^+0^{++}	3P_0						
1^-0^{++}	3P_0						
0^+1^{++}	3P_1	1 (3)		1 (3)	1 (3)	0,2 (3)	1 (3)
1^-1^{++}	3P_1		0,2 (2)		1 (3)	0,2 (3)	1 (3)
0^+2^{++}	3P_2			1 (3)		2 (3)	1 (3)
1^-2^{++}	3P_2		2 (2)			2 (3)	1 (3)

Table 2.3: Initial $p\bar{p}$ states and allowed two-body final states. The values in the table are given as “ $L(f)$ ”, where L is the allowed spin state(s) between isobar and spectator and f is the branching ratio scaling factor (see section 2.7).

convention for K^- , we get

$$K^{*+} \rightarrow \sqrt{2/3}|\pi^+K^0\rangle - \sqrt{1/3}|\pi^0K^+\rangle \quad (2.5)$$

$$K^{*-} \rightarrow \sqrt{2/3}|\pi^-K^0\rangle + \sqrt{1/3}|\pi^0K^-\rangle \quad (2.6)$$

$$K^{*0} \rightarrow -\sqrt{2/3}|\pi^-K^+\rangle + \sqrt{1/3}|\pi^0K^0\rangle \quad (2.7)$$

$$\overline{K}^{*0} \rightarrow -\sqrt{2/3}|\pi^+K^-\rangle - \sqrt{1/3}|\pi^0\overline{K}^0\rangle. \quad (2.8)$$

The strong eigenstates of the neutral kaons, K^0 and \overline{K}^0 are not CP eigenstates. When they do decay, they decay into either two pions ($CP = +1$) or three pions ($CP = -1$). These two decays have very different rates because of the phase space involved. Thus it appears that the K^0 and \overline{K}^0 have been transformed into two new states, K_S and K_L , which are CP eigenstates. The K_S is the short lived particle, which is seen in this analysis. The decomposition is as follows:

$$K_S = \sqrt{1/2}(|K^0\rangle + |\overline{K}^0\rangle) \quad (CP = +1)$$

$$K_L = \sqrt{1/2}(|K^0\rangle - |\overline{K}^0\rangle) \quad (CP = -1)$$

or transforming to the other basis,

$$K^0 = \sqrt{1/2}(|K_S\rangle + |K_L\rangle) \quad (2.9)$$

$$\overline{K}^0 = \sqrt{1/2}(|K_S\rangle - |K_L\rangle) \quad (2.10)$$

2.9 Connecting initial $p\bar{p}$ states with isobar states

The next step is connecting the $p\bar{p}$ initial states with the isobar-spectator intermediate states, by comparing allowed quantum numbers. This is done in table 2.3, using the tables in section 2.6 and table 2.2. Only J^{PC} values are needed for selection criteria. The C -parity is critical in determining the isospin.

One can see that there are many allowed initial and intermediate states, with 45 allowed combinations! In practice, not all combinations are used in the fits. This is true especially for P wave annihilation and $L = 2$ states when a $L = 0$ state is also allowed for the same final state. We also note that there are no allowed states from 3P_0 .

2.10 A discussion of the states used in the partial wave analysis

In the partial wave analysis, we need to know not only how many resonances to use in the fit, but also if there are symmetry restrictions to the number of amplitudes to use in the fit. If there are identical particles in the final state, the dynamical amplitude must be symmetric under interchange of the particles. However, in practice the measured particles are not the original interaction particles and have undergone decays and flavor mixing (i.e. the K_S). In some channels, there may be symmetries that are not obvious from the list of final-state particles. For instance, in the Dalitz plot analysis of $\pi^0 K_S K_L$, the dynamical amplitude is symmetric under interchange of K_S and K_L .

For this analysis, all final-state particles are different (π^\pm , K^\pm , and K_S), but there may be some hidden symmetry. There is also some freedom to choose which basis to use in describing the isobars. In the past [31], the $\pi K K$ system was written in terms of eigenstates of isospin. This was fine in the distant past when isospin was believed to be a good symmetry, but in the present we know that isospin is broken by the differences in up and down quark masses. This difference is small, but easily measurable, for example in the mass difference of $K^*(892)^\pm$ and $K^*(892)^0$, which is $4.4 \pm 0.4 \text{ MeV}/c^2$, or about 0.5%. If one does the analysis in the isospin eigenstate basis (which is suited for isospin invariance), this mass difference needs to be inserted by hand in the formula depending on which axis the dynamical amplitude is being calculated. Since isospin invariance is not true, there is no reason to use the isospin eigenstate basis.

In the following steps, we derive the basis states used to describe the $\pi K K$ system. At first, we work in the isospin eigenstate basis, but then show at the end that we can write the basis in terms of charged and neutral K^* resonances equivalently. Once written in this manner, the mass difference is easier to include in the fitting algorithm. More importantly, the result of the fit gives the amplitudes in terms of charged and neutral K^* contributions, allowing a direct check of charge invariance in the strong reaction of $p\bar{p}$ annihilation which is believed to be charge-blind.

If we expand the intermediate states in table 2.2 with (2.5), (2.6), (2.7) and (2.8) we get the four states $\phi_{I,C}$ where $I = 0, 1$ and $C = +1, -1$. The order of particles listed in the kets is important; the pion and the first kaon decay from the K^* isobar, while the second kaon is a spectator.

$$\phi_{I,C} = \sqrt{\frac{1}{12}} \left\{ \begin{array}{cc} -|\pi^0 K^+ K^- \rangle & +\sqrt{2}|\pi^+ K^0 K^- \rangle \\ -(-1)^I \sqrt{2}|\pi^- K^+ \overline{K^0} \rangle & +(-1)^I |\pi^0 K^0 \overline{K^0} \rangle \\ +C[-|\pi^0 K^- K^+ \rangle & -\sqrt{2}|\pi^- \overline{K^0} K^+ \rangle \\ +(-1)^I \sqrt{2}|\pi^+ K^- K^0 \rangle & +(-1)^I |\pi^0 \overline{K^0} K^0 \rangle \end{array} \right\} \quad (2.11)$$

We can replace the K^0 and $\overline{K^0}$ particles with K_S and K_L . Since we do not observe the K_L nor the π^0 , we can simplify the isospin- C -parity $|I, C\rangle$ state expressions by suppressing all terms that are not observed in this analysis:

$$\phi_{I,C} \sim \left\{ \begin{array}{c} +|\pi^+ K_s K^- \rangle \\ -(-1)^I |\pi^- K^+ K_s \rangle \\ +C(-|\pi^- K_s K^+ \rangle \\ +(-1)^I |\pi^+ K^- K_s \rangle \end{array} \right\} \quad (2.12)$$

We note that each term has the same amplitude up to a sign. For $C = +1$, there are two states $I = 0, 1$ or

$$\begin{aligned} \phi_{0,+} &= |\pi^+ K_s K^- \rangle - |\pi^- K^+ K_s \rangle - |\pi^- K_s K^+ \rangle + |\pi^+ K^- K_s \rangle \\ \phi_{1,+} &= |\pi^+ K_s K^- \rangle + |\pi^- K^+ K_s \rangle - |\pi^- K_s K^+ \rangle - |\pi^+ K^- K_s \rangle \end{aligned}$$

Because each of these states will have an independent production amplitude in the partial wave analysis, we can take linear combinations of these two states and get the same result. Let us take

$$\psi_+ = \phi_{0,+} + \phi_{1,+} = |\pi^+ K_s K^- \rangle - |\pi^- K_s K^+ \rangle \quad (2.13)$$

$$\psi_- = \phi_{0,+} - \phi_{1,+} = |\pi^- K^+ K_s \rangle - |\pi^+ K^- K_s \rangle \quad (2.14)$$

We can see in this basis that the ψ_+ state describes $K^{*\pm} \rightarrow \pi^\pm K_s$, and that ψ_- state describes $K^{*0} \rightarrow \pi^\pm K^\mp$. This shows that the amplitude can be separated into two parts which represent the two axes of the Dalitz plot, i.e. the x axis which is $m^2(\pi^\pm K_S)$ and the y axis which is $m^2(\pi^\pm K^\mp)$. This approach is better than previous analyses which fit using the isospin eigenstates, because

1. The data Dalitz plot is obviously not symmetrical
2. The masses of $K^*(892)$ depend on the axis chosen, so isospin is broken anyways.
3. The amplitudes of the charged and uncharged K^* can be fixed to the same magnitude, but keeping individual phases. This can test the hypothesis that the intensities of the charged and uncharged K^* might be the same.
4. The ratio of charged versus neutral components of the $K\pi$ wave can be directly compared.

2.11 Resonances expected in $K_S K^\pm \pi^\pm$

The first experimental results for $K_S K^\pm \pi^\pm$ were published by the Saclay 81 cm bubble chamber collaboration at the CERN PS in May 1965 [16]. From only 1145 events, they noted strong K^* bands at 890 MeV in the $K\pi$ systems, as well as two other enhancements, the $K\bar{K}$ enhancement at threshold and another $K\bar{K}$ enhancement at 1250 MeV. The two $K\bar{K}$ enhancements are known as the $a_0(980)$ and $a_2(1320)$ respectively. We scanned the original data and binned it into a 30x30 histogram, which is shown in figure 7.14.

A later analysis with more statistics from the same bubble chamber (2000 events) attempted a partial wave analysis[31]. In this analysis, they introduced another broad resonance, the so called $K\pi$ S-wave, which they parameterized with a scattering length amplitude. With these four resonances, they were able to adequately fit the data.

There is an interesting asymmetry in the Dalitz plot. If one divides the plot into four sectors defined by the strong $K^*(890)$ bands, the lower-right sector has many more events than the upper-left sector. In addition, the left-end of the horizontal $K^*(890)$ band has much more intensity than the lower-end of the vertical $K^*(890)$ band.

Until the Crystal Barrel, this was the limit of knowledge of the $K_S K^\pm \pi^\pm$ system. The Crystal Barrel published a paper on $K_L K^\pm \pi^\mp$ with much higher statistics (13K)[4]. The fundamental physics behind this reaction, which substitutes a K_L for the K_S , should be the same as for $K_S K^\pm \pi^\pm$. In addition to the bubble-chamber resonances, two extra resonances were need to describe the data, the $a_0(1450)$ (recently discovered by the Crystal Barrel in decays to $\pi^0\eta$) and the $\rho(1450, 1700)$. The $\rho(1450, 1700)$ was characterized by two poles, although in the past it was characterized by one pole, called the $\rho(1600)$. The $K\pi$ S-wave was also improved by using the characterization from the LASS experiment[18].

Two other resonances which may play a part in this reaction are the $K_2^*(1430)$ and $a_2(1660)$. The $K_2^*(1430)$ is a well known resonance in the $K\pi$ system as measured by LASS [18], but because its mass is slightly above the limit of phase space and its spin is high, was not considered previously. The $a_2(1660)$ was used in an analysis of $\pi^0\pi^0\eta$ [11], but its significance was not emphasized. The $K_L K^\pm \pi^\mp$ analysis of [4] did not require this resonance.

We discuss the history of all of these resonances in detail below.

2.11.1 $K^*(892)$ resonance

This resonance appears as the dominant vertical and horizontal bands near 0.8 GeV² in the dalitz plot. It is the most visually obvious resonance in the reaction.

This resonance is modelled as a relativistic Breit-Wigner,

$$\frac{m_0\Gamma_0/\rho(m_0)}{m_0^2 - m^2 + im_0\Gamma_0}$$

The mass and width of the neutral K^* is $m_0 = 896.10$ MeV and $\Gamma_0 = 50.5$ MeV, while the mass of the charged K^* is $m_0 = 891.59$ MeV and $\Gamma_0 = 49.8$ MeV. The K^* is a vector meson, so its angular distribution appears as $\cos^2\theta$ in the 1S_0 state, and $\sin^2\theta$ in the 3S_1 state. Because the intensities of the two initial states are approximately equal, the bands appear flat because the complementary angular distributions cancel to some degree.

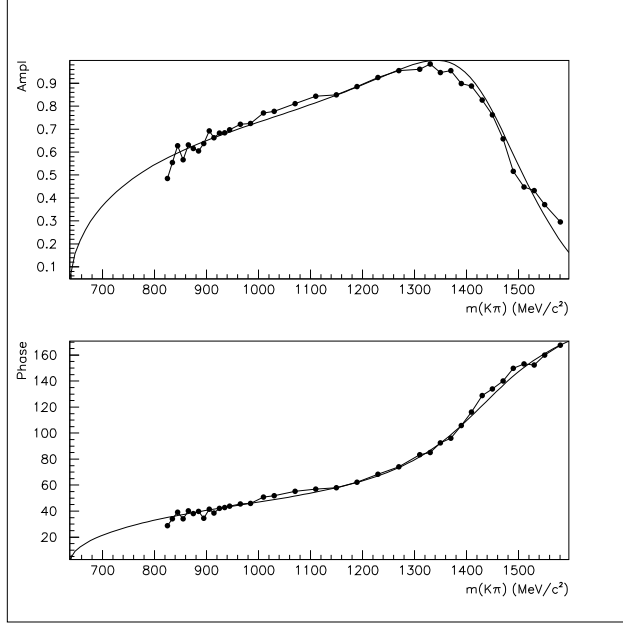


Figure 2.2: The LASS data for $K - \pi$ S-Wave scattering, and the fitted function given by (2.17), (2.16) and (2.15). Shown are magnitude and phase of T .

2.11.2 $K - \pi$ S wave

The $K\pi$ S-wave is not well understood on theoretical grounds, but is required empirically in all partial wave analyses to date.

The bubble chamber analyses [31] parameterized the S-wave using a scattering length parameterization which rises slowly with increasing mass.

$$\frac{1}{1 - ia_I p_{K\pi}}$$

$$a_{1/2} = +0.3 fm, \quad a_{3/2} = -0.3 fm$$

Later, the LASS collaboration[18] directly extracted the S-wave component from $K - \pi$ scattering, and parameterized it as a sum of an inelastic Breit-Wigner amplitude and a background term parameterized as an effective range. The same data was refit using the K -matrix formalism, with a pole term due to the $K_0^*(1430)$ resonance, and with a background term which describes the additional $K - \pi$ S-Wave component.

$$\hat{K} = \frac{m_0 \Gamma_0 / \rho(m_0)}{m_0^2 - m^2} + \frac{am}{2 + abq^2} \quad (2.15)$$

$m_0 = 1343.0$, $\Gamma_0 = 400.0$, $a = 0.00181$, $b = 0.00258$ (With MeV as units for mass). In the K -matrix formalism, the Lorentz-invariant transition amplitude is given by

$$\hat{T} = (1 - i\hat{K}\rho)^{-1}\hat{K} \quad (2.16)$$

where ρ is the two-body phase space. In the Dalitz plot, the Lorentz-invariant transition amplitude \hat{T} is used rather than the non-relativistic T . The original LASS data and the fitted T function are shown in figure 2.2; in this case, the non-relativistic form T is shown. T is calculated using

$$T = \hat{T}\rho \quad (2.17)$$

and equations (2.15) and (2.16).

In practice, the fit is insensitive to the exact parameterization of the $K\pi$ S-wave because it is so broad; for example, the χ^2 of the fit did not change significantly if the background term was omitted or parameterized as a first-order polynomial with two real coefficients. None of the individual contributions changed much, at least a lot less than the systematic error of the fit, when the background term was removed entirely. For example, the contribution from the $K\pi$ S-wave in 1S_0 dropped by only 15%, when the systematic error for this wave is estimated to be somewhere between 25 and 500% (see table 8.1).

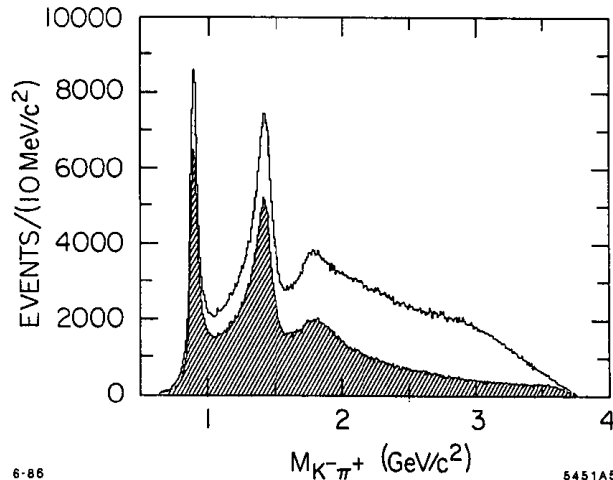


Figure 2.3: The $K^+\pi^-$ invariant mass distribution of events produced from $K\pi$ scattering. The shaded curve represents the effect of removing events from N^* production, which is not important to the discussion here. Figure is reproduced from the LASS experiment[18], Fig. 3.

2.11.3 $K_2^*(1430)$

The $K_2^*(1403)$ lies significantly outside of the phase space for this annihilation channel. However, because it is a strong resonance, the tails have a significant effect on the Dalitz plot. The LASS experiment has shown that this tensor $K_2^*(1430)$ has roughly twice the intensity of the vector $K^*(892)$ in the $K-\pi$ wave when there is no phase space limitation. See figure 2.3 which shows the large contribution from $K_2^*(1430)$ and the significant Breit-Wigner tail which extends down to at least $1 \text{ GeV}/c^2$. Of course, in the $K_S K^\pm \pi^\pm$ Dalitz plot, there is significant suppression due to phase space and the angular momentum barrier.

The shape of the distribution in the Dalitz plot is somewhat odd, because the central mass lies above the edge of the dalitz plot and because the angular momentum barrier function suppresses the intensity at the edge. The tails that appear in the Dalitz plot do not have the obvious horizontal or vertical ridge that is seen in the $K^*(892)$. Instead, the 1S_0 partial wave has diagonal bands caused by the characteristic “W” decay pattern of tensors. Figures 7.4, 7.5 and 7.6 show the unusual resonance patterns of the $K_2^*(1403)$ from different initial states.

2.11.4 $a_0(980)$

The $a_0(980)$ is an interesting resonance. It has two primary decay channels,

$$\begin{aligned} a_0(980) &\rightarrow \pi\eta \\ a_0(980) &\rightarrow K\bar{K}. \end{aligned}$$

However, in both channels, the resonance distribution in mass is severely distorted. The distortion in the $K\bar{K}$ channel is due to the fact that the mass of the $a_0(980)$ is at the $K\bar{K}$ threshold, so the decay can not happen at all below the threshold. Due to unitarity and analyticity of the dynamics, the shape of the $K\bar{K}$ amplitude directly influences the shape of the $\pi\eta$ amplitude, giving it a cusp-shape. This phenomenon is explained in the Flatté [35] parameterization of the $a_0(980)$, discussed below. The Flatté shapes are shown in figure 2.4. It is clear that neither the $\pi\eta$ nor $K\bar{K}$ amplitudes can be described by a Breit-Wigner.

The first bubble chamber analysis[31] parameterized the edge enhancement with a Breit-Wigner with a mass-dependent width

$$\frac{1}{s_{KK} - s_0 + ip_{KK}\gamma}$$

In the limit of a narrow resonance far from threshold, this width γ may be related to the more classical “constant width” Γ by the relation.

$$\Gamma = p_{KK}\gamma/\sqrt{s_0}$$

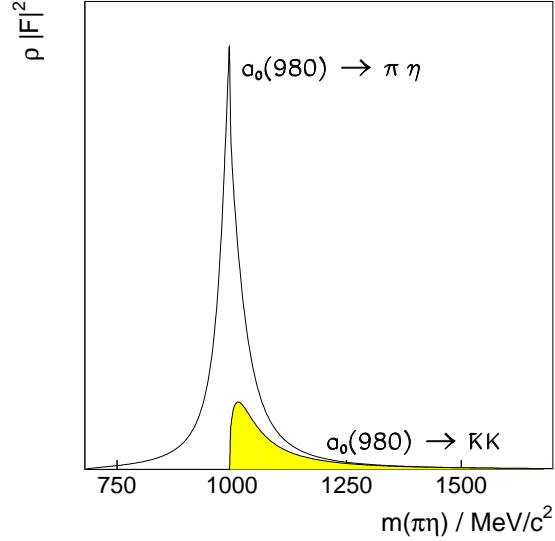


Figure 2.4: Amplitudes $\rho_{\pi\eta}|F_{\pi\eta}|^2$ and $\rho_{K\bar{K}}|F_{K\bar{K}}|^2$ (shared area).

This is an approximation to the Flatté distribution, whose width also increases with breakup momentum, p_{KK} .

The actual Flatté distribution is as follows

$$\hat{F}(s) = \frac{g_1}{m_0^2 - m^2 - i(\rho_1 g_1^2 + \rho_2 g_2^2)} \quad (2.18)$$

$$g_1^2 + g_2^2 = m_0 \Gamma \quad (2.19)$$

where $g_1 = g_{KK}$ and $g_2 = g_{\eta\pi}$. The details of the Flatté function and the connection to the K -matrix formalism is given in section 7.7.

The phase space terms are

$$\rho_1 = \pm \sqrt{\left(1 - \left(\frac{m_{\pi\pm} - m_\eta}{m}\right)^2\right) \left(1 - \left(\frac{m_{\pi\pm} + m_\eta}{m}\right)^2\right)}$$

$$\rho_2 = \pm \sqrt{\left(1 - \left(\frac{m_{K\pm} - m_{K^0}}{m}\right)^2\right) \left(1 - \left(\frac{m_{K\pm} + m_{K^0}}{m}\right)^2\right)}$$

The phase space signs are taken to be $+$ when calculating the physical resonance, but can take on either sign when calculating on the complex \sqrt{s} plane.

Because of this definition, the total width Γ is about 250 MeV, even though the peak width in the $\pi\eta$ channel is visibly much narrower, about 60 MeV. This has caused lots of confusion in getting a consistent number for the width, as the value is model dependent.

The physical resonance parameters are not the values used in any of the above formulations, but are extracted from the pole positions of the T-matrix of the form

$$E_{pole} = m_0 - i\Gamma/2.$$

Because the Flatté formula involves two phase space quantities (ρ_1 and ρ_2), each which have square-root branch cuts, there are four Riemann sheets in which the poles can be found. The two Breit-Wigner poles are always found on the second and third Riemann sheets (see [19] for a classification of the poles). In the partial wave analysis of this report, we shall cite the relevant pole position to obtain the correct values for the mass and widths

2.11.5 $a_0(1450)$

The assignment of the scalar $q\bar{q}$ nonet to experimentally seen resonances is controversial. Many candidates are available for the $I = 0$ f component, while the historical assignment of the $a_0(980)$ to the $I = 1$ component has been called into question because of evidence that the $a_0(980)$ could be a kaonic molecule or four quark state. Moreover, the mass appears to be lower than expected, assuming that the $K_0^*(1430)$ is the $I = 1/2$ component.

A search for a replacement candidate has yielded some observations in the 1300-1500 range. Boutemeur and Poulet[25] announced at Hadron 89 an isovector scalar meson with mass ~ 1320 and width 130. In 1994, the Crystal Barrel announced observation[11] of the $a_0(1450)$ with mass $m = (1450 \pm 40)$ MeV and $\Gamma = (270 \pm 40)$ MeV, seen in the $a_0(1450) \rightarrow \eta\pi^0$ decay mode in $p\bar{p} \rightarrow \pi^0\pi^0\eta$. The reduced χ^2 decreased from 2.1 to 1.3 with $N_{\text{dof}} = 1249$. The $a_0(1450)$ is 5% of the Dalitz plot.

A later coupled channel analysis[12] confirmed the $a_0(1450)$ with $\text{BR} = (0.29 \pm 0.11) \times 10^{-3}$, $m = 1470 \pm 25$ MeV and $\Gamma = 265 \pm 30$ MeV. A further analysis[1], used $a_0(1450)$ with a 3% contribution and $\text{BR} = (0.203 \pm 0.038)^{-3}$, which agrees with the previous coupled analysis. However, the focus of this paper was on the $I = 0$ resonances, not the $a_0(1450)$.

At Hadron 97, the Crystal Barrel announced observation of the $a_0(1450)$'s decay into $K\bar{K}$ [4], while the OBELIX collaboration announced observation of an $a_0(1300)$'s decay into $K\bar{K}$ [46]. The mass, width and branching ratio parameters of these 2 resonances were *not* compatible. The Crystal Barrel's $a_0(1450)$, with $m = (1480 \pm 30)$ MeV and $\Gamma = (265 \pm 15)$ MeV, had decay rates into KK that agree with the SU(3) prediction.

In other analyses, inclusion of the $a_0(1450)$ was not incompatible with the data, but not absolutely required. In the $\pi^0\pi^0\eta'$ Dalitz plot[3], the $a_0(1450)$ was needed. However, the contribution could be as small as 1.5 ± 1.2 % and the mass parameters were not well constrained according to the text. In Ehmman's paper, $p\bar{p} \rightarrow \pi^+\pi^-\eta$, and they claim that the $a_0(1450)$ is necessary, but don't give any numbers. In the exotic paper[5], the $a_0(1450)$ was not needed in the fit at all. In truth, the $a_0(1450)$ has only been seen in the $\eta\eta\pi^0$ and $K_L K^\pm \pi^\mp$ Dalitz plots.

Because the parameters of the a_0 are not well determined, we explored the complete parameter space of mass, width and branching ratio for this isovector, scalar resonance, modeling it as a Breit-Wigner resonance. If the mass is indeed above 1300 MeV, the K -matrix formalism is not necessary to describe the distortion from the $a_0(980)$.

2.11.6 $\rho(1450)$ and $\rho(1700)$

The $\rho(1450)$ and $\rho(1700)$ are two "new" resonances which used to be lumped together as the $\rho(1600)$. The $\rho(1700)$ has been seen in its decay into $K\bar{K}$ [29], while the $\rho(1450)$ has not[33]. The evidence against the $K\bar{K}$ decay mode of the $\rho(1450)$ is not terribly convincing, because it assumes that the $I = 0$ and $I = 1$ amplitudes are real and positive, which is mostly likely not the case. For example, if the amplitudes were real but relatively negative, there would be evidence for the $K\bar{K}$ decay mode.

The problem with a $\rho(1450)$ is that it has nearly the same mass as the $a_0(1450)$, making it hard to disentangle the two.

2.11.7 $a_2(1660)$

The $a_2(1660)$ was introduced for the first time in a Crystal Barrel analysis on $\pi^0\pi^0\eta$ [11]. As stated in the paper,

We find that the fit ... can be improved by adding a small contribution of a higher mass $\pi^0\eta$ D-wave resonance with a mass of 1600 MeV to 1700 MeV and a width of 180 MeV to 250 MeV. As the contribution of this additional resonance is marginal, (1.0 ± 0.5) %, and localized at the edges of the Dalitz plot where acceptance corrections are relatively more important, we refrain from attaching any physical meaning to this effect.

Recently, the $a_2(1660)$ has aroused more interested in the spectroscopy community, so we attempt to include it in our fits.

2.11.8 $K^*(1410)$

The strange vector $K^*(1410)$ could also be a part of the Dalitz plot, even though its coupling to $K\pi$ is somewhat small. We attempt to include it in our fits.

Chapter 3

Software tools

This chapter discusses the software used in the analysis, including the software written by the author.

3.1 cblbl++

A C++ class library was written by the Uni-Bochum group to wrap all of the FORTRAN code in a C++ interface. However, with the advent of the CLHEP standard C++ class library for High Energy Physics, much of the code needed to be rewritten to take advantage of the better list handling classes, better interface to HBOOK, as well as improving the data I/O classes. Further more, wrappers for charged data did not exist and needed to be written. This rewritten class is now known as `cblbl++`.

A detailed description of the software is omitted here, because most of it concerns technical details of data management, i.e. pointer juggling or simple 4-vector arithmetic. One of the interesting classes that is part of `cblbl++` is `KinFit`, the general purpose kinematic fitter. This is described below.

3.2 Vertex Fit

The section summarizes the operation of the vertex fit which was specially written for this analysis. The details are given in a technical report[42].

3.2.1 Introduction

There are two components in making a proper multi-vertex fit to an event. First is determining the track-to-vertex topology, and second is constraining the tracks to the measured JDC hits.

The Crystal Barrel was designed primarily for detection of neutral particles, a task that was nearly impossible in the 1960's bubble chamber experiments, especially if there was more than one neutral particle. In most cases, resonances or other intermediates decay via strong or electro-magnetic forces, meaning that the lifetimes are very short ($t \ll 10^{-15}$ s). The distance such a particle can move in such a short time is only a few nanometers or less, which is entirely undetectable in a drift chamber or vertex detector which have resolutions of 0.1 to 1 mm in the Crystal Barrel. It appears that all charged tracks and nearly all neutral photons originate from the same spot, the $p\bar{p}$ annihilation point.

Thus the old vertex fit algorithm simply assigned all tracks to one vertex. For computational simplicity, the fit did not constrain the tracks to lie on the "hit" positions. It simply took the results from the helix fit, which did constrain the tracks to the hit positions, and adjusted the helix parameters via an iterative algorithm so that they all passed through a common point in space. In practice, this was a reasonable thing to do for 2-track events with long tracks. However, for short tracks in 4-track events, the fit tended to severely rotate tracks around to force a single vertex. These rotated tracks no longer intersected the measured hits; in some cases the rotation was as large as 90 degrees, totally changing the true direction vector of the track. In addition, vertices separated by less than 1 cm would be incorrectly merged into a single vertex if the helix constraints were "soft".

In the unique case of $K_S \rightarrow \pi^+ \pi^-$, the K_S travels a few cm before decaying. This distance is easily measurable in the Crystal Barrel, and creates a distinct second vertex. A new vertex fit algorithm was

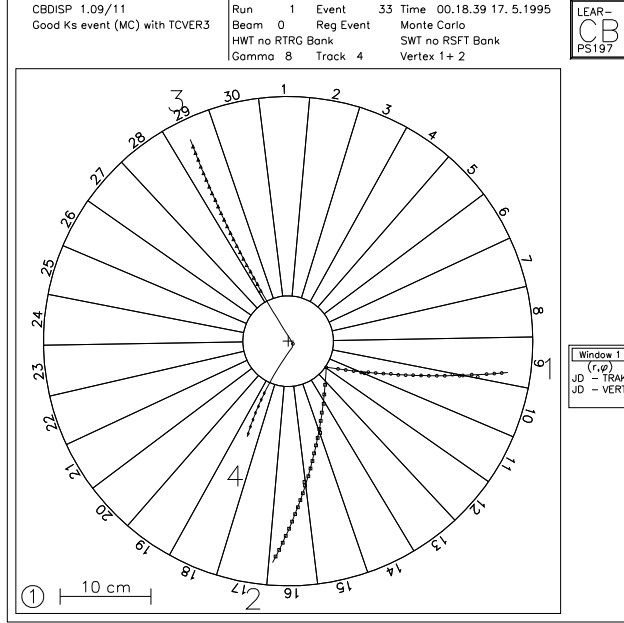


Figure 3.1: An example of a good (2,2) fit to Monte Carlo data

thus needed for two reasons. First, this analysis required a vertex fit that can determine two (or more) simultaneous vertices, which became the “**TCVER3**” routine. Second, because the distance between vertices can be small (down to 1.2 cm), the vertex fit had to be constrained by the original JDC hits, not just the reconstructed helices. This routine was called “**TCVRHX**”. If not, the vertex fit could force true disjoint vertices into a single incorrect vertex. An example of a good fit is shown in figur3.1.

3.2.2 TCVRHX

The new vertex fit code **TCVRHX** implemented a new track-to-hit fitting algorithm, based on the helix fitting code. The geometry of the detector is a cylinder on the \hat{z} axis, with $+z$ the direction of momentum of the incoming \bar{p} beam. The 1.5T magnetic field points in the $-z$ direction (something that wasn’t discovered until the second year of running). The tracks bend in the (x, y) plane, which is defined with $+y$ as vertically up (opposing gravity) and $+x$ is defined through the right-hand rule. In the helix fitting code, each set of hits was fit to a parametric curve of 5 parameters: curvature ($\alpha \sim 1/P_{\perp}$), center of circle in cylindrical coordinates (r_0, ψ_0) , pitch ($\tan \lambda$), and offset in beam direction z_0 . This resulted in 20 parameters for a 4-track event. In the **TCVRHX** fitter, tracks were parameterized as coming from a vertex in space (x, y, z) and then moving with a curvature, azimuth (ϕ_0) and pitch ($\tan \lambda$) (see figure 3.2). Because tracks share vertices, this results in 18 parameters for an event with two vertices with two tracks each, or 15 parameters for a single vertex with four tracks. This method of finding the vertex is superior in finding the true position of the vertex, especially when used with the fine precision of a vertex detector which highly constrain the path of the helices. It is better in distinguishing closely spaced vertices, and the momentum resolution is comparable to the old vertex fit routine.

3.2.3 TCVER3

As a companion to the actually fitting code, a new topology generator and selector was written (**TCVER3**). This routine generates all vertex topologies that are possible from all the tracks of an event. Topologies are written in the following notation:

$$(n_1, n_2, \dots, n_m)$$

where m is the number of vertices and n_i is the track multiplicity of the i^{th} vertex. The n_i are sorted in decreasing order. A track that appears to come from “nowhere” is assigned a vertex multiplicity of 1 and the vertex position is the closest approach to the z -axis. For two-track events, there are only 2 topologies:

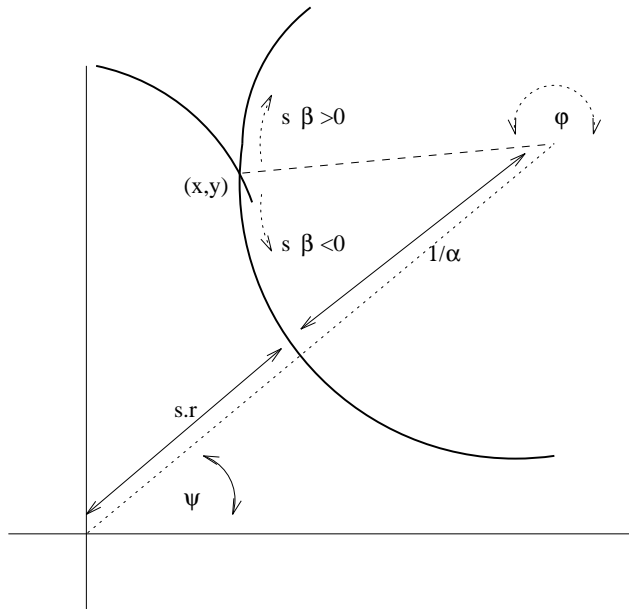


Figure 3.2: The parameterization of the TCVRHX vertex fit.

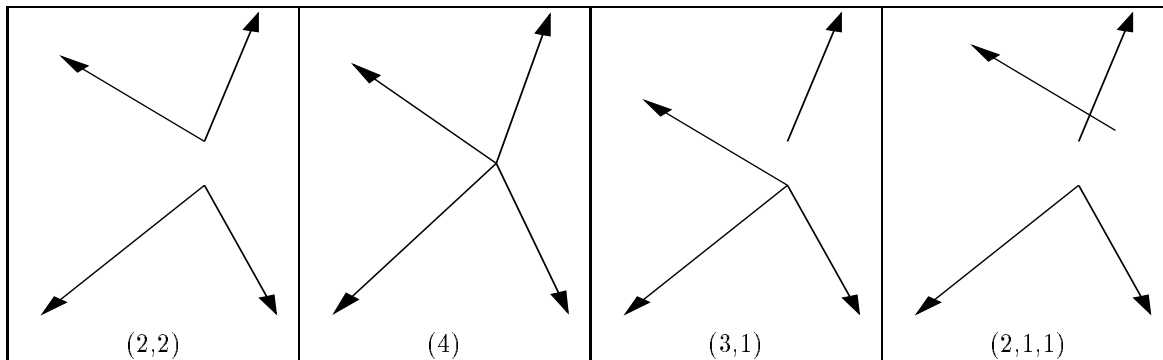


Figure 3.3: Common event topologies. See text for notation

either the tracks come from a common vertex (2) or they don't (1, 1). For three-tracks, there are 3 topologies (1, 1, 1), $3 \times (2, 1)$ or (3), where there are 3 permutations of the (2, 1) topology. For four tracks, there are (1, 1, 1, 1), $6 \times (2, 1, 1)$, $3 \times (2, 2)$ $4 \times (3, 1)$ and (4). See figure 3.3 for a schematic of common topologies for 4 tracks.

The algorithm for finding the “best” topology was designed to be robust and independent on the original order of the tracks. The routine starts by assigning each track to a null vertex. It then forces pairwise sets of vertices together and calls the track fitter. The best pairwise combination of all pairwise combinations is kept, if the χ^2 is below a threshold. This process is continued until no vertices can be compared together than would result in a χ^2 below the threshold. The result of this algorithm is to return the topology with the smallest number of vertices. In order to eliminate some combinations, the user can require that 2-track vertices have zero net charge.

The vertex fit uses the reduced χ^2/N_{df} to determine whether a fit is good or not. Using data with 4 golden long tracks, it was determined that a cut off of $\chi^2/N_{df} < 1.8$ was a good discriminator between the (4) and (2,2) topologies. For $N_{df} \approx 40$, this cut should accept more than 99% of good events. This value was varied to see its effect on the $K_S K^\pm \pi^\pm$ MC. A higher cut off of 3.0 increased the number of accepted (22) events by 5%. This small increase in statistics was not deemed significant enough to merit using 3.0 as the cut off instead of 1.8, since the vertex fit quality of the additionally accepted events was worse.

Additional “outlier” rejection is applied to hits in the vertex fit. In earlier processing, outliers are tagged

Data Type	$S(\sigma_\phi)$	$S(\sigma_z)$
Monte Carlo	0.720	0.840
Real Data	0.952	0.936

Table 3.1: The error scalings applied to the hit errors of real data and Monte Carlo

by assigning an enormous error to it, thereby “effectively” removing the influence of the hit from the fit. However, leaving these outliers in the fit makes the χ^2/N calculation incorrect because N remains the same but χ^2 decreases. Thus these hits are discarded in `TCVRHX`. If the number of “good” hits drops below 10, then the entire track is discarded. This can cause an event with 4-long tracks on input to have only 3 (or less) tracks on output of the vertex fit.

3.2.4 Hit Error Scaling

The vertex fit used the χ^2 value to determine the goodness of fit. A χ^2 calculation depends directly on the estimated errors of the measured values. In this case, the estimated errors are the measurement errors of the JDC hits, measured in two dimensions: the azimuthal ϕ position which is a direct function of the drift time, and the z position which is a function of the charge division measurement. The third position measurement, the radial position of the hit, is a function of the fixed geometry of the JDC fields, and thus does not have significant error compared to the other two measurements. In addition to the small error, because the tracks are mostly radially, the additional constraint on the helical track due to a radial position measurement is minimal. Thus the χ^2 is due only to the ϕ and z errors and not the ρ errors.

The fast Monte Carlo simulation does not simulate the true physics of the ionization due to the track, for example tracking delta electrons, but simply assigns a drift time and z position to the hit. These values are then smeared additionally by a Gaussian to mimic the true data.

Even with this additional smearing, the Monte Carlo is still “too good” compared to the data. To get consistent results, the error estimates of the hits need to be scaled differently so that the final χ^2 distributions take the proper mean. The error scalings S which scale the errors as

$$\sigma'_x = S\sigma_x$$

are given in table 3.1, and the resultant pulls

$$p = \frac{x - \bar{x}}{\sqrt{\sigma^2(x) - \sigma^2(\bar{x})}}$$

are shown in figures 3.4 and 3.5. The pulls as a function of layer number (or equivalently radius) are fairly constant except for the first and last layers. The gap at the 6th layer is due to a missing layer in the JDC.

The pull distributions for Monte Carlo and data are shown in figures 3.4 and 3.5. The pulls are reasonably Gaussian, with no significant mean shift. The ϕ pull distribution deviates from Gaussian slightly, but is satisfactory for this analysis. The width of the z pull distribution is consistent with unity, while the width of the ϕ pull distribution is a little too narrow, and the resultant confidence level distributions are likewise peaked towards high confidence levels. To smooth out this effect which is a result of experimental errors being estimated too large, the experiment errors of the ϕ position are scaled. This results in a flat confidence level for the χ^2 of the individual hits (with 2 degrees of freedom). The scalings for Monte Carlo and data are given in table 3.1. The global scaling is applied to all other scalings.

The reconstruction accuracy is shown in figure 3.7 where the vertices V0 and V1 of Monte Carlo generated events are plotted. The differences to the reconstructed vertices are shown as short line segments. The majority of vertices are correctly reconstructed. The errors are well described by the statistical fitting errors and a the variation induced by multiple scattering between the JDC and the target. The pulls for the kinematic fit, which depends on the 3×3 error matrix of the momentum for each track, are shown in figure 4.14.

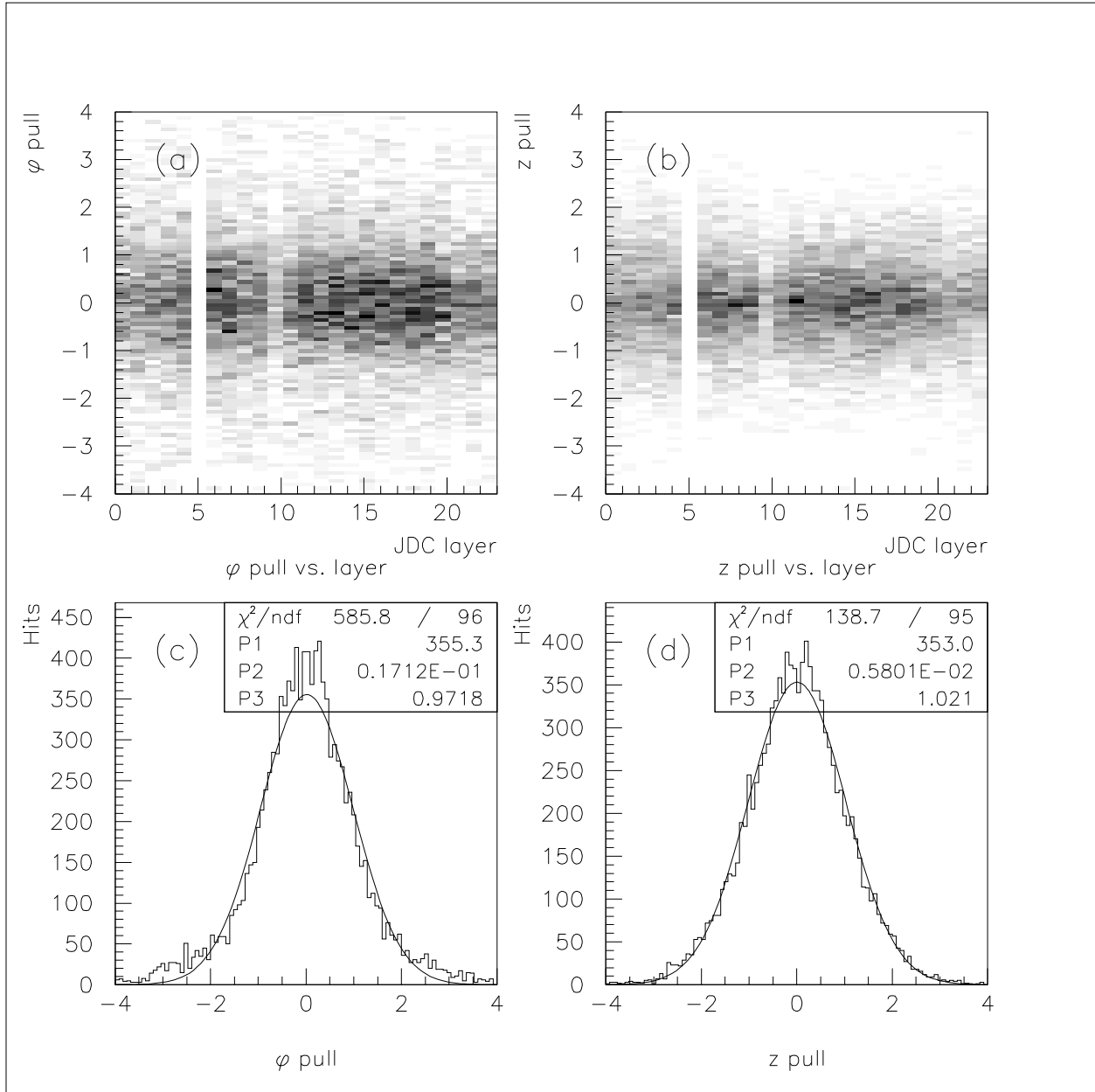


Figure 3.4: Vertex fit pulls for MC. (a) The ϕ pull versus layer number, (b) The z pull versus layer number, (c) The ϕ pull with superimposed Gaussian fit, (d) The z pull with superimposed Gaussian fit

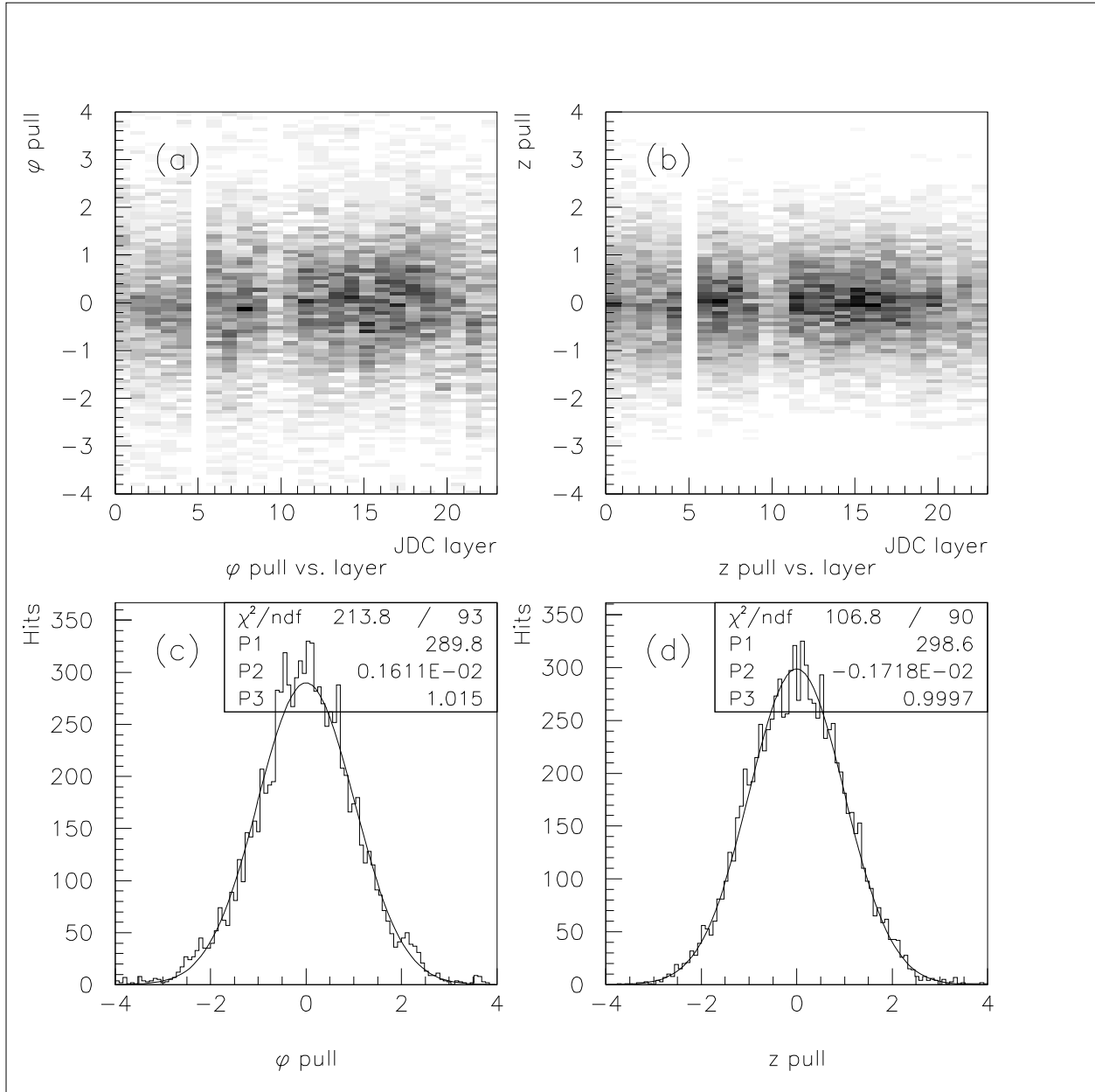


Figure 3.5: Vertex fit pulls for real data. (a) The ϕ pull versus layer number, (b) The z pull versus layer number, (c) The ϕ pull with superimposed Gaussian fit, (d) The z pull with superimposed Gaussian fit

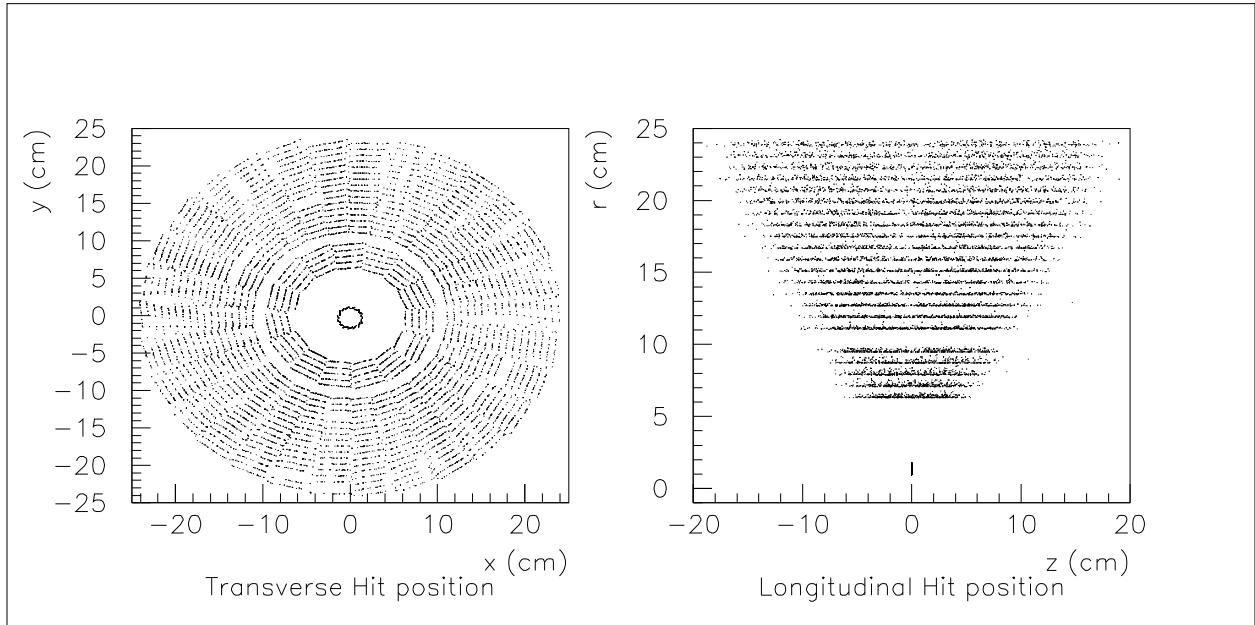


Figure 3.6: The position of the hits used in the vertex fit. (a) the $\phi - \rho$ projection. The gap at $\rho = 10$ cm is due to the missing 6th layer in the JDC, while the small ring at the center is due to the SVX. (b) the $z - \rho$ projection. The vertical line at the bottom is due to the SVX which has no z resolution.

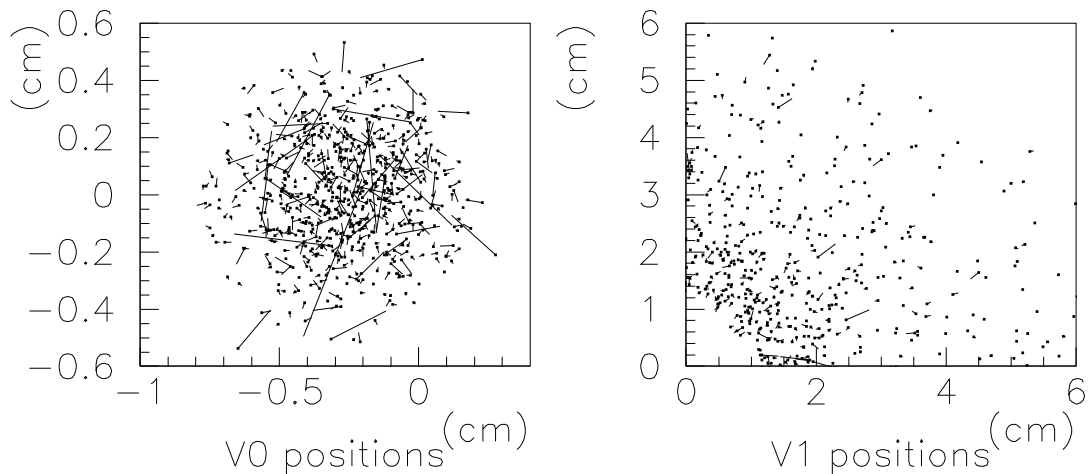


Figure 3.7: The reconstruction accuracy of the vertex fit. The Monte Carlo generated vertices as small squares and connecting line is drawn to the reconstructed vertex position. Note the difference in scale for the two plots of the V0 and V1 vertices, and that only one quadrant of the detector is shown for V1.

3.3 KinFit - General Kinematic Fitter

One of the new classes of `cb1b1++` is `KinFit` which is a general kinematic fitting algorithm. A kinematic fit is a technique where the measured particle 4-momenta are improved by applying constraints to ensembles of the momenta and varying the momenta slightly to satisfy these constraints. Typical constraints include

1. the total energy of an ensemble of particles
2. the total momentum of an ensemble of particles, either in magnitude or in each spatial component.
3. invariant mass of an ensemble of particles

There are two other uses of the kinematic fit besides improving momenta. The first is to do π^\pm/K^\pm particle ID on an unidentified charged track. Because the π^\pm and the K^\pm have different masses, the total energy of a set of tracks depends on the identification of the track as a π^\pm or K^\pm . By testing both hypotheses in a kinematic fit and looking for the lower χ^2 or higher confidence level, the identity of the tracks can be determined usually, unless the momenta of the two tracks are the same. We do not use the kinematic fit for the actual particle identification (this is done by dE/dx), but for particle identification validation.

The second use of a kinematic fit is to test the hypothesis of one or more missing particles. For example, a soft $\pi^0 \rightarrow \gamma\gamma$ could escape the detector through the end gaps. A kinematic fit of an event with a lost particle will typically be much worse than of an event with all particles seen.

For $p\bar{p}$ annihilations at rest, the total energy and momentum components are known. They are $E = 1876$ MeV and $\vec{p} = 0$. Typical invariant mass constraints are applied to gamma-gamma pairs to constrain the mass to the π^0 mass (139 MeV) or η mass (547 MeV). Another mass constraint is applied to $\pi^+\pi^-$ or $\pi^0\pi^0$ pairs to the K_S mass (497 MeV). In the case of the later pair, where the $\pi^0 \rightarrow \gamma\gamma$, two levels of mass constraints can be imposed.

In `KinFit`, one constructs a hypothesis using the `Particle` class. The annihilation ensemble is assigned to a pseudo-root particle called “pbarp” with mass of 1876.54 MeV. This root particle then decays into two or more daughter `Particles`, which can further decay if necessary. Then, each data event is constrained to this hypothesis, with a χ^2 calculated based on the following constraint equations f :

$$\Sigma_\alpha p_i^\alpha - p_i^{\prime\prime\prime} = f_i = 0 \quad (3.1)$$

$$\frac{m_\beta^2 - m_{0\beta}^2}{2m_{0\beta}} = f_\beta = 0 \quad (3.2)$$

where α runs over all final-state particles (the leaves at the end of the decay tree), i is x , y or z , β runs over the mass constraints of intermediate particles, m_β and $m_{0\beta}$ are the measured and correct invariant masses, respectively, of the β intermediate particle. In this analysis, there are four measured tracks, so four terms in the momentum sum. Also, there is one mass constraint on the $K_S \rightarrow \pi^+\pi^-$ decay, where $m_{0\beta} = 497$ MeV/ c^2 for the $\pi^+\pi^-$ pair.

The details of the fit algorithm are given in appendix 10.

3.4 awp - Partial Wave Analysis

The software for the partial wave analysis was called `awp` (a reversal of the acronym for what it does). It originally began as a program written in FORTRAN, and then translated by hand into C++. Unfortunately, the translation was impenetrable gibberish, and did not take into any of the features of object oriented programming. In an effort to understand all of the details of the partial wave analysis, the entire program was rewritten from scratch using C++ objects.

The theoretical physics details are given in the partial wave analysis, chapter 7. Here we describe the software interface. The input file outlines the structure of the partial waves for each Dalitz plot. The form is given here abstractly:

```
PWA {
  ResonanceDefinition
  ResonanceDefinition
```



```

ResonanceDefinition
...

DalitzPlot {
  InitialState {
    FinalState {
      ResonanceProduction
      ResonanceProduction
      ...
    }
    FinalState
    ...
  }
  InitialState
  ...
}
DalitzPlot
...
}

```

The program first reads all external histograms into memory, and then calculates the spin-parity functions for each bin for each initial state and final state. These values are cached. Then control is given to MINUIT[40], which calls `awp` to numerically calculate the second derivative matrix of the log-likelihood, and then varies the parameters in order to minimize the negative log-likelihood. The source code is attached in the enclosed CDROM.

Some of the features are

1. Free or constrain an overall fudge function of arbitrary polynomial order. This feature is used to take care of any discrepancies between the Monte Carlo and real data.
2. Ability to set two or more production amplitudes to the same value. This is used to constrain the two $K\pi$ axes to the same production strength.
3. Ability to constrain the percentage of each of the different initial states, for example constraining P -wave annihilation to 10% of the total Dalitz plot.

The textual output of the program is in the same format as the input, so the output can be slightly edited and then resubmitted to the program. The histograms are outputted in a private format, and printed using a custom program that generates the postscript directly, to avoid using any of the CERNLIB libraries.

Chapter 4

Data Selection

This chapter reports on the steps taken in the data collection and data reduction. We discuss the online trigger, the event reconstruction, and the four stages of processing from the raw data to the final Dalitz plot. Table 4.1 gives the event statistics at the end of each stage.

4.1 K_S Trigger

The general trigger system is discussed in the detector chapter. Here we give a description of the specific K_S trigger.

A K_S decays into $\pi^+\pi^-$ with a branching ratio of 69%. In this reaction, $K_S K^\pm \pi^\mp$, the $K^\pm \pi^\mp$ tracks originate from the original annihilation point, forming a 2-prong vertex there. The $K_S \rightarrow \pi^+\pi^-$ forms a second vertex at a typical radius given by $c\tau = 2.6762$ cm. The momentum-dependent mean path length of a decaying particle is given as

$$d = \tau \frac{p}{m}$$

where τ is the particle's rest frame lifetime, p is the particle's momentum and m is the particle's mass. This formula takes into account the effects of velocity ($\beta = p/E$) and the relativistic time-dilation ($\gamma = E/m$). Because the detector is in a cylindrical configuration, the crucial distribution is in r_\perp , which is shown in figure 4.1. This is not a pure exponential decay distribution, because the proper time (lifetime in the K_S rest frame) is momentum dependent. However, a plot of the proper time would also not be a pure exponential, because of the radial cut imposed by the SVX.

The Silicon Vertex Detector (SVX) was used as the main tool for determining the K_S vertex, because of its close proximity to the annihilation point. It sits at radius 1.2 cm, which is just slightly larger than the liquid hydrogen target. A K_S that decays outside of the SVX will leave no signal, while other tracks originating from the annihilation vertex will leave a hit in the SVX with high probability.

The trigger was run with two independent configurations. If the criteria of either configuration were met, the event was written to tape. The first configuration was designed to trigger on events with one or more K_S 's outside of the SVX and no other tracks, and was named "0→2" meaning 0 charged tracks inside the SVX and 2 (or more) charged tracks outside the SVX. The 0→2 trigger would select events of the type

$$\begin{aligned} p\bar{p} \rightarrow K_S K_L \pi^0 & \quad p\bar{p} \rightarrow K_S K_S^n \pi^0 \\ p\bar{p} \rightarrow K_S K_L \pi^0 \pi^0 & \quad p\bar{p} \rightarrow K_S K_S^n \pi^0 \pi^0 \end{aligned}$$

Stage	Description	Events	rel. fraction
0	Trigger	9,448,575	—
1	K_S skim	2,300,360	24 %
2	Energy/Momentum	287,400	12 %
3	Vertex reconstruction	118,372	42 %
4	Particle ID and Kinematic Fit	57,099	48 %

Table 4.1: An overview of the statistics at each processing stage

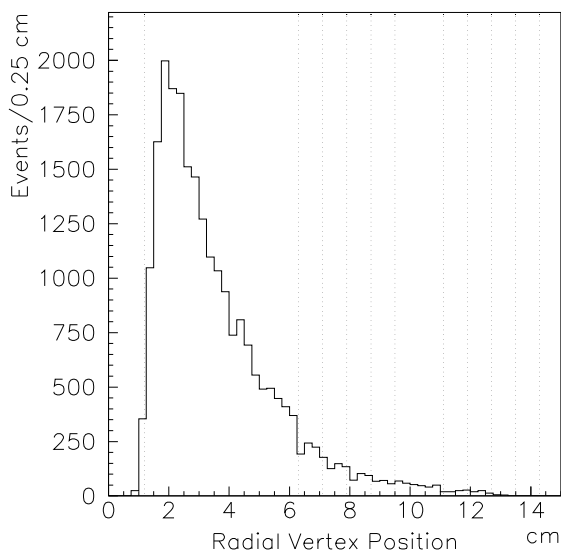


Figure 4.1: The distribution of radial ($r = \sqrt{x^2 + y^2}$) positions of the K_S decay vertex. The vertical lines indicate the radial positions of the SVX and the first 10 layers of the JDC.

where K_S^n indicates the K_S in its neutral decay mode, $K_S \rightarrow \pi^0 \pi^0$.

The second configuration was designed to trigger on events with one or more K_S 's outside of the SVX and either 1 or 2 tracks inside the SVX, and was named “2→4” meaning 2 (or one) charged tracks inside the SVX and 4 (or more) charged tracks outside the SVX. The 2→4 trigger would select events of the type

$$\begin{array}{ll}
 p\bar{p} \rightarrow K_S K^\pm \pi^\mp & p\bar{p} \rightarrow K_S K_S \pi^0 \\
 p\bar{p} \rightarrow K_S K^\pm \pi^\mp \pi^0 & p\bar{p} \rightarrow K_S K_S \pi^0 \pi^0 \\
 p\bar{p} \rightarrow K_S K_L \pi^\pm \pi^\mp & p\bar{p} \rightarrow K_S K_S^n \pi^\pm \pi^\mp
 \end{array}$$

The reaction of this thesis is the first one listed in the later configuration.

The hardware trigger consists of a set of discriminators hooked to the signal outputs of the SVX and JDC. The SVX has a fine-grained front side, with 128 wires spaced a few hundred microns apart. However, the readout is too slow for a fast trigger, so instead the back side of the SVX is used for triggering. The backside is simply the common current drain, so it acts as a logical OR of all 128 front-side wires. The JDC sense wires are readout by flash ADC's whose analogue output is discriminated by the trigger system.

The hardware trigger consists of a system of programmable logic units (PLU's) connected to multiplicity counters. The multiplicity counters work by analogue summing of the discriminated signal of all 30 JDC sectors of a particular layer. The sum is digitized and converted to an integral value for the PLU's. The PLU's output goes high when the integer count on its input lie between two predefined values.

The specific trigger condition for the 0→2 trigger was exactly 0 hits in the backplanes of the SVX, and 2 or 3 hits in each of JDC layers 19 and 20. The specific trigger condition for the 2→4 trigger was exactly 1 or 2 hits in the backplanes of the SVX, and 3 or 4 hits in each of JDC layers 9 and 10, and exactly 4 hits in each of JDC layers 19 and 20. These two conditions were part of trigger **ksh44_v2**.

During the run, it was decided to modify **ksh44_v2** slightly by adding a third condition. The SVX backplanes overlap significantly in order to make up for the fact that the pitch of the planes opens gaps between them. However if a particle moves purely radially, it can travel through two backplanes in the overlap region, and this would cause an increase in backplane multiplicity. To recover these events that would otherwise be rejected by the 2→4 trigger, a third condition allowed three backplane hits, as long as there was also a signal in the front-plane in the overlap region, which was about 13 wires wide. This revised trigger was named **ksh44_v3**.

Data taking occurred during the April 1996 run period at the LEAR ring at CERN, from April 13 to May 6. In addition to the **ksh44_v2** and **ksh44_v3** triggers, 4-prong and minimum bias triggers were also taken,

for absolute rate calculations and efficiency corrections. This data was recorded on 26 Digital Linear Tapes (DLT's) with 10 GB of data on each. These were copied and brought to Berkeley for further processing.

4.2 Reconstruction and Skimming Stage

The first stage of processing is reconstruction, followed by cuts to reject events that probably do not contain useful information, resulting in a summary data set of good K_S candidates. Reconstruction is the process of decoding the raw data and extracting the momenta of the measured particles. This data processing stage is the most CPU intensive because it involves the full data set and the charged tracking algorithm (Fast Fuzzy Radon) requires a lot of calculations. The cuts used to remove poor events are described below.

4.2.1 Reconstruction Performance

Some distributions of important event parameters, including the number of reconstructed tracks (all tracks, just long tracks and the charges of the tracks), the total energy and momentum of the event, and the momenta of all charged particles and of all photons, are given in figure 4.2. The sharp peaks in the track multiplicities are at four, which is exactly what was expected coming from the trigger. Most of the events contain two positive and two negative tracks. Most of the tracks are fully contained by the detector as evidenced by the peak in the momentum vs energy plot (see figure 4.2 (d)) which peaks at near zero momentum and around 1900 MeV energy, exactly that expected from $p\bar{p}$ annihilation. The charged track momenta peak at 200 MeV, while photon energy peaks at the lower reconstruction threshold. This is to be expected because by selecting 4 charged tracks, there is little phase space left for any neutral particles.

The invariant mass and opening angle of pairs of $\pi^+\pi^-$ are shown in figure 4.3. A peak is clearly seen at the K_S mass of 497 MeV (figure 4.3 (a)). There is also a large broad combinatorial background, as well as a large spike at $2m_\pi$. This spike is correlated to the spike in the angular distribution (figure 4.3 (b)) at $\cos(\theta) = 1$. These events are gamma conversions, $\gamma \rightarrow e^+e^-$, that occur on the JDC field and sense wires or on the inner wall. This background is easily removed at a later stage.

The stability of the data is good over the 3 week period that the data was taken, as seen in the many faces of figure 4.4. Figure (a) shows the number of 2 \rightarrow 4 triggered events per run; the large step near run 35800 is a result of the trigger definition change. The gaps are simply runs that were not taken with the trigger.

In Figures (b),(c),(e), and (f), one can see a slight hiccup in trend (up for energy and momentum (b,c), down for efficiencies (e,f)) which is most likely due to variations in the barometric pressure at the experiment. Because the JDC is very fragile, the Isobutane/CO₂ gas within is held at atmospheric pressure. Most of this variation is corrected by the reconstruction software, which takes into account the pressure. The momentum accuracy is corrected to greater degree than the absolute acceptance.

In figures (d,e,f), the relative efficiencies of the first selection criteria are shown. The change in efficiency in (d) is due to the change of trigger, which shows that the data was positively enriched by the change, which was intended.

In figures (g,i), one can see a spike near Run 35450 in the number of hits per track and the dE/dx values. We determined that this spike was caused by a faulty gas flow meter or pressure gauge. At the time of the spike, the ratio of CO₂ to isobutane dramatically increased. The problem was resolved during the periodic inspection during data taking, but it took much longer for the gas mixture to readjust to the proper ratio. When the CO₂ level increases, the gain of the JDC increases, resulting in bigger signals (leading to bigger measured dE/dx values) and more hits being seen. The dE/dx values were corrected later on, described in section 4.5.

In figures (j,k,m,n), the first and last layer of hits of a track are seen, and these are in good condition. There is a small gap in the "first layer" histogram (fig k), which is caused by a slight misalignment between in the inner and outer sections of the JDC, but this is not a major problem. Note that fig (j) shows the *average* first layer of all tracks in a run; the average is higher than "1" as can be seen in (k). For the purpose of stability checks, figures (j,m) are nicely stable. In figures (l,o), the number of low momentum and high momentum tracks per event are stable.

4.2.2 Skimming cuts

1. **2 \rightarrow 4 selection.** Because the data contains two triggers (0 \rightarrow 2 and 2 \rightarrow 4), the first step is to extract

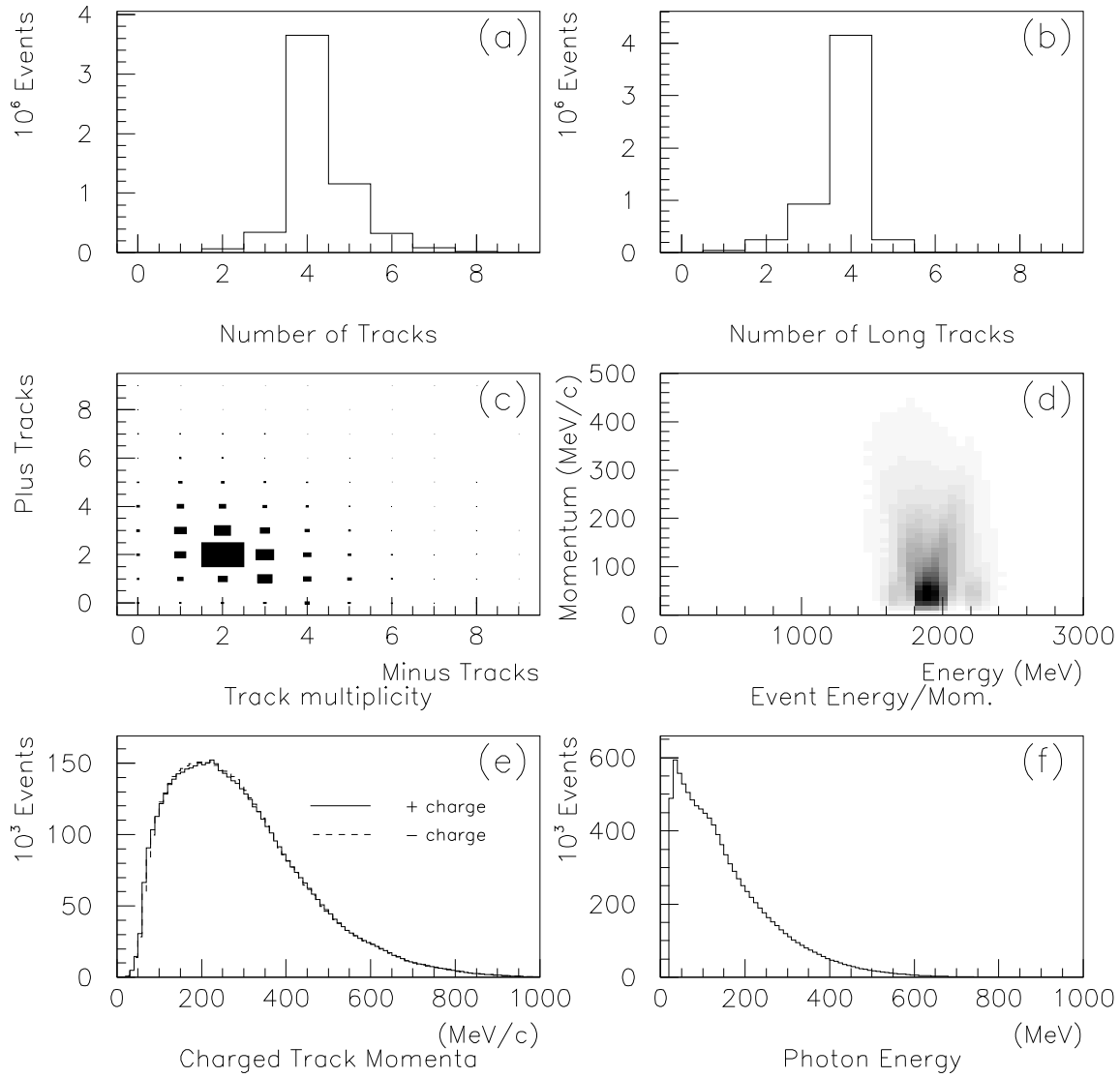


Figure 4.2: Various distributions of important event parameters of the triggered data

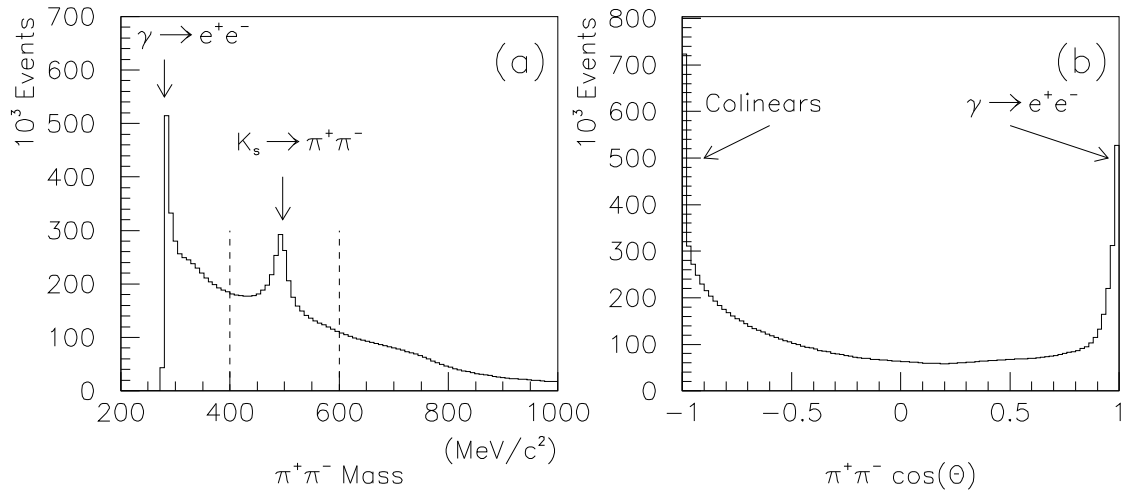


Figure 4.3: (a) The invariant mass of all $\pi^+\pi^-$ pairs. (b) The opening angle of all $\pi^+\pi^-$ pairs.

the desired trigger ($2\rightarrow 4$) and only process those events. This is to save some reconstruction time since 33% of the data is the $0\rightarrow 2$ trigger.

2. **Exactly 4 Long tracks.** This cut requires exactly long tracks (with at least 10 hits) and exactly no short tracks (with no more than 9 hits).

From previous experience with reconstructed charged tracks, tracks need at least 10 hits to have a reasonable reconstruction accuracy, even though the helix fit only requires 5 hits. Requiring long tracks of untriggered data typically reduces the solid angle acceptance, since polar-directed tracks can not hit many layers before exiting the JDC. However, the long track condition was already part of the trigger specification, so this cut does not reduce the statistics greatly.

Many events have “splash-back” tracks which typically originate from interactions of hadrons with the crystals. These junk tracks are not part of the desired physics and in principal could be ignored. For two reasons, however, they are not ignorable. First, the junk tracks tend to mess up the reconstruction of the other “good tracks”. Second, if one accepts events with extra unidentified tracks, one is opening up the probability of increasing background. Using Monte Carlo simulation (see chapter 5), we found that allowing one short track (that was ignored) increased the signal statistics at the skimming level by 10%. We felt that this small gain was not significant when compared to possible problems with extra background and later data reconstruction.

This cut rejects 43% of all the events of the data, and 22% of the signal as calculated via Monte Carlo.

3. **2 positively-charged and 2 negatively-charged long tracks.** Because the $p\bar{p}$ has zero net charge, this cut is natural. The events that are rejected could come from 3 sources:
 - (a) $p\bar{p}\rightarrow 6$ tracks, where 2 positive or 2 negative tracks were lost down the polar directions,
 - (b) pile-up events, where two annihilation events occur so near in time that drift electrons from the previous event linger into the next event causing spurious readings, and
 - (c) reconstruction errors which assign the wrong curvature to a track.

This cut rejects 14% of the data, and 6% of the signal as calculated via Monte Carlo.

4. K_S mass cut. This last cut was chosen for a technical reason rather than for physics reasons: It was desired to fit the entire skimmed data on one 20GB tape. Without this cut (which rejects 14% of the data), the result would not fit on one tape.

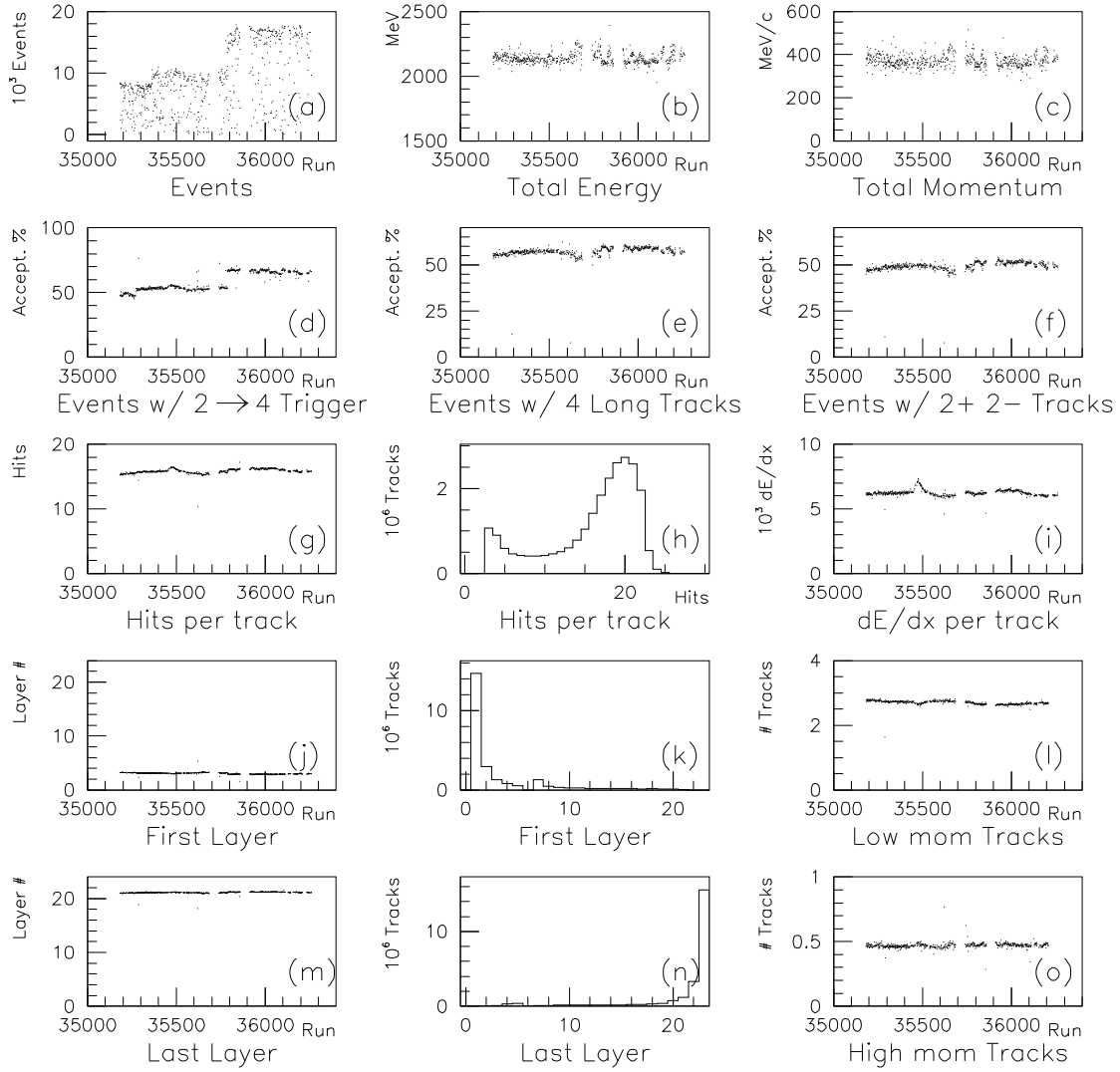


Figure 4.4: Stability checks versus run number.

The mass of the K_S is 497 MeV, and thus the invariant mass of the decay products ($\pi^+\pi^-$) should be 497 MeV. However, because the vertex of the decay products was not known at this stage in the data processing (the vertex fit was not completed), the correct invariant mass could not be calculated. So an approximation was made by assuming that the vertex position was at the annihilation point. This approximation is worst for true decay vertices that are far away, but only affects the angle between the two pions and not the momenta. Because of the approximation, the mass window was chosen to be much larger than the true experimental width of the K_S .

This cut required at least one pair of $\pi^+\pi^-$ (4 possibilities) to have a mass between 400 and 600 MeV/ c^2 . This only rejects 1% of Monte Carlo events, while rejecting 14% of data events, which was sufficient to have the output data fit on one tape. The larger rejection fraction is due to much more background in the data, for example from gamma conversion ($\gamma \rightarrow \eta^+e^-$).

4.3 Energy and momentum selection

The first pass on the data described in section 4.2 was intended to be a general “good event” selection, but did not specifically select the channel $K_S K^\pm \pi^\pm$.

The channel $K_S K^\pm \pi^\pm$ consists pure of 4 charged tracks and no photons. Because of this, we could ignore the crystal calorimeter (except much later when it is used as for an anti π^0 cut). The momenta of the charged tracks is well defined (by the curvature and pitch of the helix), but the energy ($E = \sqrt{m^2 + p^2}$) is not because the particles have not been identified as pions or kaons and thus the mass is unknown. For high energy particles, the energy asymptotically approaches the magnitude of the momentum, but in the case of $p\bar{p}$ annihilation, the mass is important.

To select good $K_S K^\pm \pi^\pm$ events, the magnitude of the total momentum

$$|\vec{p}_{\text{tot}}| = \left| \sum_{i=1,4} \vec{p}_i \right| < 180 \text{ MeV}/c^2$$

was required to be less than 180 MeV/ c , in concordance with at rest annihilation. By assuming that all particles are pions, a fake energy E' quantity can be calculated as

$$E'_{\text{tot}} = \sum_{i=1,4} E'_i$$

$$E'_i = \sqrt{\vec{p}_i^2 + m_\pi^2}.$$

Through Monte Carlo simulation, the minimum value of E'_{tot} for $K_S K^\pm \pi^\pm$ is 1400 MeV, where the shift in energy from $2m_p = 1876$ MeV is due to one particle being misidentified as a pion rather than kaon. Thus all events were required to have an E' greater than 1400 MeV. Figure 4.5 shows the energy and momentum, and the cut limits.

In figure 4.5.a, there are five features of note. The desired signal lies at **A**, which shows full conservation of energy and momentum. At feature **B** are events of the type $\pi^+\pi^+\pi^-\pi^-$, for example from $K_S K_S$. These lie at the true energy and momentum conservation spot because no tracks are kaons misidentified as pions. At feature **C**, are events of the type $K_S K^\pm \pi^\pm \pi^0$, where the neutrally decaying π^0 appears as missing momentum. The narrow diagonal blob of **C** can be extrapolated to feature **A** by following the slope. This implies that the in both **A** and **C**, one of the tracks is truly a kaon and not a pion. Feature **D** are due the events with one massive lost particle (not a pion) and perhaps other lost neutral particles. If the event truly contains a K_S seen by the trigger, then the lost massive particle is most likely K_L . for example $K_L K_S \pi^+ \pi^-$. Extrapolating this blob to 0 momentum does not intersect **A**. Because feature **E** does not have an axis pointing diagonally down, it is due to more than one lost or neutral particle, for example $K_S K^\pm \pi^\pm \pi^0 \pi^0$.

4.3.1 Statistics

13.9 Gigabytes of skimmed data were read and 1.75 GB (12.6%) of data with proper energy and momentum were written to Exabyte. The number of runs used was 709.

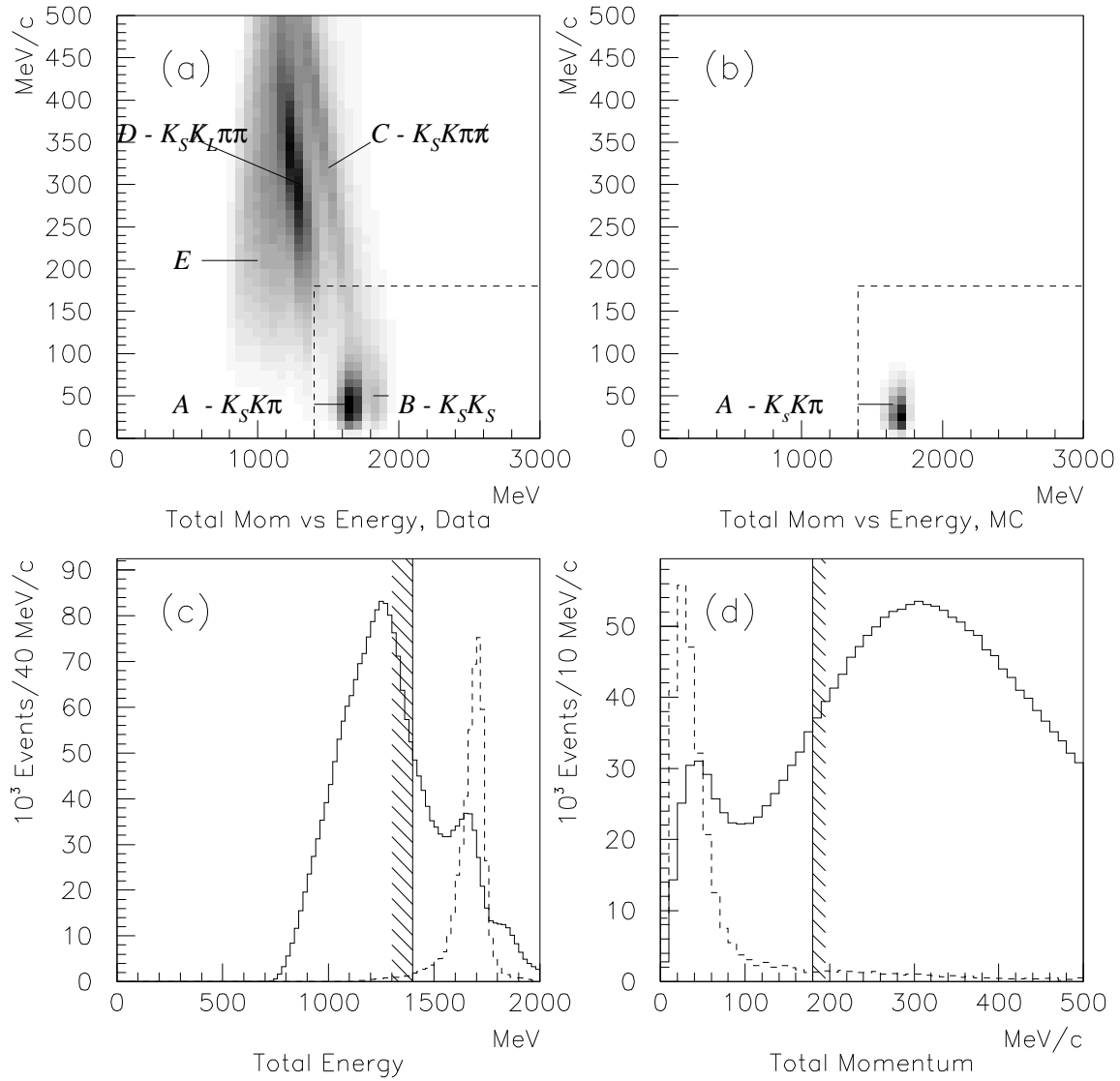


Figure 4.5: Cuts on total energy and momentum. (a) The total energy vs total momentum plot for data. (b) The total energy vs total momentum plot for Monte Carlo of $K_S K^\pm \pi^\pm$. (c) The total energy with data drawn as a solid line, the MC drawn as a dashed line, and the cut limit. (d) The total momentum, with same definition as (c).

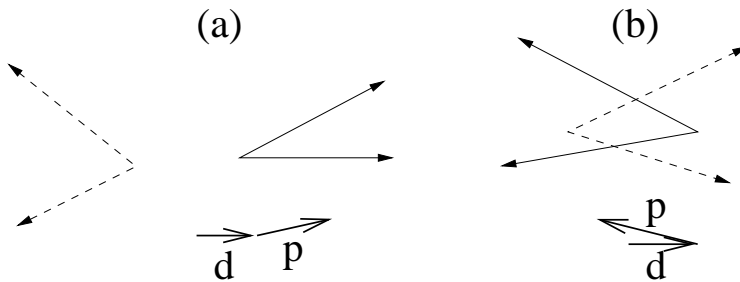


Figure 4.6: (a) A properly reconstructed vertex configuration. $\vec{p} \cdot \vec{d} > 0$. (b) A improperly reconstructed vertex configuration. $\vec{p} \cdot \vec{d} < 0$.

Cut	Events	Net %
Event Read	2300360	100.0
Momentum Cut	449653	19.5
Energy Cut	287400	12.5

A few runs after this step were removed because either (a) they were the wrong trigger type, (b) the antiproton beam conditions appeared to be bad based on gross asymmetries in the crystal hits, or (c) the SVX did not appear to be working. This accounted for a removal of only 318 events out of 287400.

4.4 Vertex fitting

The third data selection operation was vertex fitting and selection. This involves running the specially written multi-vertex fitter, fine tuning the fit parameters(see section 3.2), and selecting the desired topology.

The vertex fit takes the results of the helix fit and combines tracks pairwise to see if they come from a common vertex. An overview of the special vertex fit and a description of the topology notation is given in section 3.2.

The desired event topology is an inner vertex due to the charged kaon and the charged pion, and an outer vertex due to the decay of the K_S into two charged pions. Thus we select events with a topology equal to (2,2). See figure 3.3 for a schematic of common topologies. At this point, the two remaining vertices are sorted by their radial distance to the origin. The inner vertex is labeled V0 and the outer vertex is labeled V1.

The third cut requires that the vertices open in the correct direction relative to the annihilation vertex. Because the K_S is moving away from the annihilation vertex, the momentum of V1 must point away from the annihilation vertex. However, sometimes there is rare condition where the tracks are accidentally paired to a fake set of vertices which are pointing the wrong way, see figure 4.6. The cut is calculated as follows. First the mean position of V0 and V1 is calculated as

$$x_{\text{center}} = \frac{1}{2}(x_0 + x_1).$$

Actually, any point lying on the line connecting the two vertex positions would work for this cut, since we are just interested in the unit direction vectors from this point to each vertex. For each vertex $i = 0, 1$, a direction vector is then defined

$$\vec{d}_i = \vec{x}_i - x_{\text{center}}$$

and the cosine of the angle between this direction vector and the momentum of the vertex,

$$\vec{p}_i = p_i^{\pi^+} + p_i^{\pi^-},$$

is required to be greater than zero,

$$\vec{p}_i \cdot \vec{d}_i > 0.$$

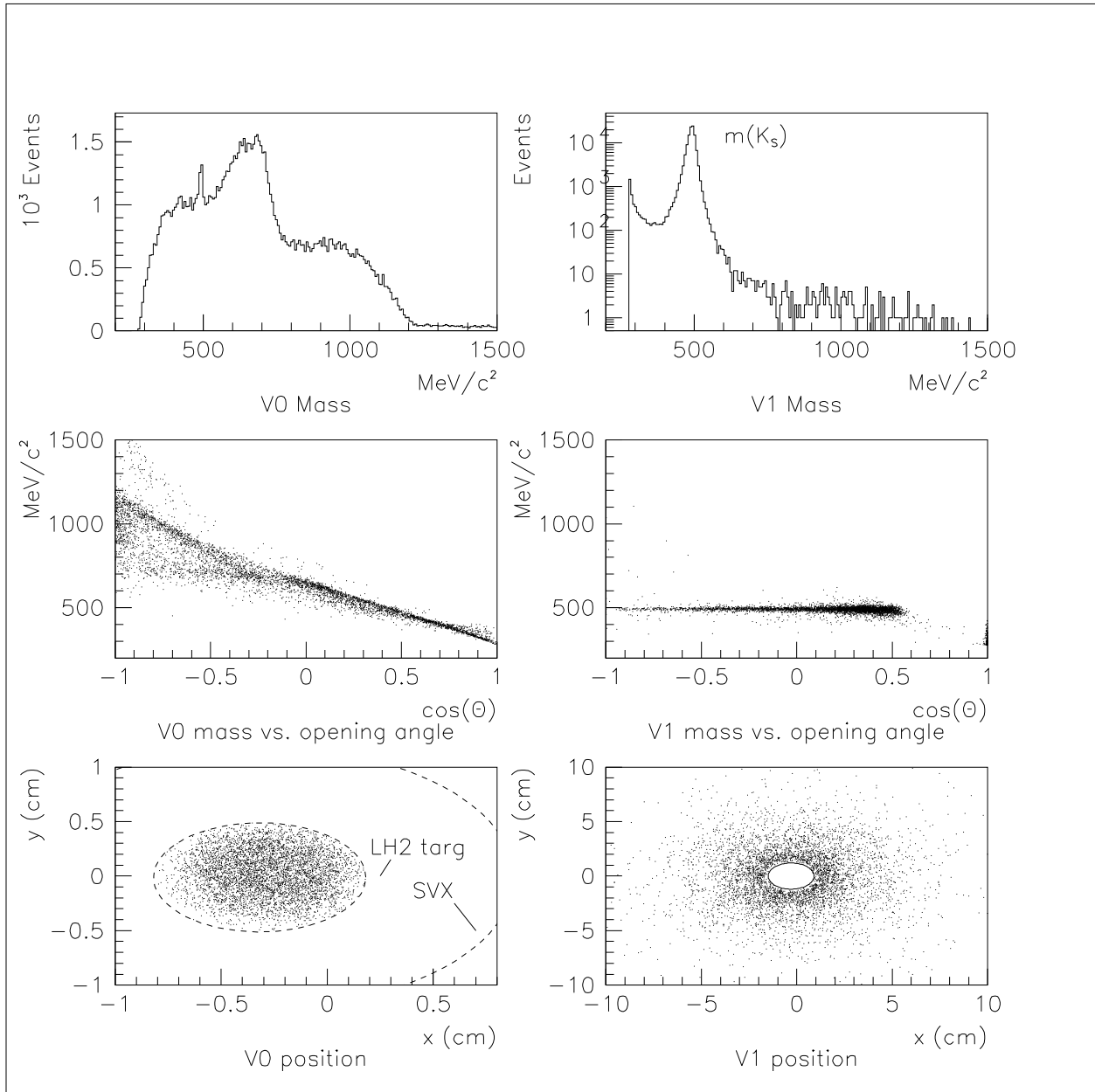


Figure 4.7: The reconstructed vertices. The left column is for the inner vertex, V0, and the right column is for the outer vertex, V1. (a,b) The invariant mass of the $\pi^+\pi^-$ pair at the vertex. The large peak in (b) is due to the K_S . (c,d) The invariant mass vs. the cosine of the angle between the $\pi^+\pi^-$. (e,f) The (x, y) position of the vertex, with the target and SVX boundaries drawn.

The next cut required that all SVX hits be assigned to the reconstructed tracks. The efficiency of the SVX is higher than the efficiency of the JDC, so it possible for short tracks to be seen in the SVX but not reconstructed properly because some of the JDC hits were below threshold.

The next pair of cuts required the inner vertex, V0, to lie within 0.5 cm of the axis of the LH₂ target, which was centered at (-0.31864, -0.01232, 0), and required the outer vertex V1 to lie outside of the SVX cylinder boundary, with a transverse radius of 1.2 cm.

4.4.1 Statistics

The event counts for the real data and the Monte Carlo of $K_S K^\pm \pi^\pm$ are given in table 4.2. The most important cut is cut # 2 which requires exactly two distinct vertices. Most of the reject real data events are of the topology (4), which means that the event was most likely a $p\bar{p} \rightarrow \pi^+ \pi^+ \pi^- \pi^-$ event that leaked passed the SVX at the trigger level. The reason that the “Real data” column does not follow the “ $K_S K^\pm \pi^\pm$ MC” column is that there are still background events in the real data, which are not removed until after the kinematic fit.

NB: An updated JDC calibration database was used at this step of the real data processing. Because the tracks were reconstructed again with the new calibration, some new tracks were found and some old tracks were lost. This explains the > 4 track statistics in table 4.2, which account for less than 0.5% of all events. The < 4 track statistics are due to 2 reasons. The first is due to the new database. The second is that some tracks are rejected in the vertex fit if there are too many “outlier” hits.

4.5 Particle identification using Energy Loss (dE/dx)

At this stage of the analysis, there are exactly four reconstructed charged particles, with two originating from the annihilation vertex and two originating from a displaced vertex outside of the target region. The only possible long-lived, charged particles allowed in this energy range ($E_{\text{tot}} < 1876$ MeV) are pions, kaons and electrons.

Direct $p\bar{p}$ annihilation into electrons is highly unlikely; the strong color force dominates annihilation processes. The branching ratio $\text{BR}(p\bar{p} \rightarrow e^+ e^-) = 3.2 \times 10^{-7}$ [15] is several orders of magnitude less than the reactions of interest, for example $\text{BR}(p\bar{p} \rightarrow K^0 K^{0*}) = 1.6 \times 10^{-3}$ [15]. Electrons are formed however through photon conversion on the JDC sense or field wires. The process creates a displaced vertex, but because of the zero mass of the photon, these vertices ($\gamma \rightarrow \eta^+ e^-$) have a $\theta = 0$ opening angle, and are kinematically easily separated from $K_S \rightarrow \pi^+ \pi^-$.

The remaining track identification problem is between kaons and pions. At this energy scale, the outer V1 vertex can only be due to the decay of a K_S or a photon conversion, so the tracks originating from V1 are not kaons. By strangeness conservation, there must be an even number of kaons. There is no phase space for $p\bar{p} \rightarrow 4K$, so events are limited to only 2 kaons with 0 or more pions. The tagged K_S is one of these kaons. The other kaon could be K^\pm , K_S , K_L . Thus the inner vertex V0 could be $\pi^\pm \pi^\mp$ with a missing kaon (and zero or more missing pions), or $K^\pm \pi^\mp$ with zero or more missing pions.

4.5.1 $K_S K_L X^0$

The background channel with $X^0 \rightarrow \pi^+ \pi^-$

$$p\bar{p} \rightarrow K_S K_L \pi^+ \pi^-$$

would give two tracks at the inner vertex. However, the missing mass of the K_L makes it very unlikely to pass the kinematic fit. Events with additional neutral particles are suppressed even more by the kinematic fit.

4.5.2 $K_S K_S X^0$

In this reaction, the second K_S decays quickly inside the target region into $\pi^+ \pi^-$. From figure 4.7, a small narrow peak (about 500 events) at $m(\pi^+ \pi^-) = 497$ MeV can be seen in the V0 Mass plot. Background events of the type

$$p\bar{p} \rightarrow K_S K_S \pi^0$$

#	Cut	Real data		$K_S K^\pm \pi^\pm$ MC	
		Events	%	Events	%
1	Event in	287092	100	33692	100.0
2	type (2,2)	153908	53.6	27389	81.3
3	$\vec{d} \cdot \vec{p} > 0$	141567	49.3	26515	78.7
4	all SVX hits matched	131359	45.8	26306	78.1
5	V0 inside target	121941	42.5	23680	70.3
6	V1 outside SVX	118861	41.4	23277	69.1
	Topology	Events	%	Events	%
4 track		279671	97.4	33629	99.8
	(4)	75377	26.3	1037	3.1
	(2,2)	153908	53.6	27389	81.3
	(3,1)	14582	5.1	539	1.6
	(2,1,1)	31342	10.9	4443	13.2
	(1,1,1,1)	4462	1.6	221	0.7
<4 track		6186	2.1500	63	0.187
	(1)	1	0.0003	0	-
	(2)	87	0.0303	0	-
	(3)	1688	0.5880	6	0.018
	(1,1)	64	0.0223	0	-
	(2,1)	3541	1.2300	51	0.151
	(1,1,1)	805	0.2800	6	0.018
>4 track		1235	0.4300	0	-
	(5)	26	0.0090	0	-
	(3,2)	52	0.0180	0	-
	(4,1)	258	0.1080	0	-
	(2,2,1)	456	0.1590	0	-
	(3,1,1)	141	0.0490	0	-
	(3,2,1)	1	0.0003	0	-
	(4,1,1)	1	0.0003	0	-
	(2,1,1,1)	229	0.8000	0	-
	(2,2,1,1)	2	0.0006	0	-
	(3,1,1,1)	1	0.0003	0	-
	(1,1,1,1,1)	68	0.0230	0	-

Table 4.2: The statistics for the vertex fitting.

have the highest probability of being mistaken for the desired channel, $K_S K^\pm \pi^\pm$, since the missing energy of the π^0 could be incorrectly assigned to one of the inner pions, giving it a higher probability to be identified as a kaon. However, as we shall see, this background does not appear significantly in the final data sample. Background events of the type

$$p\bar{p} \rightarrow K_S K_S$$

do not pass the kinematic fit because it is nearly impossible for a π^\pm to fake a K^\pm .

4.5.3 $K_S K^\pm X^\mp$

Assuming one of the tracks from V0 is K^\pm , then the other track (X^\mp) is π^\mp . The events with missing particles in addition to X^\mp should be suppressed by the kinematic fit.

Because there is virtually no background from the first two channels, the particle identification must only distinguish $K^\pm \pi^\mp$ from $K^\mp \pi^\pm$. In this case, only one particle must be positively identified; the other is identified by process of elimination. This greatly simplifies the particle identification process.

4.5.4 dE/dx Theory

As charged particles travel through matter and ionize the surrounding medium, they lose energy. In the limit of particles that are not ultra-relativistic, i.e. $2\gamma m_e \ll M$, where m_e is the mass of the electron and M is the mass of the charged particle doing the traveling, the equation for the rate of energy loss is given by the Bethe-Bloch equation ([36] Equation 23.1).

$$-\frac{dE}{dx} = Kz^2 \frac{Z}{A} \frac{1}{\beta^2} \left[\ln \frac{2m_e c^2 \beta^2 \gamma^2}{I} - \beta^2 - \frac{\delta}{2} \right]$$

The variables K (overall constant), Z (atomic number of medium), A (atomic mass of medium), I (mean excitation energy of medium) and δ (density effect correction) are a function of the medium. The variable z is the charge of the incident particle, which is ± 1 in the case of pions and kaons. We do not care about the actual value of these parameters, because we fit the dE/dx curves with a simpler function in (4.1). We measure the dE/dx in the JDC, so the medium is a Isobutane/CO2 gas mixture. The remaining variable is β , the velocity of the particle. The velocity of a particle is given by

$$\beta = \frac{p}{E} = \frac{p}{\sqrt{p^2 + m^2}}.$$

Because a pion and kaon differ in mass, for a particular momentum they will have different velocities, and thus different values of dE/dx . This fact allows identification of particles with the same momentum. Because the dependence on mass m becomes less significant at higher momentum (i.e. $\beta \rightarrow 1$ for both particles as $p \rightarrow \infty$), the identification is good for π/K momenta up to about 500 MeV/c. Beyond that, the identification is not unique.

The ionization energy is measured by integrating the collected charge on each JDC sense wire. The analog-to-digital converters (flash ADC's) on each wire measure the current versus time for each wire at each end, and this data is written to tape with the entire event. Offline, each signal is linearized, integrated and corrected for non-linearities in the electronics and scaled by a calibrated factor for that wire. This is the raw value for the dE/dx measurement.

At the same time, the Monte Carlo simulation simply applies the Bethe-Bloch equation to the particle and gas and calculates a value for dE/dx . Because neither the Monte Carlo nor the data is properly absolutely calibrated, there is no need to use most of the parameters given above. Instead, we can fit the data and Monte Carlo with a simplified 3-parameter equation, and make adjustments to each if necessary. The equation is thus

$$-\frac{dE}{dx} = \frac{M}{\beta^2} \left[\ln \frac{N\beta^2}{1-\beta^2} - \beta^2 - \delta/2 \right] \quad (4.1)$$

where $M = -2.8 \times 10^{-7}$ MeV/cm, $N = -0.668$ and $\delta = 20055$. Since the the dE/dx of the JDC was never properly calibrated in absolute terms, the units of M is arbitrary, although they are stated to be "MeV/cm" in the literature. The fit to the data and MC is shown in figure 4.8.

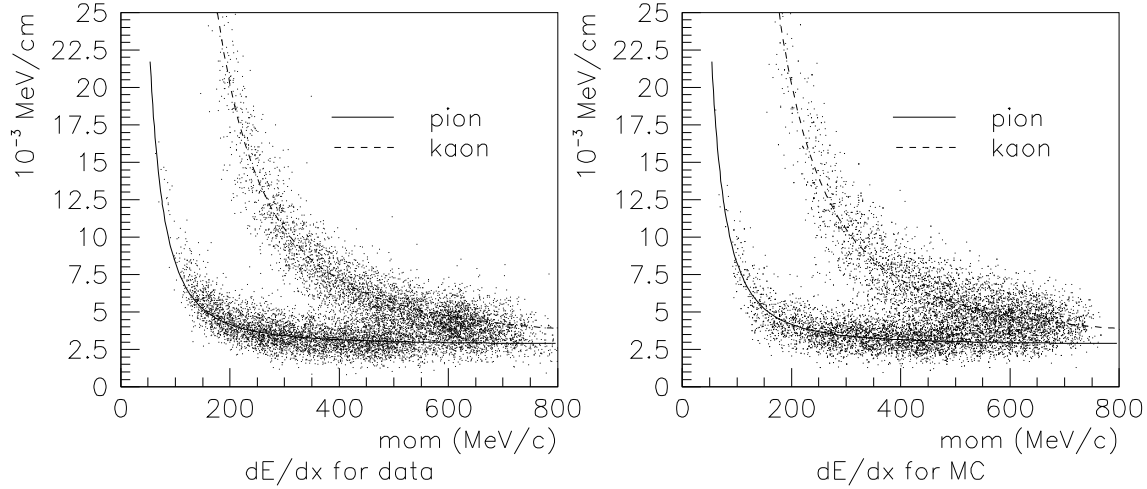


Figure 4.8: The dE/dx profiles for (corrected) data and (corrected) MC. The simplified Bethe-Bloch curves are described in the text.

4.5.5 Corrections applied to data

A comparison between the raw data dE/dx values and the values in the Monte Carlo calculated theoretically with the Bethe-Bloch equation showed a marked discrepancy. This appears to be due to the fact that there was an unsubtracted positive DC bias to all JDC signals in the real data. It appears that the calibration committee did a quick and dirty job calibrating the dE/dx values for the data using only minimum ionizing particles, thus only at one momentum. As can be seen in figure 4.9, the minimum ionizing point lies more or less on the unity line relating the data to the Monte Carlo. However, everything above that point is incorrect. For each slice of momentum, the mean data value for dE/dx was plotted versus the Monte Carlo value for dE/dx (see figure 4.9), and a line was fit giving the following

$$y = 0.00118 \text{ MeV/cm} + 0.564x.$$

This equation was then inverted and applied to the data, and the resulting curves for Monte Carlo and data became sufficiently similar (see figure 4.8).

4.5.6 Corrections applied to Monte Carlo

We found that the dE/dx values arrived at through CBGEANT did not have the same statistical variation that the data did. As was to be expected, the default Monte Carlo values were too “clean”. The default Gaussian smearing added to the dE/dx values was not enough. To correct for this, additional Gaussian smearing was added to the Monte Carlo values, using the following formula, where $\text{gauss}()$ generates a random value from a normal distribution with mean 0.0 and width 1.0,

$$\frac{dE}{dx} \text{ MC-smear} = (4.0 \times 10^{-4} \text{ MeV/cm}) \cdot \text{gauss}() + (0.15 \cdot \frac{dE}{dx} \text{ MC}) \cdot \text{gauss}().$$

The resultant width of the dE/dx distribution is about 20-30% of the mean value, depending on momentum. A comparison between data and Monte Carlo with the preceding smearing is given in figure 4.10. The overlap in the critical region above 450 MeV/c appears to be well described by the Monte Carlo.

4.5.7 Curves used for Particle Identification

As long as the data and Monte Carlo are virtually indistinguishable, one can make graphical cuts on the distributions. We choose to make two curves; one curve gives the upper limit of dE/dx for pions and the

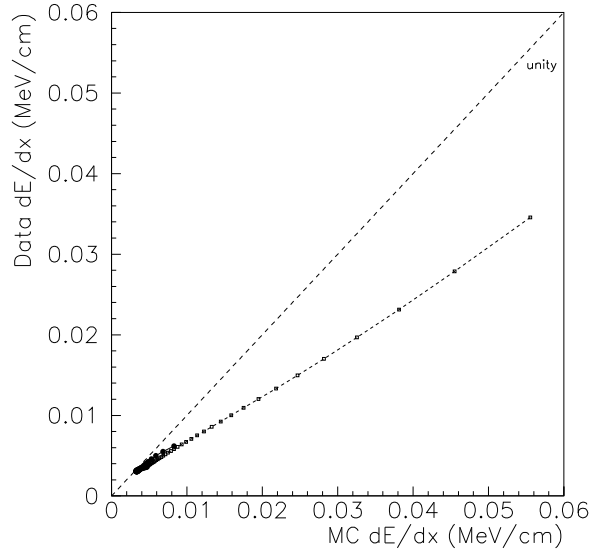


Figure 4.9: The calibration curve for data dE/dx values versus Monte Carlo (Bethe-Bloch) values. The diagonal line indicates what the proper relationship should be.

other gives the lower limit of dE/dx for kaons. Above 400 MeV/c, there can be an ambiguity as the two curves cross. Thus all tracks are classified into one of four disjoint regions:

1. “ π ” - must be a pion
2. “ K ” - must be a kaon
3. “ambig” - could be either (ambiguous)
4. “nil” - is neither.

See figure 4.11 to see the positions of the curves.

To generate these curves, we fit each arm with the simplified curve given above in subsection 4.5.4 and shown in figure 4.8. The curves are then shifted in momentum by 50 MeV/c (x axis) and shifted in dE/dx by 0.0015 MeV/cm (y axis). The pion curve is shifted up and right, while the kaon curve is shifted down and left (figure 4.11).

4.5.8 Particle Identification Logic

Events are rejected if both tracks are “ambiguous,” meaning that the dE/dx points lie in the ambiguous region: either track could be a pion or kaon. Events are also rejected if either track is “nil” meaning that it lies in the “nil” region. The remaining events have at least one track that is uniquely identified. Because of the arguments given at the beginning of this section, the other particle is also identified: it is a π if the first particle is a K and vice versa.

In the Monte Carlo events, a few events are misidentified. In the $K_S K^+ \pi^-$ MC events, 28 events out of 15K are misidentified as $K_S K^- \pi^+$, while in $K_S K^- \pi^+$ MC Events, 56 events out of 15K are misidentified as $K_S K^+ \pi^-$. This is a total of 84 events out of 30K, or only 0.3 % of data points in the Dalitz plot.

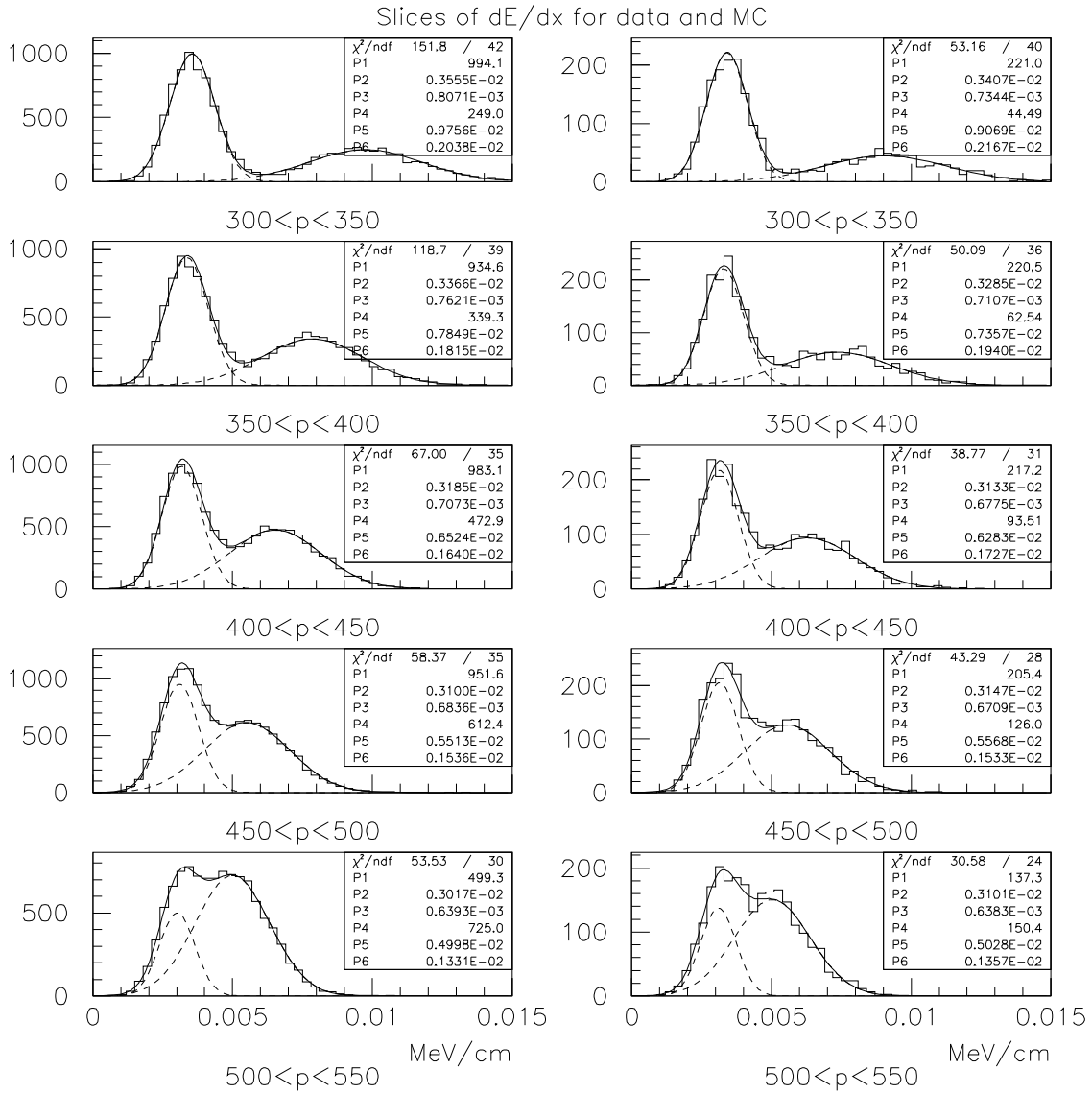


Figure 4.10: The dE/dx distributions in slices of momentum. Each plot shows a double peak, with the left peak due to pions and the right peak due to kaons. The left column is real data, right right column is MC. The agreement between data and MC after corrections and additional MC smearing is good.

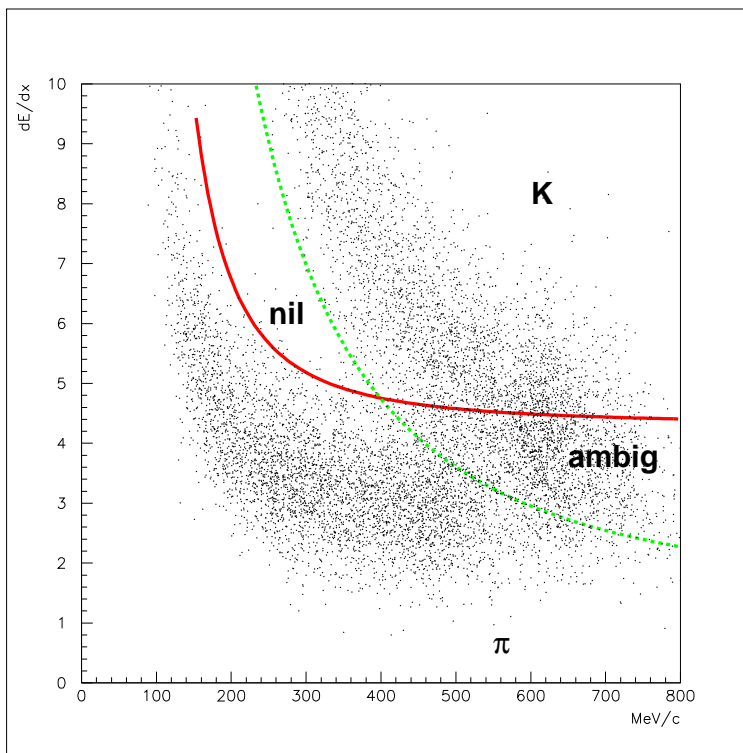


Figure 4.11: The graphical particle identification cuts. There are four labeled regions, “nil”, “K”, “ π ” and “ambig”.

4.6 Corrections

4.6.1 Run by run momentum scaling

The drift-velocity of ionized electrons in the JDC is inversely proportional to the pressure of the JDC gas. Because the Crystal Barrel JDC operates at atmospheric pressure which changes with the ambient weather conditions, the atmospheric pressure is measured concurrently with the data and corrections are applied offline. Also, the JDC gas mixture (isobutane/ CO_2) ratio affects the signal pulse height on the wires and to a lesser extent the measured drift-velocity.

During the April 1996 run period, one of the gas flow valves became stuck and the JDC gas mixture became too CO_2 rich. The regulator was fixed shortly thereafter, but it took a significant number of runs for the ratio to reach the desired 1:10 ratio. The impact on the data can be seen in 4.4 where the dE/dx measurement spikes up.

To correct for both of these effects, the measured momenta of each event was scaled by a factor for each run. A run typically lasts on the order of 30 minutes, over which time scale the weather and beam conditions are relatively stable. The scale factor was determined by averaging the invariant mass of the vertex V1 over each run and comparing to $m_K = 497.672 \text{ MeV}/c^2$. The run-by-run scale factors are plotted in figure 4.12. The sharp dip near run 35450 is due to the gas mixture problem; the valve stopped working near run 35430 and was fixed near run 35470. The broad dip around run 36000 was caused by weather conditions.

4.6.2 Error scaling

Just as the errors of the JDC hits used in the vertex fit needed some tuning, the error estimates of the reconstructed momenta needs some tuning in order that the probabilities returned by the kinematic fit make sense. For accurate measurements with Gaussian errors of the proper channel, the probability distribution (also known as the confidence level) is uniform from 0 to 1.0. The probability is the probability that subsequent events will have a better fit to the hypothesis.

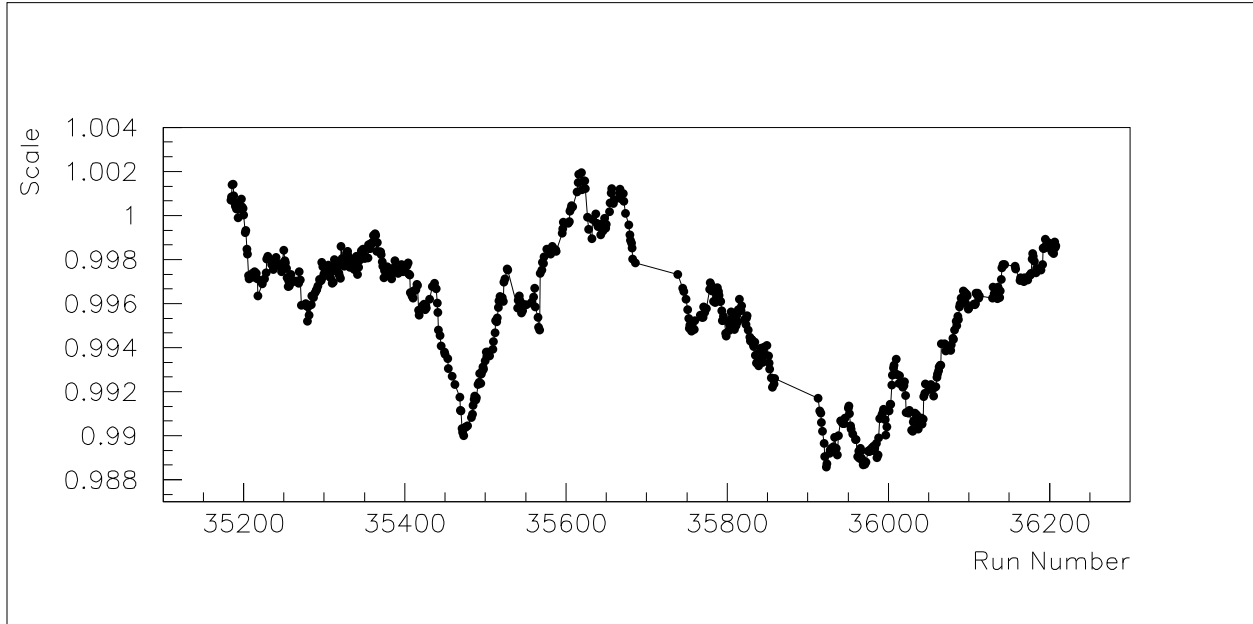


Figure 4.12: The momentum scale factor as a function of run number

	MC	Data
Momentum x, y Scaling	0.9985	1.0055
Momentum z Scaling	1.0035	1.0709
Momentum Error Scaling	1.25	1.55
π^\pm correction parameters for energy loss		
α_1	-1.3566	
α_2	-2.283×10^{-2}	
α_3	6.728×10^{-3}	
α_4	-9.316×10^{-6}	
K^\pm correction parameters for energy loss		
α_1	0.8719	
α_2	-1.966×10^{-2}	
α_3	1.533×10^{-2}	
α_4	-2.033×10^{-5}	

Table 4.3: The correction parameters for momentum scaling due to JDC geometrical distortion, energy loss and error scaling.

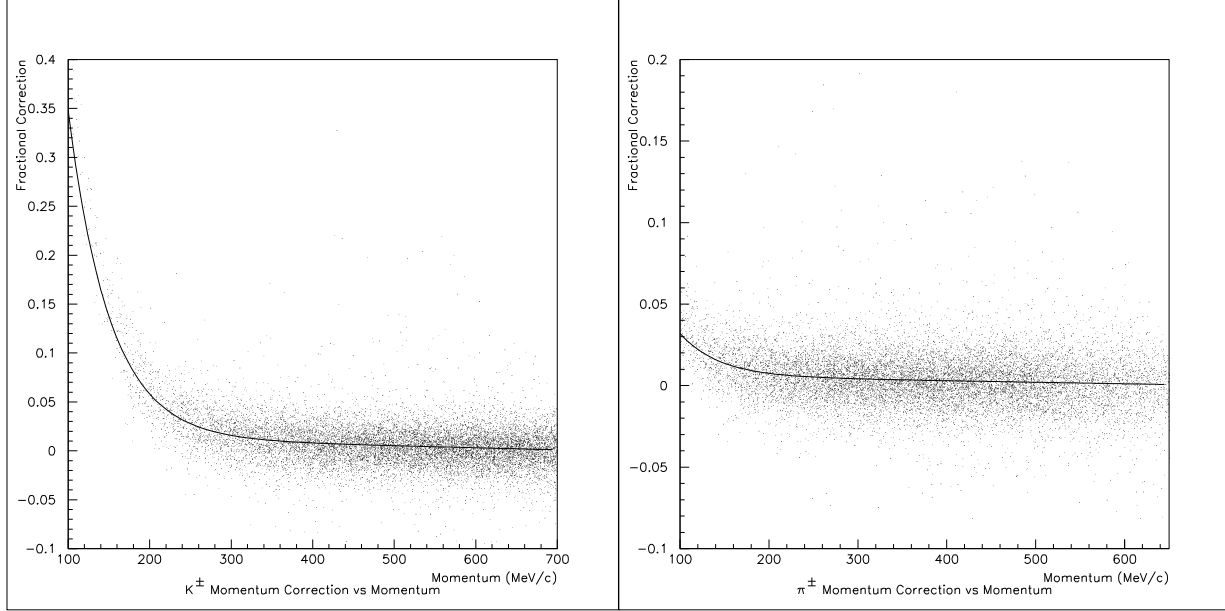


Figure 4.13: The fractional momentum correction vs momentum for K^\pm and π^\pm as derived from Monte Carlo.

4.6.3 Energy loss Correction

Charged particles experience an energy loss due to ionization in material before entering the JDC, especially at low momenta. This energy loss results in the measured momentum to be systematically too low. This effect increases at slower velocity, so low momentum kaons are affected the greatest. Figure 4.13 shows the correction fractions as a function of momentum for K^\pm and π^\pm .

The following phenomenological correction function was applied to all tracks, based on their particle identity:

$$f_{\text{ms}} = 1 + e^{\alpha_1 + \alpha_2 * p} + \alpha_3 + \alpha_4 p$$

where p is the particle's measured momentum and α_i are the parameters given in table 4.3. The functions are plotted in figure 4.13.

4.6.4 JDC geometrical distortion

The z -dimension of the JDC was discovered to be incorrectly calculated in the reconstruction by a significant amount. This was discovered independently by two groups. We found that the invariant mass of the V1 $\pi^+\pi^-$ pair was dependent on the orientation of the decay. If one takes the normal to the K_S decay plane

$$\hat{n} = \vec{p}_{\pi^+} \times \vec{p}_{\pi^-} \quad (4.2)$$

and then looks at the invariant mass of the pair as a function of

$$\cos \theta = \hat{n}_z / |\hat{n}|, \quad (4.3)$$

one could see a significant drop in mass as $\cos \theta \rightarrow 1$. This is because for $\cos \theta = 0$, the z dimension has no effect on the opening angle calculation, but as $\cos \theta \rightarrow 1$ the z dimension becomes important. If the z dimension is compressed, the angle becomes smaller too, and the invariant mass falls. This is shown in figure 4.16.

To determine the correct JDC z dimension, the z dimension was scaled by a parameter until the invariant mass was no longer dependent on the polar angle of \hat{n} . The scaling factor of 1.0709 ± 0.005 was determined to satisfy this condition.

A second group in the collaboration discovered that the track-to-PED alignment was significantly off, with the JDC z dimension about 6% too small. This agrees well with the determination made using the $m(K_S)$ vs \hat{n} method. Figure 4.16 shows that the V1 mass is now constant with respect to decay plane angle.

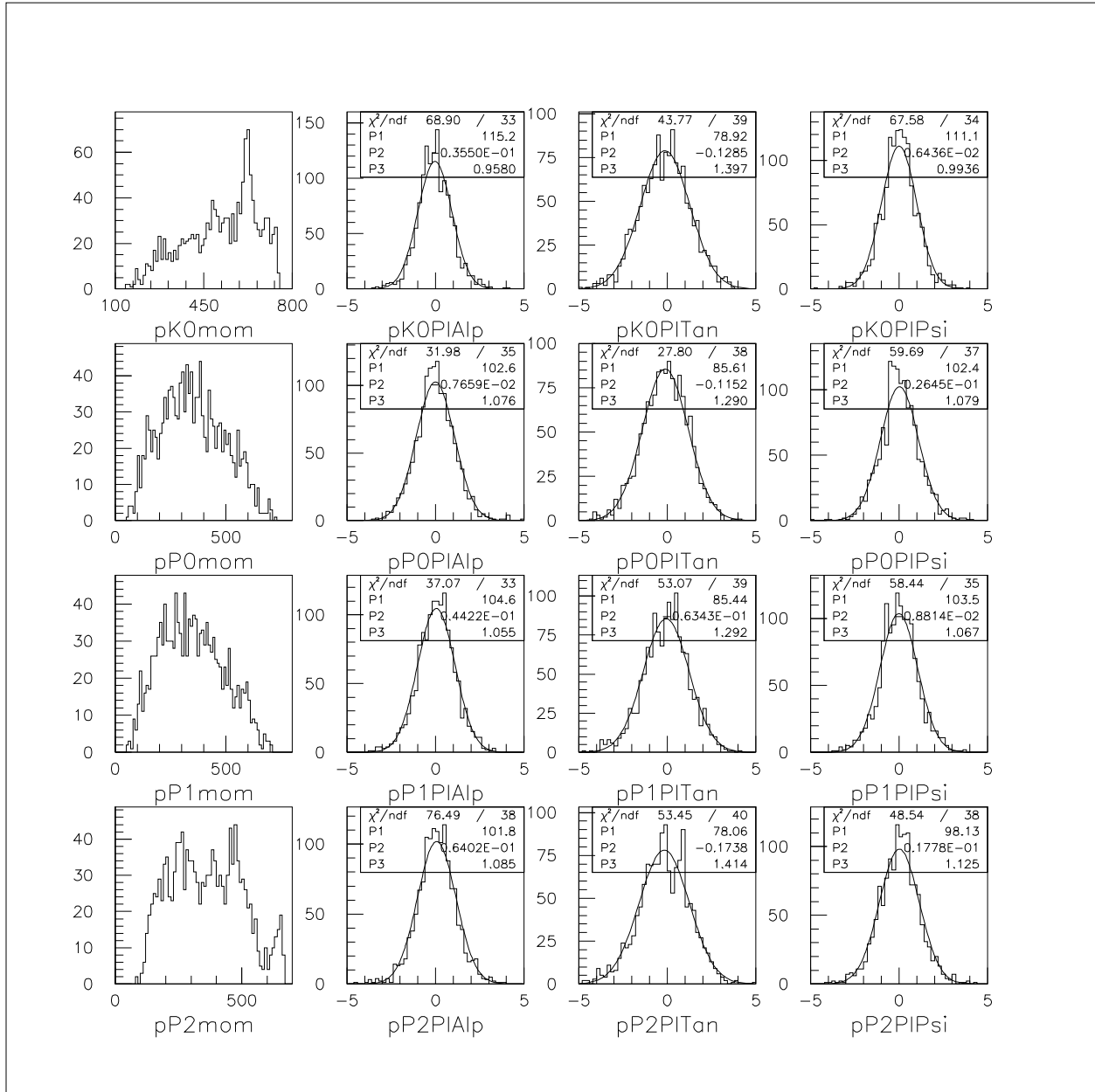


Figure 4.14: The statistical pulls of each particle's momentum component as seen in the real data. Each row represents one particle, in the following order: (from V0) K^\pm and π^\pm , (from V1) π^+ and π^- . The first column is the particle's total momentum, the second column is the pull in α (curvature), the third column is the pull in $\tan \lambda$ (pitch), the fourth column is the pull in ψ (azimuth).

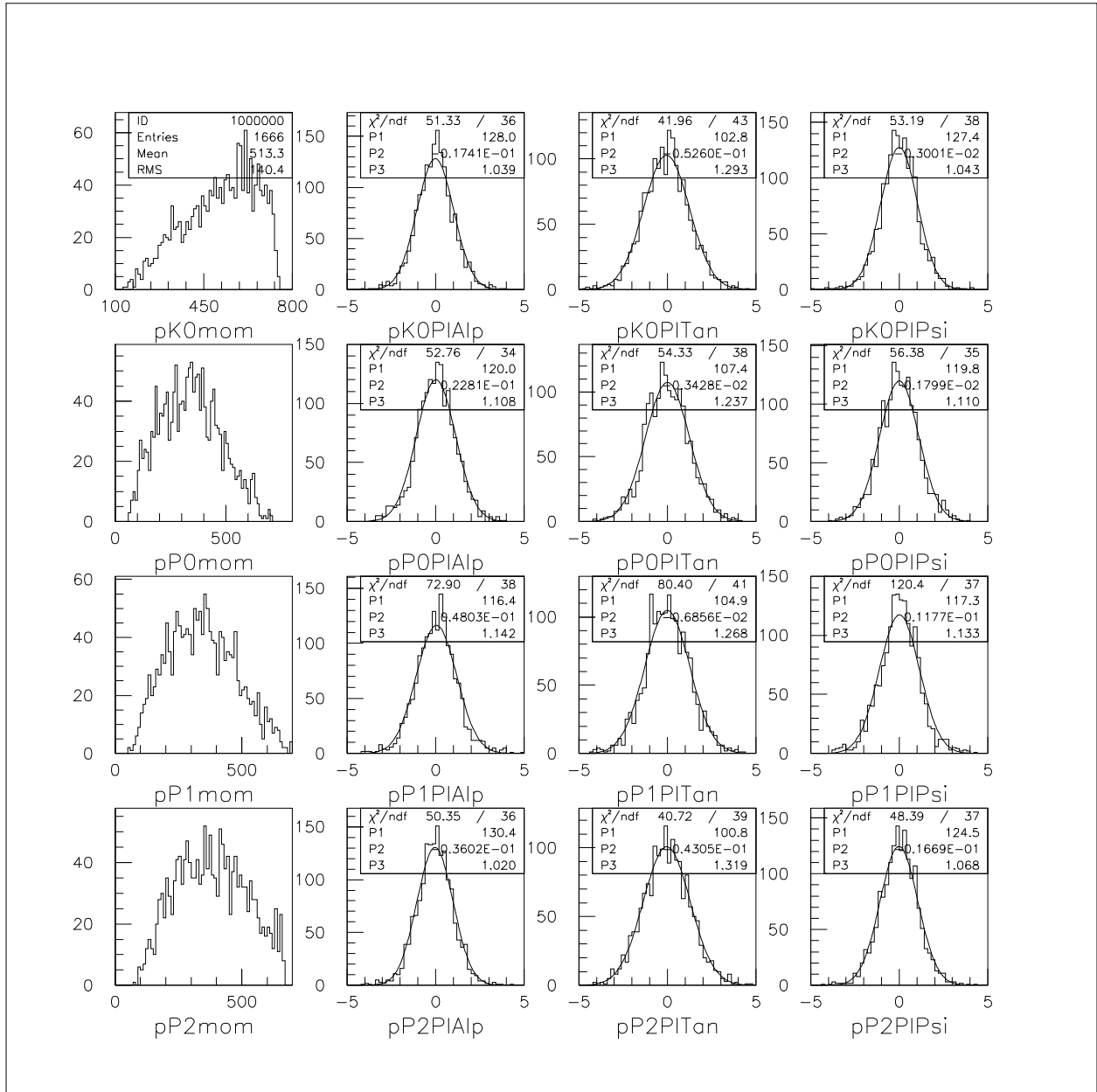


Figure 4.15: The statistical pulls of each particle's momentum component as seen in the Monte Carlo. See figure 4.14 for a description of the plots.

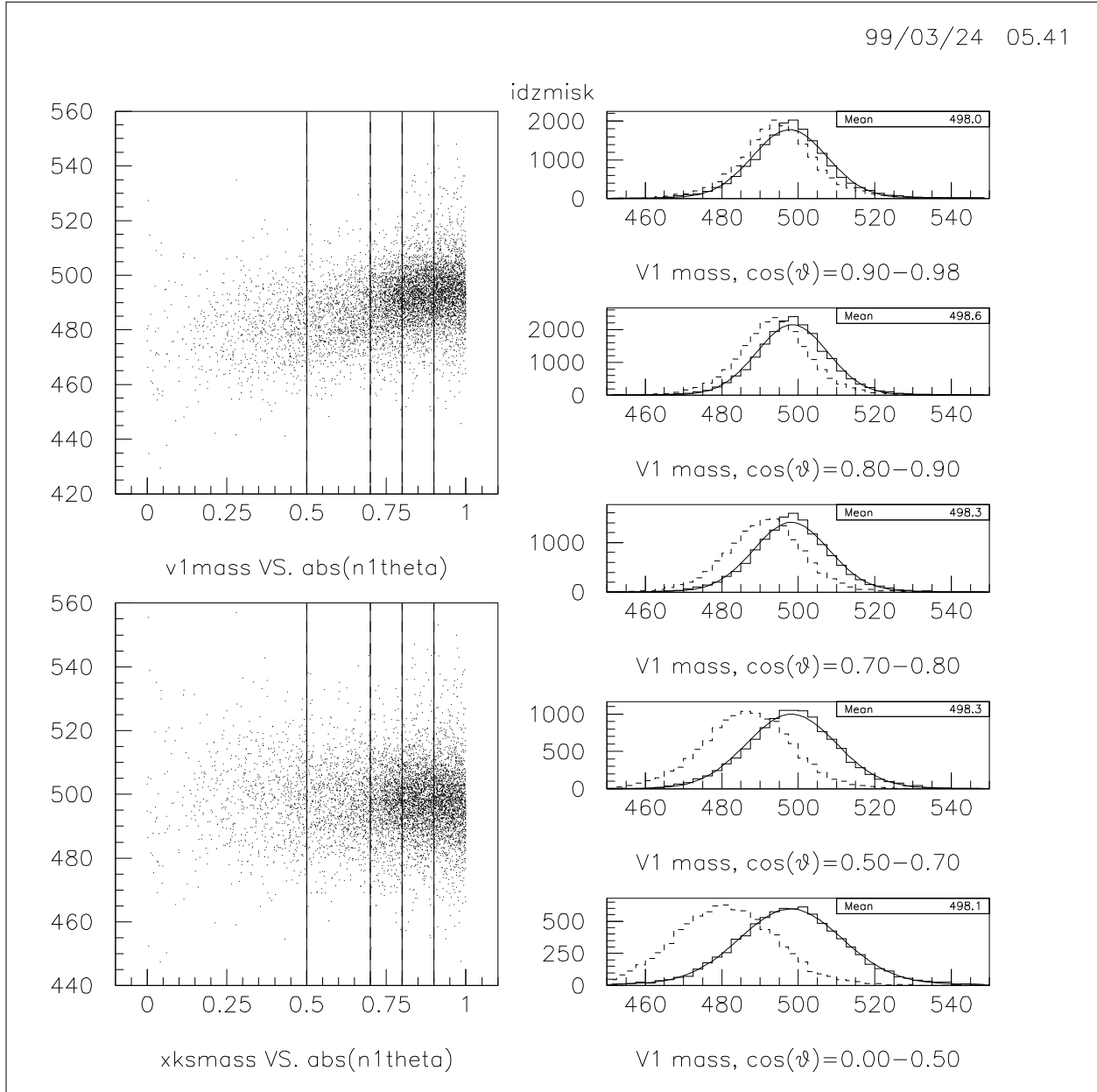


Figure 4.16: V1 invariant mass, before and after z -dimension rescaling. In (a) is shown the invariant mass of V1 versus the decay plane angle (see equation 4.3). In (b) the same is plotted, except after the rescaling of the z dimension. The right column shows the slices of the scatter plots. The solid line is the corrected data, and the dashed line is the uncorrected data.

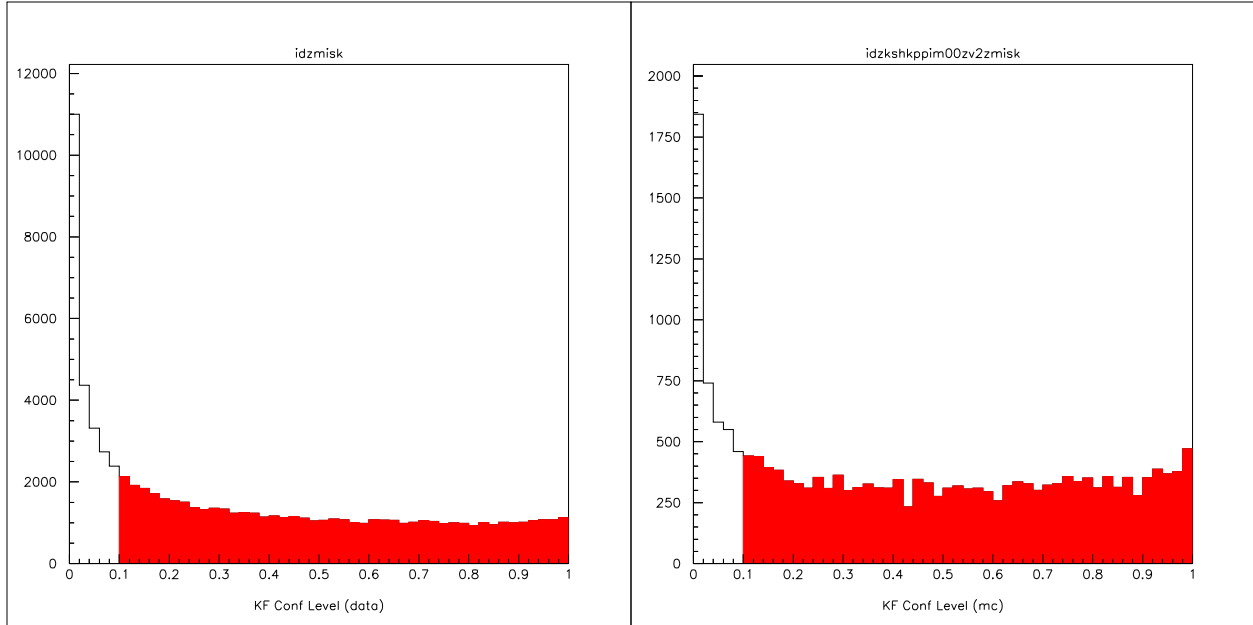


Figure 4.17: The Confidence Level or Probability of the 5C kinematic fit. The shaded region are the accepted events at 10% confidence. (a) real data (b) Monte Carlo

4.7 Kinematic Fit

4.7.1 Introduction

The measurement accuracy and precision can be improved if there are additional constraints imposed on the data beyond the direct measurements of the apparatus. For example, if the total momentum of the event is known to be zero even though the measured values do not sum to zero, the measured values can be slightly adjusted (within the estimated errors or error matrix) by a minimization procedure until they do sum to zero. This typically improves the accuracy of the measurements and always improves the precision. For “good” events, the kinematic fit will return a probability that lies uniformly between 0.0 and 1.0.

At the same time, a kinematic fit can perform two other useful tasks. First, it can help distinguish between charged kaons and pions, because the total energy is a function of the mass of the constituent particles. The correct assignment will have a higher probability. Second, it can reject events that have “missing” particles (such as a K_L or other neutral particle) or are otherwise bad, because these events will have a low probability, typically less than 1%. The algorithm of kinematic fitting is given in chapter 10.

The channel of interest in this analysis has five additional constraints that may be imposed on the measured momenta.

1. Total momentum is 0 (three constraints).
2. Total energy is twice the proton mass (one constraint).
3. Invariant mass of V1 vertex is K_S mass.

At this point in the analysis, all particles have been identified already, so the kinematic fit is used to reject bad events as well as improve the accuracy of the good events.

The kinematic fit depends directly on the estimated errors of the measured momenta. The errors are determined by the vertex fit based on the fit itself plus corrections for multiple-scattering. The errors are diagonal in the vertex-fit basis (α (curvature), $\tan \lambda$ (pitch), and ϕ (azimuth)) but in the Cartesian (p_x, p_y, p_z) basis, the errors are described by a symmetric 3×3 matrix. These errors need to be adjusted slightly in order that the final probability calculated by the kinematic fit makes sense. This procedure is described below.

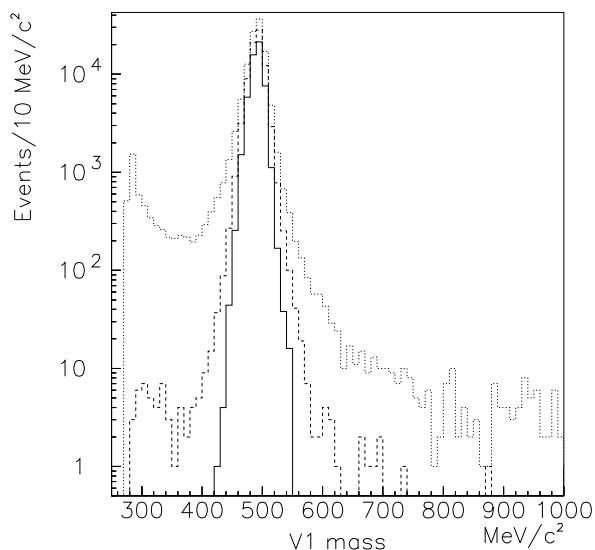


Figure 4.18: The V1 invariant mass distribution, before the kinematic fit (dotted), after 4C phase space fit (dashed) and after full 5C kinematic fit (solid).

The events are first subjected to a phase space 4-constraint kinematic fit, meaning that the K_S mass constraint is not imposed, i.e.

$$p\bar{p} \rightarrow K^\pm \pi^\mp \pi^+ \pi^-.$$

If the fit converges with a reduced $\chi^2/4 < 20.0$ (a very loose constraint), then the events are submitted to the 5-constraint kinematic fit which includes the constraint that the pions from the outer vertex have the K_S mass,

$$p\bar{p} \rightarrow \begin{array}{c} K^\pm \pi^\mp K_S \\ \quad \quad \quad \swarrow \\ \quad \quad \quad \pi^+ \pi^- \end{array}.$$

The confidence level for this hypothesis is required to be greater than 0.10, as seen in figure 4.17.

The cleanliness of the signal after the kinematic fit can be seen in figure 4.18. The background level from non- K_S events is negligible.

4.7.2 Reconstruction Accuracy

The invariant mass of the V1 $\pi^+\pi^-$ pair and total energy of the event, after all the corrections, is histogrammed in figure 4.19.

The momenta of physical interest are the momenta at “ $t = 0$ ”, i.e. the momenta at the interaction point(s) rather than the momenta as tracked in the JDC. Ideally, the momenta measured in the JDC can be corrected for multiple-scattering and then kinematically fitted to obtain the physical $t = 0$ values.

A check of this reconstruction accuracy can be done by comparing the $t = 0$ values generated by the Monte Carlo (the “physical” values) with the reconstructed values. To make a meaningful plot of the comparison, the Dalitz plot coordinates $\vec{X} = (x, y)$ for each event are calculated twice, once using the MC generated values \vec{X}^{mc} and once using the kinematically fitted reconstructed values \vec{X}^{kf} . Ideally, these two values are the same but in practice each event is slightly off. All the events are binned according to the \vec{X}^{mc} value, with a 2-dimensional vector weighting equal to

$$\vec{\Delta}_i = \vec{X}_i^{\text{kf}} - \vec{X}_i^{\text{mc}}$$

where i runs over the entries for a particular bin. Once all events are binned, a mean deviation and RMS

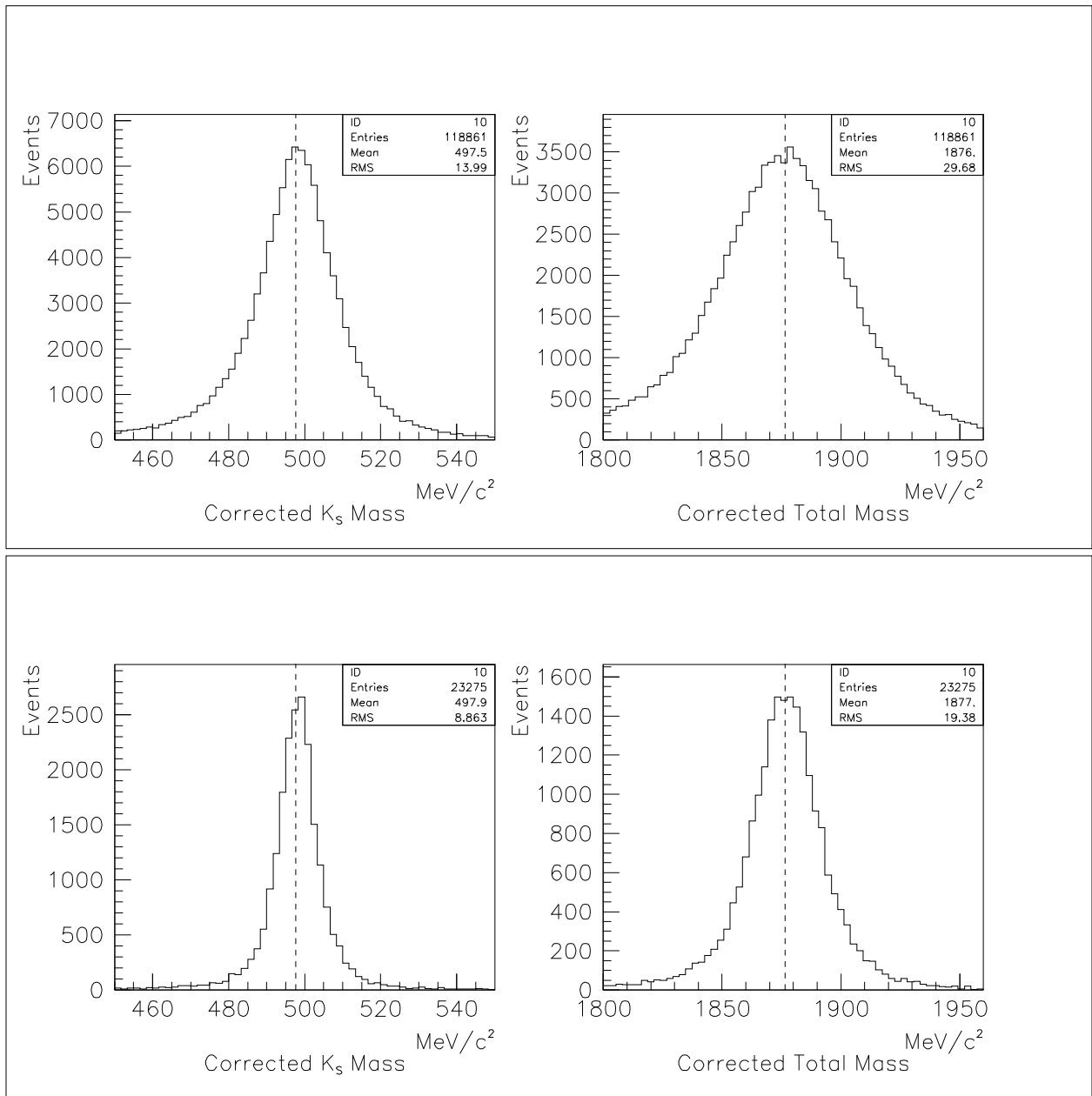


Figure 4.19: The V1 $\pi^+\pi^-$ invariant mass and total energy for data and Monte Carlo

deviation are calculated,

$$\vec{\bar{\Delta}} = \frac{1}{N} \sum_i \vec{\Delta}_i$$

$$\bar{\Delta}_{\text{rms}} = \sqrt{\frac{1}{N-1} \sum_i \left(\Delta_{i,x}^2 - \bar{\Delta}_x^2 \right)}$$

where

$$\Delta^2 = (\Delta_x^2, \Delta_y^2).$$

Figure 4.20 shows the results of these calculations. As can be seen, the mean shifts are randomly oriented, with large deviations only coming from edge bins with low MC statistics. The shifts are all much smaller than the bin size. Likewise, the RMS spread of the shifts (figure c) are also smaller than the bin size, approximately half the bin size, showing that this bin size is a good choice. Figure (d) shows the fractional reconstruction error for all events in the Dalitz plot variables

$$f_x = \frac{\Delta x}{\bar{x}} = 2 \frac{x^{\text{kf}} - x^{\text{mc}}}{x^{\text{kf}} + x^{\text{mc}}}$$

$$f_y = \frac{\Delta y}{\bar{y}} = 2 \frac{y^{\text{kf}} - y^{\text{mc}}}{y^{\text{kf}} + y^{\text{mc}}}.$$

There is a small systematic shift of about -0.06 % and the RMS error is about 0.8 %, both of which are excellent for this analysis and independent of axis.

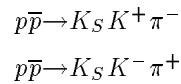
4.7.3 π^0 Suppression

This analysis has only looked at charged data so far. This is because the electro-magnetic calorimeter is plagued by hadronic split-offs from the charged particles. Many of the ‘‘PEDs’’ turn out to be not be from physical photons, but caused by dislodged neutrons and other uninteresting hadronic debris (caused by the collision of the desired pions and kaons hitting the crystals) flying from one half of the detector to the other side. These PEDs are not part of the interesting physics and just cause additional random background to the photon signal. Luckily, in this analysis we are not looking for photons, so this background doesn’t matter.

However, the PEDs can still be used to check to see if events with a $\pi^0 \rightarrow \gamma\gamma$ (for example $p\bar{p} \rightarrow K_S K^\pm \pi^\mp \pi^0$) are surviving the preceding cuts and kinematic fit. Happily, the answer is no, as seen in figure 4.21. The invariant mass of all pairs of PEDs before the kinematic fit cuts is plotted first. While most PEDs are junk and therefore form just a smooth combinatorial background that decreases with energy, a significant π^0 peak can be seen above the background. This peak totally vanishes for events that pass the kinematic fit, shown as the second dashed histogram. No $\eta \rightarrow \gamma\gamma$ peak was seen before or after the kinematic fit.

4.8 Charge symmetry

The two reactions



should have identical Dalitz plots if the strong force is charge independent. The experimental Dalitz plot may have some charge dependence, however, for two reasons.

First, the JDC is inherently chiral. The external magnetic field causes the drift lines to rotate about each sense wire by 7.2° [8], the Lorentz angle. Tracks which curve in opposite directions will not see the mirror symmetric fields, and this could cause a small asymmetry between measured tracks of opposite sign.

Second, hadronic interactions with the detector are charge dependent. For example, the biggest asymmetry is between K^+ and K^- which interact differently with protons. For kaons between 0.1 and 1.0 GeV/c, the $K^- p$ cross section is roughly 5 to 10 times that of $K^+ p$ [36]. This increased interaction probability can cause more interactions in the JDC and the Barrel, raising the probability that splash-back particles can re-enter the JDC and cause an event to be rejected.

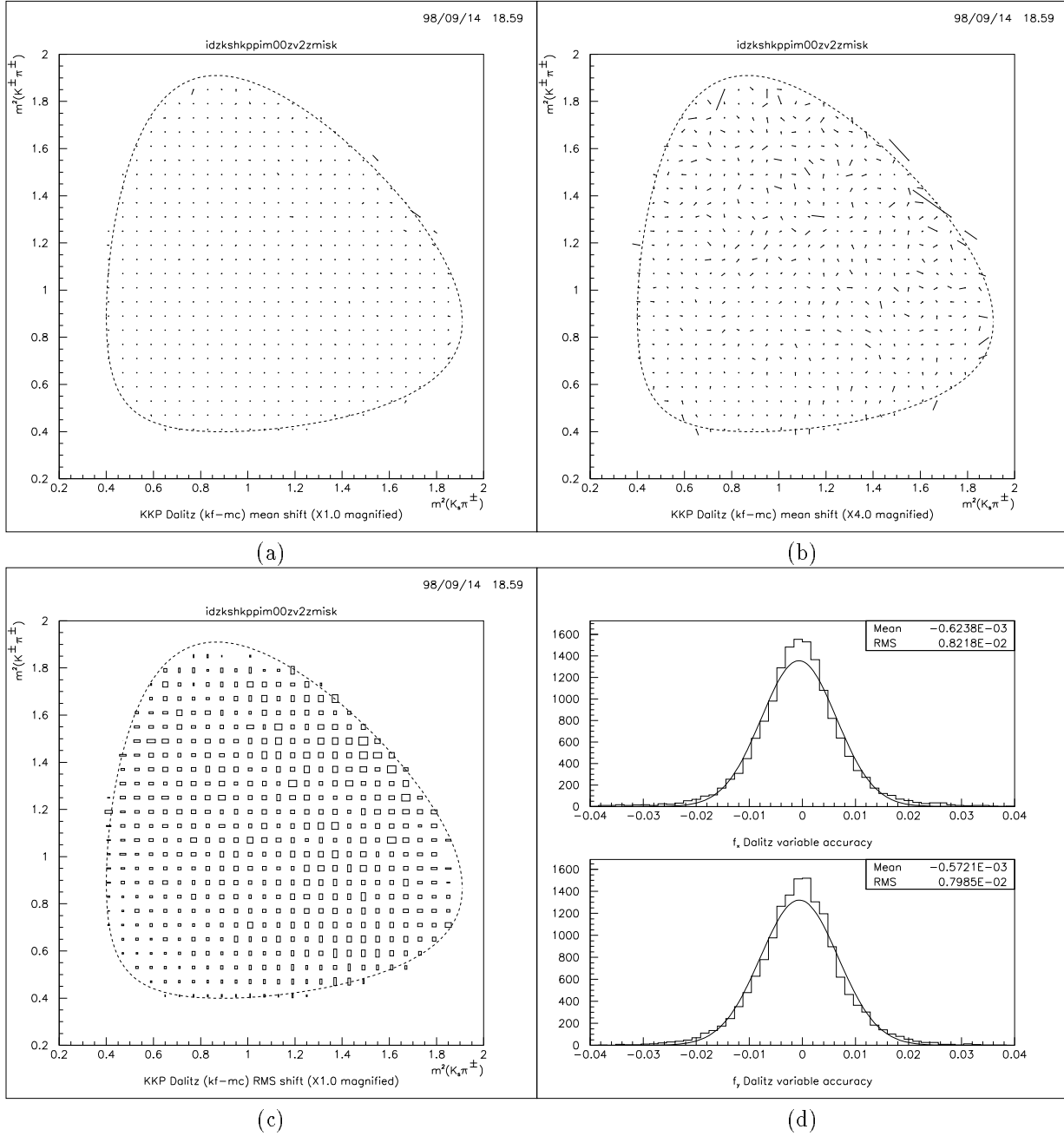


Figure 4.20: A comparison between the reconstructed and MC generated Dalitz plot variables. Figures (a) and (b) show the average mean deviation for each bin. The short line segment in each bin has one vertex at the center of the bin; the other vertex is the mean of the deviation, $\bar{\Delta}$, as described in the text. Figure (a) shows the unscaled deviation vector, while figure (b) shows the deviation vector scaled by a factor of 4 to make the deviations easier to see. Figure (c) shows the RMS deviation, with each box dimension ($l \times w$) equal to twice the RMS deviation in that direction. (d) Shows the accuracy of all events, f_x and f_y (see text).

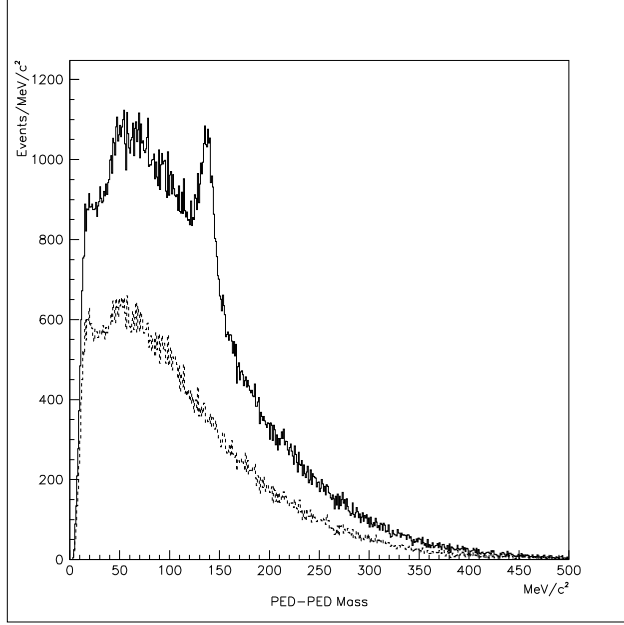


Figure 4.21: The PED-PED invariant mass for events before (solid line) and after (dashed line) the kinematic fit cut.

The ratio of charge configurations accepted in the final Dalitz plot are

$$\frac{N(K_S K^+ \pi^-)}{N(K_S K^- \pi^+)} = \frac{26994}{26736} = 1.0097 \pm 0.0086$$

which is very nearly consistent with unity. The projections of the Dalitz plot for each charge configuration is given in figure 4.22. There is a slight enhancement of $K_S K^+ \pi^-$ events below $1 \text{ GeV}^2/c^4$ but it is probably not significant in the fit. The χ^2 comparison between the two Dalitz plots (shown in figure 4.23)

$$\chi^2 = \sum_{i \text{ bins}} \frac{[N_i(K_S K^+ \pi^-) - N_i(K_S K^- \pi^+)]^2}{N_i(K_S K^+ \pi^-) + N_i(K_S K^- \pi^+)}$$

gives $\chi^2/N_{df} = 457/505 = 0.91$, showing good compatibility.

For the Monte Carlo, 1 million events of each charge configuration were generated. The ratio of accepted events was

$$\frac{N(K_S K^+ \pi^-)}{N(K_S K^- \pi^+)} = \frac{15087}{14964} = 1.0082 \pm 0.012$$

which is also in agreement with unity and even better agreement with the observed ratio. Thus the small ($< 1\%$) charge asymmetry in the data is due to the detector and reconstruction and not interesting physics. Since the effect is only 1σ from unity and the asymmetry is consistent with the Monte Carlo, it will not be considered further.

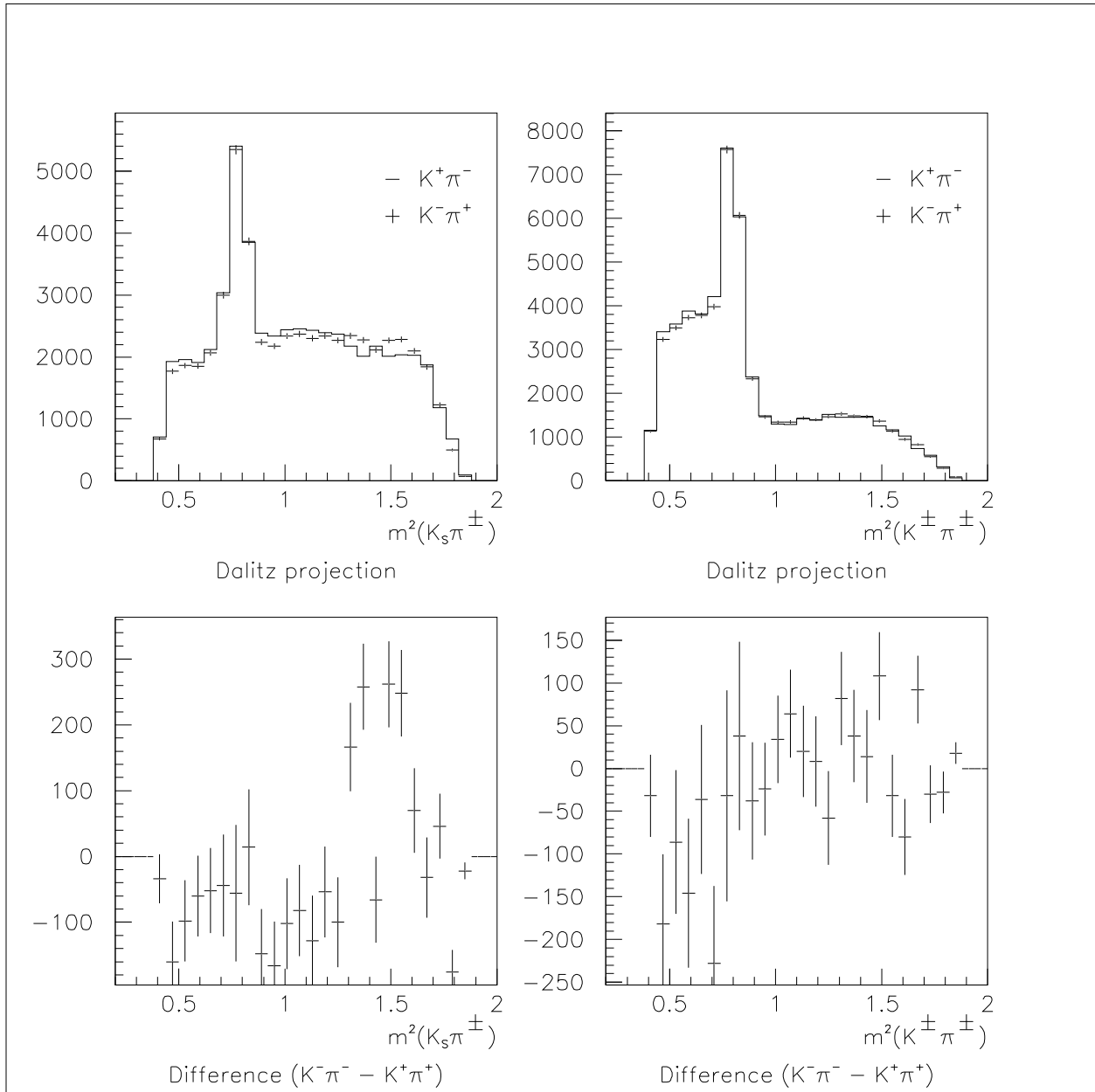


Figure 4.22: The Dalitz plot projections for each charge configuration, $K_S K^+ \pi^-$ and $K_S K^- \pi^+$ at top, and the differences between the two configurations at bottom. Note that only the error bars for $K_S K^- \pi^+$ are shown in the top projections; the error bars for $K_S K^+ \pi^-$ are of approximately equal size. The error bars in the difference plots take into account both individual errors.

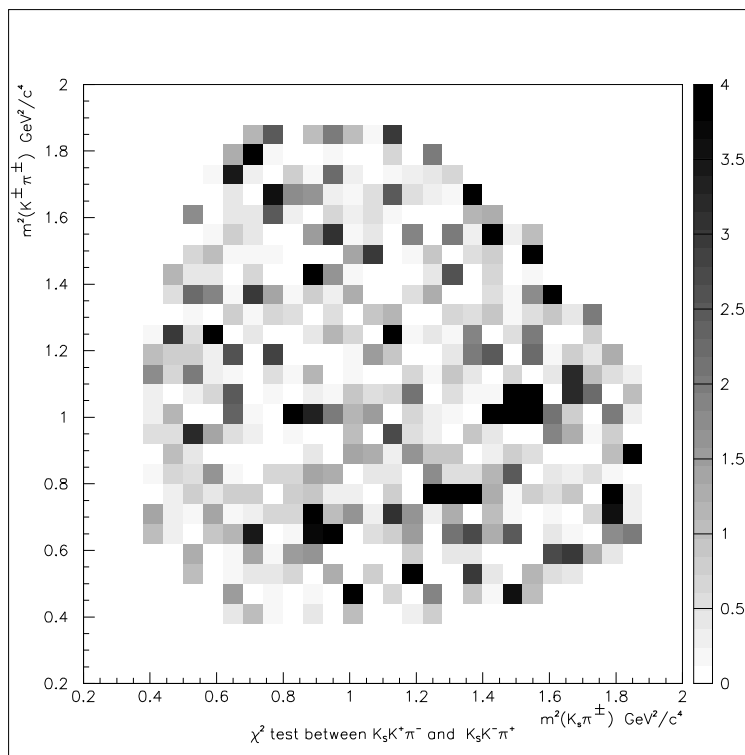


Figure 4.23: The χ^2 test between $K_S K^+ \pi^-$ and $K_S K^- \pi^+$. The maximum is set to $\chi^2=4.0$

Chapter 5

Monte Carlo Simulation

A good simulation of the experiment is necessary for several reasons.

1. Determination of corrections to the measured momenta, caused by losses in the detector.
2. Determination of overall efficiency for branching ratio calculations.
3. Determination of momentum dependent acceptance corrections to be applied to the Dalitz plot
4. Estimation of backgrounds

The first point has been discussed already in the data selection chapter 4. The second point is discussed in the branching ratio chapter 6. The final two points are discussed in this chapter, along with a discussion on the SVX positioning.

The Monte Carlo program, `CBGEANT`[6], is based on the general detector simulation program `GEANT`[26] from CERN. The program fully simulates the passage of the initially generated particles and any decay particles through all matter of the detector volume, except for the ionization of the gas in the JDC. The full JDC simulation, with tracking of delta rays, is too computationally expensive. The “fast” simulation method simply generates a statistical “time” signal for each wire that the track passes. However, the electromagnetic and hadron interactions with the crystals is fully simulated, using the `FLUKA` hadronic interaction package.

5.1 Channels simulated

The signal channel $K_S K^\pm \pi^\pm$ requires the most Monte Carlo statistics in order to get a smooth acceptance correction function. We generated 1,000,000 events of $K_S K^+ \pi^-$ and 1,000,000 events of $K_S K^- \pi^+$. However, since the acceptance of the trigger and data selection is smaller (about 1.5%), only about 30K events survive in the final Monte Carlo data set. This is sufficient for constraining the acceptance function, which is discussed in section 5.4.

For the purpose of background estimation, we also generated 100,000 events of the type $\pi^+ \pi^+ \pi^- \pi^- \pi^0$, and 100,000 events of the type $K_S K^+ \pi^- \pi^0$, 10,000 events of the type $K_S K_L \pi^+ \pi^-$, 100,000 events of the type $K_S \pi^+ \pi^-$, and 100,000 events of the type $K_S \pi^+ \pi^- \pi^0$. The later two do not conserve strangeness unless the $\pi^+ \pi^-$ pair originates from K_S , thus they are supersets of the $K_S K_S$ and $K_S K_S \pi^0$ channels.

The “ K_S ” was the standard `GEANT` K_S , which decays into both neutral pions ($K_S \rightarrow \pi^0 \pi^0$) and charged pions ($K_S \rightarrow \pi^+ \pi^-$), and there was no radial cut on the annihilation vertex. This explains why the efficiency for all channels was so low, since 1/3 is lost to the neutral decay, and another half or so is lost to decays inside the SVX. We used the standard K_S because these Monte Carlo data sets were used in other analyses too.

5.2 Parameters of the Monte Carlo

The Monte Carlo software is `CBGEANT` which is the Crystal Barrel customization of the CERN library `GEANT` 3.21. It includes all detector and structural components of the experiment. Most of the precise positioning

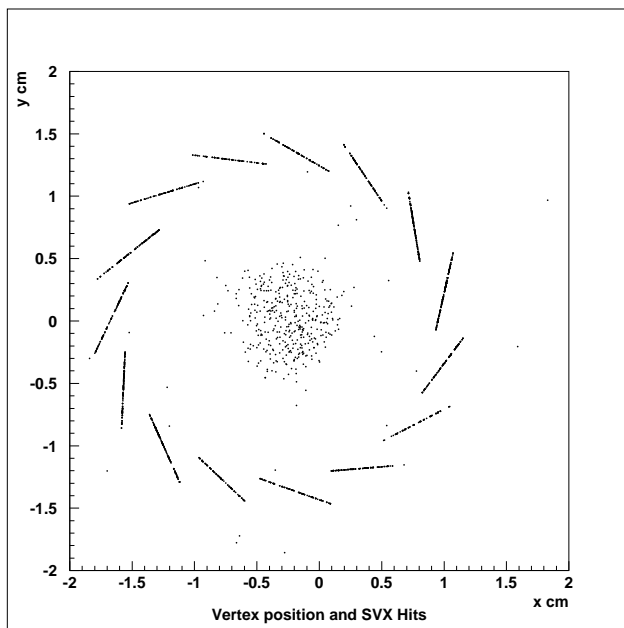


Figure 5.1: The positions of reconstructed vertices and SVX hits, showing the centering of the annihilation vertex distribution inside the SVX.

of large components is not absolutely critical to having a reasonable Monte Carlo. The critical positioning parameters are the JDC sense wire positions relative to each other and the positioning of the SVX detector relative to the annihilation spot. Because there are gaps in the SVX detector, annihilations that are far from the center of the SVX can produce tracks that leak through without being detected. Because of the handedness of the SVX detector planes, this can also create a charge asymmetry; positively charged particles are more likely to pass through this gap than negatively charged particles.

The position of the SVX can be measured directly only to within a few millimeters. A more accurate position can be determined by an iterative calibration using charged tracks, which minimizes the χ^2 of the helix fits to the SVX hits by adjusting the parameters of the SVX geometry. The position and pitch of each of the 15 segments was determined in this manner. These positions were then used to define the correct geometry in the Monte Carlo. The mean shift of the SVX relative to the external JDC was determined to be about 2.5 mm to the left.

The annihilation vertex ideally lies exactly at the center of the SVX detector. However, because of the complications of beam steering and non-ideal beam shape, the distribution of annihilation vertices can be slightly skewed or shifted. Using 4-prong triggered data, we have determined the mean position of the annihilation vertex to be $(-0.24, 0.02, 0.00) \pm 0.01$ cm and the Gaussian 1-sigma widths to be $(0.20, 0.22, 0.40) \pm 0.01$ cm. See figure 5.1 The Gaussian width is due to both physical and reconstruction uncertainties. In the $x - y$ plane, the Gaussian width is due mostly to the beam profile, while in the z plane the width is due entirely to the limited precision of z -reconstruction. (The JDC produces hits with $x - y$ errors on the order of 200 microns and z errors on the order of 1 cm.)

We generated the Monte Carlo annihilation vertex distribution with the parameters given above, except that the z width was set to 0.20 cm. The reconstruction of this simulated data produced measured means and widths consistent with the 4-prong real data.

Note that the center of the SVX was at $(-0.319, -0.012)$ cm which is slightly off from the center of the annihilation point.

5.2.1 Vertex position

The vertex (inner and outer) is reconstructed within typically 300 microns of the generated vertex. However, there are long tails that extend to 1 cm or more. On inspection with the event display, these are due to bad pattern recognition on the tracks, where the track finding algorithm missed several hits which would have

MC set	Efficiency	BR [10^{-3}]	Relative Intensity
$K_S K^\pm \pi^\pm$ (signal)	1.5×10^{-2}	2.820	100.00 %
$K_S K^\pm \pi^\pm$ ($K\pi$ swap)	2.8×10^{-5}	2.820	0.19 %
$K_S K_S [\pi^0]$	6×10^{-5}	0.760	0.11 %
$K_S [K_L] \pi \pi$	$< 3 \times 10^{-6}$	2.600	< 0.02 %
$K\pi K_S [\pi^0]$	3×10^{-5}	5.500	0.02 %
$4\pi [\pi^0]$	$< 3 \times 10^{-8}$	178.500	< 0.01 %
$K_S K_S [\eta]$	$< 3 \times 10^{-6}$	0.410	< 0.003 %
$K_S K_S$	6×10^{-5}	0.005	0.0007 %
Total Background	–	–	0.32 to 0.44 %

Table 5.1: The estimates of primary background. The relative intensity is the product of the efficiency times the branching ratio, renormalized to the signal channel. The particles in [brackets] are lost particles.

dramatically moved the track. The common problem was that these tracks either crossed several boundaries or the track ran along a sense plane or field plane.

5.3 Background Estimation

The analysis channel is surprisingly low in backgrounds. The displaced vertex and mass of the $K_S \rightarrow \pi^+ \pi^-$ decay is virtually background free. The biggest source of background comes from the signal channel itself, when the particles are misidentified. The remaining background comes from soft particles lost in the kinematic fit. The estimated total from all backgrounds is estimated to be no more than 0.44%. The total statistics is about 57K events, so there are about 250 background events over the entire Dalitz plot. With about 500 bins, that makes about 0.5 event per bin on average of background, while the Poisson noise of a typical bin will be $\sim \sqrt{57000/500} \sim 10$. Because the background is much smaller than the noise, no background subtraction is necessary.

Below we discuss the possible forms of background. In each case, we generate a number of Monte Carlo events of the specific background type and feed it into the same analysis chain, and count the number of events that survive all the cuts until the final Dalitz plot. This gives us the efficiency for that channel. We multiply this efficiency by the known branching ratios¹. The results are in table 5.1.

5.3.1 $K_S K^\pm \pi^\mp$ ($K\pi$ swapped)

This of course is the signal channel. Since the K_S is well tagged, the most likely background from the signal channel itself is reverse identification of the K^\pm and π^\mp at V0. Using Monte Carlo data, we find that only 28 ± 5 events are misidentified, which translates to 0.19 % of the Dalitz plot.

5.3.2 $K_S K_S [\pi^0]$

The $K_S K_S [\pi^0]$ channel becomes a background when one of the K_S 's decays inside the vertex. Because there is missing mass due to the lost π^0 , one of the V0 pions could assume the missing energy and mimic a kaon in the kinematic fit. This turns out to be the largest background, with 0.10% of the data. Note that there is no visible π^0 peak in figure 4.21. However, we do see *some* events at the V0 vertex, which is due to the second K_S , which is seen in figure 5.2. There are 60 ± 40 events seen in the fitted Gaussian on top of the 4th order polynomial, which translates to 0.10 ± 0.07 % of the Dalitz plot. This agrees perfectly with the hypothesis that this peak is due sole to $K_S K_S [\pi^0]$.

¹Compiled by Lucien Montanet of CERN

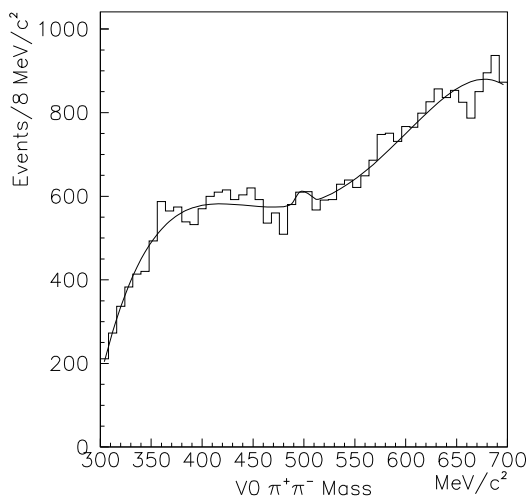


Figure 5.2: The small K_S contamination at V0. The curve is a Gaussian plus 4th order polynomial, with the small bump visible at 497 MeV.

5.3.3 $K_S[K_L] \pi^\pm \pi^\mp$

Out of 10000 events, no events survived into the Dalitz plot. Before the kinematic fit level, there were 4 events. The channel $K_S K_S[\pi^0]$ should have a similar kinematic fit efficiency, which was 6 out of 781 events. Thus the efficiency of $K_S[K_L]\pi^\pm\pi^\mp$ should be less than $4/10000 \times 6/781 = 3 \times 10^{-6}$.

5.3.4 $K\pi K_S[\pi^0]$

This is similar to the signal channel, except there is an additional π^0 . If the π^0 is very soft and undetected in the kinematic fit, this channel can feed through. Three Monte Carlo events survived out of 100000.

5.3.5 $4\pi^\pm[\pi^0]$

The $4\pi^\pm\pi^0$ channel is copiously produced in $p\bar{p}$ annihilation. However, because it lacks a tagging K_S , the feed-through is very small.

100K events were generated, but none survived all data processing cuts. We can put an upper limit on the efficiency. The last step where events existed was the after the “V0 inside target” cut, with 3 events. This is an efficiency of 3×10^{-5} . Now we compare to the $K_S K_S[\pi^0]$ channel, which should have a greater kinematic fit efficiency. This channel had 781 events at the “V0 inside target cut”, and then 6 events in the Dalitz plot, or less than 10^{-3} . Thus the efficiency for $4\pi^\pm\pi^0$ should be less than 3×10^{-8} .

5.3.6 $K_S K_S[\eta]$

This is very similar to the preceding channel, $K_S[K_L]\pi^\pm\pi^\mp$; the lost η is nearly the same mass as the lost K_L , so the kinematics are the same. We didn’t run any Monte Carlo for this channel, but use the same efficiency as $K_S[K_L]\pi^\pm\pi^\mp$.

5.3.7 $K_S K_S$

There is a small background from $K_S K_S$ Monte Carlo, but the branching ratio is very small. 6 events survived out of 100000 generated.

5.4 Acceptance Correction

The acceptance (or sometimes referred to the efficiency correction) of the detector varies as a function of the momenta of all particles. The biggest effect is the trigger acceptance, which is biased towards high momenta of the K_S . Also, the π^\pm and K^\pm are have low acceptances at low momentum because of curl ups or decays.

The partial wave analysis will only be accurate if the data is acceptance corrected. There are two methods of acceptance correction: The first method generates lots of Monte Carlo events, and divides the data by the Monte Carlo. The second method generates a smaller amount of Monte Carlo events and then fits a functional form, assuming some level of smoothness.

In order for the first method to work and not increase the statistical noise, the number of Monte Carlo events should be an order of magnitude more than the data. In this case, with roughly 50K data events in the Dalitz plot, we would like 500K MC events in the Dalitz plot. Our efficiency is on the order of 1.5%, so this would mean generating at least 30M MC events. With our fastest computer, we generate 100K events/day, so this would take 9 months of computing, which is clearly a waste of time.

Instead, we have generated 2M MC events of the form $K_S K^\pm \pi^\pm$ (in an equal ratio of both charge conjugate states). We then describe the net efficiency as a product of the efficiencies for each particle as a function of momentum, followed by an overall fudge-factor seventh-order polynomial. That is,

$$\epsilon_b = \frac{A_b}{A_0} \epsilon_{K^\pm}(p_{K^\pm}) \epsilon_{K_S}(p_{K_S}) \epsilon_{\pi^\pm}(p_{\pi^\pm}) p_7(x, y) \quad (5.1)$$

where A_b is the area of bin b within phase-space, A_0 is the total area of a bin, $\epsilon_x(p_x)$ is the efficiency of particle x as a function of the momentum of particle x , and $p_7(x, y)$ is an overall seventh order polynomial in terms of the Dalitz plot variables (x, y) , given in equation 5.6.

In most fits, the coefficients of the polynomial $p_7(x, y)$ are free. In a fit to just the Monte Carlo gives $(\chi^2)^{\text{mc}} = 630$. When both the Monte Carlo and data are fitted simultaneously, the χ^2 due to the Monte Carlo increases, of course, to compensate for a decrease in the χ^2 due to the data. This increase, is typically small, about $\Delta\chi^2 = 20 - 30$ for the best fits.

$$E(m_{12}, m_{23}) = E_1(p_1) E_2(p_2) E_3(p_3) p_7(m_{12}, m_{23}) \quad (5.2)$$

To determine the momentum efficiency from MC, we start with the fact that the MC is generated flat in phase space. The phase space factor for a dalitz plot is

$$dLIPS = dm_{12}^2 dm_{23}^2$$

which may be also written as

$$dLIPS = dE_3 dm_{23}^2$$

or

$$dLIPS = \frac{P_3}{E_3} dp_3 dm_{23}^2$$

If we plot p_3 for each generated MC event with the weight

$$w = \frac{E_3}{p_3 \int dm_{23}^2},$$

this weighted distribution will be a constant within the limits of phase space. Deviations from this constant factor give the momentum dependence. Note that the integral is

$$\int dm_{23}^2 = m_{23}^2(\text{max}, m_{12}) - m_{23}^2(\text{min}, m_{12})$$

A plot of the weighted K_S momentum distribution is given in figure 5.3. The efficiency is zero at zero momentum, and rises roughly linearly with momentum. (The last point at the end of the plot near 750 MeV has not been weighted correctly because the bin exceeds phase space, so it should be ignored. The same would go for the lowest momentum bin, but it has zero events.) The probability of a K_S to decay outside a cylinder of radius $\rho = 1.2$ cm is

$$E_{\text{SVX}}(p) = \int_{4\pi} d\Omega \exp\left(-\frac{\rho m}{p\tau \sin \theta}\right) \quad (5.3)$$

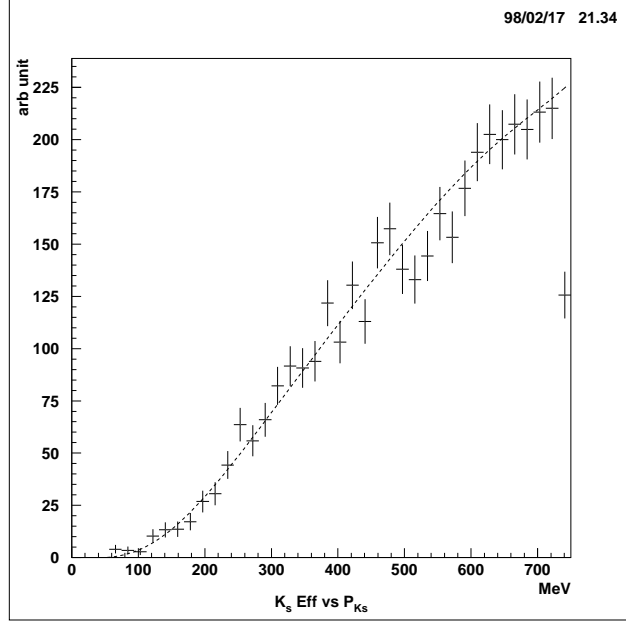


Figure 5.3: The efficiency as a function of K_S momentum. The histogram is due to the MC, while the smooth line is the functional form described in the text.

where $m = 497.672$ MeV, $\tau = 2.6762$ cm (in units where $c = \hbar = 1$). The limits of θ are determined by the JDC geometrical acceptance, but the functional form is relatively insensitive for values of $\theta = (0, 30^\circ)$.

We plot the form of E_{svx} in figure 5.3 with the appropriate normalization to the MC distribution. We see that the E_{svx} functional form describes the MC well.

There are additional corrections from the reconstruction efficiency of each track. To put these corrections in functional form, we generated 10000 Monte Carlo events each of K^+ and π^+ , distributed evenly in momentum space between 0 and 750 MeV. We then fit a parabolic function to each, with the following results.

$$E_\pi(p) = \begin{cases} (275.0 + 0.1p - 0.0002p^2)/333.3 & 125 < p \\ 275.0/333.3(p - 50.0)/75.0 & 50 < p < 125 \\ 0 & p < 50 \end{cases}$$

$$E_K(p) = \begin{cases} (84.0 + 0.47p - 0.00037p^2)/333.3 & 180 < p \\ (84.0 + 0.47p - 0.00037p^2)/(p - 140.0)/40.0/333.3 & 140 < p < 180 \\ 0 & p < 140 \end{cases}$$

$$E_{K_s}(p) = 1.0 + 0.0004p$$

The seventh order polynomial is found by simultaneously fitting the Monte Carlo and the data with the same function. In truth, since there are more statistics in the data, the data probably constrains the efficiency more than the Monte Carlo. The zeroth order term of the polynomial is set to 1, so there are $7(7+1)/2 - 1 = 35$ parameters. The fitted efficiency function (5.2) is shown in figure 5.4. The polynomial is a function of x, y which are

$$x = m_{12}^2 - 1.1\text{GeV}^2/c^4 \quad (5.4)$$

$$y = m_{23}^2 - 1.1\text{GeV}^2/c^4 \quad (5.5)$$

$$p\tau(x, y) = 1 + \sum_{i=1}^7 \sum_{j=0}^i c_{i-j,j} x^{i-j} y^j \quad (5.6)$$

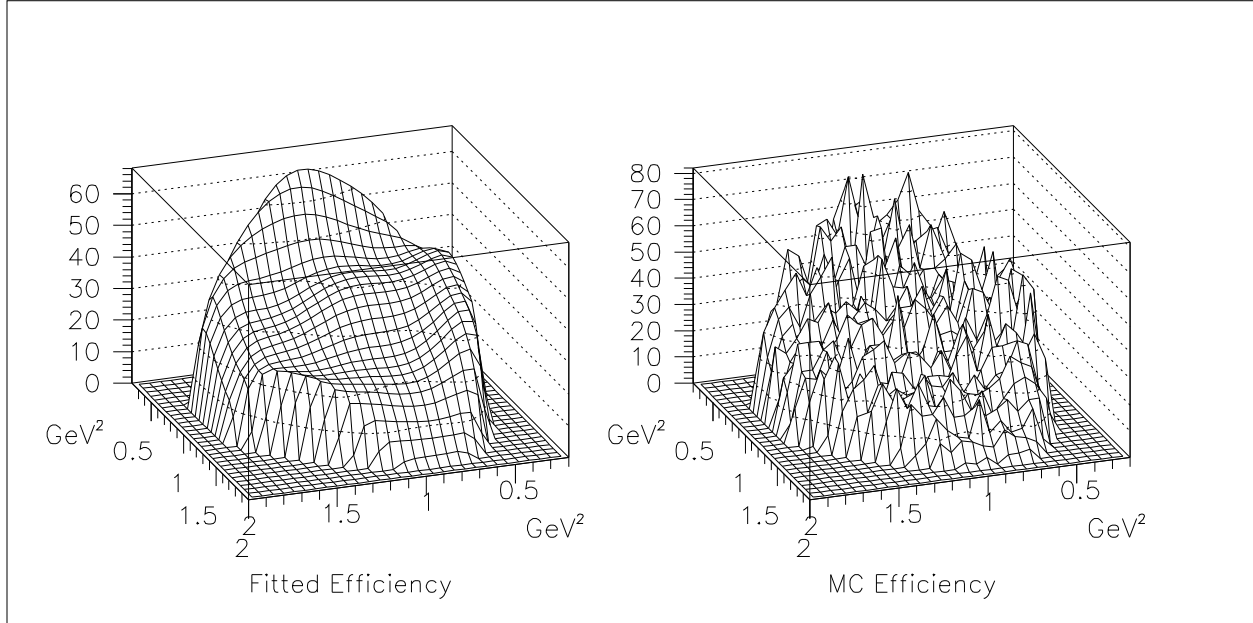


Figure 5.4: The acceptance function for the Dalitz plot. The fitted function (at left) is the result of a polynomial fit to the MC distribution (at right). The vertical scale is events per $0.06 \times 0.06 \text{ GeV}^4/c^8$.

The coefficients are given in table 5.2. We chose a seventh order polynomial, since seven was the minimum order that gave the best χ^2/N to the data. We show the efficiency fit for orders zero through eleven in figure 5.5.

We discovered quite late into the analysis that the random number seeds used for the various runs comprising this 2 million event Monte Carlo set were not adequately “random”, and that there were correlations between events. This caused the fit of the efficiency function to have an abnormally high $\chi^2/N \sim 1.7$, even when the function was expanded to 11th order. When each individual Monte Carlo run was individually fit (each with its own seed), the $\chi^2/N \sim 0.96$ to 1.2 at 7th order, regardless if the run was 100K, 200K, 300K or 500K events. Any combination of two runs caused the χ^2 to increase enormously to $\chi^2/N \sim 1.4$ to 1.6. In the interest of time, we did not regenerate the full statistics using the correct seeds, but used the only 500K event set of $K_S K^- \pi^+$, which fit the efficiency function with $\chi^2/N = 0.96$. We have shown in chapter 4 that the data is charge independent, so this single run is equivalent to using both $K_S K^- \pi^+$ and $K_S K^+ \pi^-$.

Term	Coefficient	Term	Coefficient	Term	Coefficient
x	-0.07 ± 0.24	y	-0.95 ± 0.22	x^2	-1.5 ± 0.65
xy	-0.67 ± 0.72	y^2	-2.2 ± 0.73	x^3	-3.0 ± 3.1
x^2y	9.2 ± 2.9	xy^2	-1.3 ± 3.4	y^3	8.1 ± 2.3
x^4	8.1 ± 3.5	x^3y	1.9 ± 5.5	x^2y^2	10.5 ± 8.5
xy^3	-6.7 ± 6.4	y^4	17.1 ± 4.0	x^5	$16.1 \pm 13.$
x^4y	$-19.0 \pm 12.$	x^3y^2	$-21.7 \pm 20.$	x^2y^3	$-55.7 \pm 17.$
xy^4	$35.5 \pm 15.$	y^5	-33.8 ± 8.4	x^6	-12.5 ± 5.7
x^5y	$-1.0 \pm 12.$	x^4y^2	$-14.5 \pm 20.$	x^3y^3	$18.1 \pm 23.$
x^2y^4	$-13.9 \pm 25.$	xy^5	$27.6 \pm 14.$	y^6	-29.0 ± 6.0
x^7	$-23.0 \pm 16.$	x^6y	$7.8 \pm 19.$	x^5y^2	$54.3 \pm 33.$
x^4y^3	$76.5 \pm 40.$	x^3y^4	$23.3 \pm 46.$	x^2y^5	$110.0 \pm 34.$
xy^6	$-66.4 \pm 23.$	y^7	$43.6 \pm 10.$		

Table 5.2: The coefficients for the seventh order “fudge-factor” polynomial

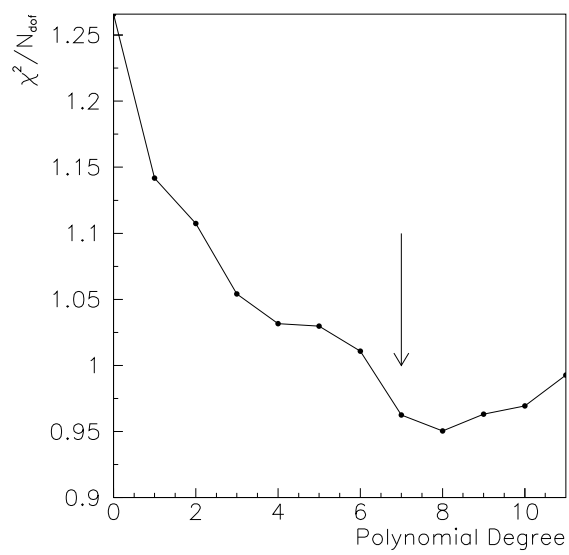


Figure 5.5: The pure efficiency fit as a function of polynomial degree

Chapter 6

Absolute branching ratio measurement

In order to calculate the total branching ratio, minimum bias events are counted and then corrected for acceptance. To select the proper events, we use the same cuts as in chapter 4, except for one difference. Because we do not need to simulate the online K_S trigger, we do not apply the trigger simulator to the Monte Carlo.

Of 154 300 generated $K_S K^\pm \pi^\pm$ Monte Carlo events, 5660 are accepted into the final Dalitz plot.

There were 867 995 minimum bias events collected during the April 1996 run. The minimum bias trigger simply requires an incoming \bar{p} and no outgoing \bar{p} downstream. Of these, 86 survive into the $K_S K^\pm \pi^\pm$ Dalitz plot after applying all of the same cuts there were applied to the triggered data, except for the online trigger condition. These 86 events are well spread over the Dalitz plot, as shown in figure 6.1.

Because the acceptance varies considerably, each event must be individually corrected, rather than taking the total number of events and dividing by the acceptance.

To correct for the acceptance variation, the

$$N_{\text{mb-cor}} = \frac{N_{\text{mc-tot}} A_i}{A_{\text{tot}}} \sum_{\text{events}_i} \frac{1}{n_i}$$

where A_{tot} and A_i are the areas of the total Dalitz plot and the bin, respectively,

$$A_{\text{tot}} = 1.71126 \text{ GeV}^4/c^8 \quad (6.1)$$

$$A_i = 0.06 \text{ GeV}^2/c^4 \times 0.06 \text{ GeV}^2/c^4 = 0.0036 \text{ GeV}^4/c^8 \quad (6.2)$$

$$N_{\text{mc-tot}} = 154\,300, \quad (6.3)$$

and n_i is the number of Monte Carlo events in the closest bin to the i -th minimum bias event. For bins on the boundary of phase space, the value of n_i is corrected by dividing by the fractional area within phase space. This gives

$$N_{\text{mb-cor}} = 2390^{+330}_{-260}$$

where the negative error is statistical and the positive error is due to one specific minimum bias event that appears to be an outlier. This event is the right-most dot on the Dalitz plot in figure 6.1.

Thus the branching ratio is

$$BR(K_S K^\pm \pi^\pm) = \frac{N_{\text{mb-cor}}}{N_{\text{mb-tot}}} \quad (6.4)$$

$$= \frac{2390^{+330}_{-260}}{867\,995} \quad (6.5)$$

$$= (2.7^{+0.4}_{-0.3}) \times 10^{-3} \quad (6.6)$$

This agrees within 2σ with Baresh *et al.* [21] ($\frac{1}{2}\text{BR}(K^0 K^\pm \pi^\mp) = (2.13 \pm 0.28) \times 10^{-3}$), and within 1σ with Armenteros *et al.* [16] ($\text{BR}(K_S K^\pm \pi^\pm) = (2.82 \pm 0.11) \times 10^{-3}$) and with the equivalent Crystal Barrel result [4] ($\text{BR}(K_L K^\pm \pi^\mp) = (2.91 \pm 0.34) \times 10^{-3}$).

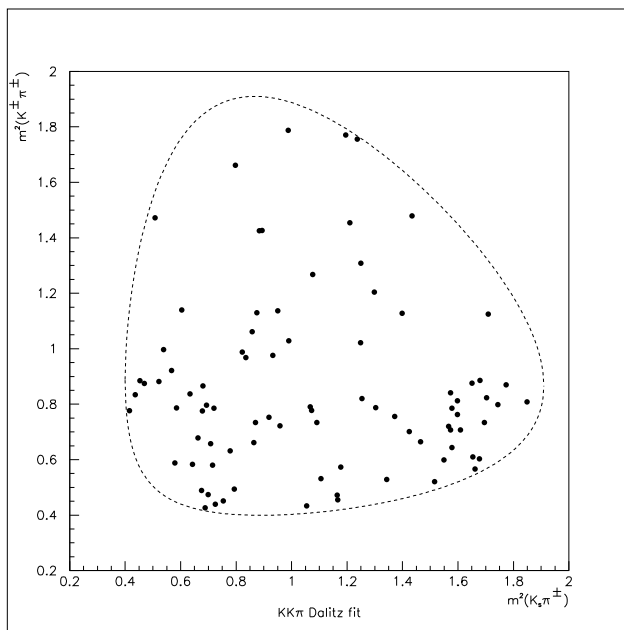


Figure 6.1: The Dalitz plot from 86 minimum bias events. The rightmost data point is discussed in the text.

As these are all independent measurements, the error-weighted average of all four measurements is

$$\text{BR}(K_S K^\pm \pi^\pm) = (2.68 \pm 0.14) \times 10^{-3}. \quad (6.7)$$

Chapter 7

Partial Wave Analysis

7.1 Introduction to Partial Wave Analysis

The primary purposes of this analysis are to quantitatively measure the masses, widths and branching ratios of the intermediate isobar resonances involved in the reaction $K_S K^\pm \pi^\pm$. Up to this point, the data selection has worked to select out the three final state particles, but has not made any requirements on the isobars.

Selection of the isobars is not a trivial task. Because the isobars decay via the strong interaction, their lifetimes are very short and hence widths are very wide. A typical isobar width is on the order of 100 MeV, much wider than the experimental resolution. Therefore one can not simply count the number of events in a narrow mass window to measure the isobars. More importantly, since there are many wide isobars in the same reaction, there is a lot of overlap, causing quantum mechanical interferences between the resonances.

Thus in order to determine the masses, widths and especially branching ratios of the resonances, a full theoretical calculation of the quantum mechanical amplitude is necessary. Each amplitude due to each resonance must be carefully summed, either coherently or incoherently as necessary.

We wish to calculate this amplitude using the fewest number of independent observables. For this, we use a Dalitz plot.

7.1.1 Dalitz plot

The differential Lorentz Invariant Phase Space (dLIPS) is given by

$$d\Phi(P; p_1, \dots, p_n) = \prod_{i=1}^n \frac{d^3 p_i}{(2\pi)^3 2E_i}$$

where P is the total four-momentum and p_i the four-momentum of particle i . Since $n = 3$ for $p\bar{p} \rightarrow K_S K^\pm \pi^\pm$, there are 12 parameters (p_i^μ) describing phase space. Since all of the particles are identified and have a unique mass, this removes 3 arbitrary parameters ($p_0 = \sqrt{p_i^2 + m^2}$), leaving 9 parameters. We have applied a 4C kinematic fit to the data, requiring total energy and momentum conservation. Thus the number of parameters describing the phase space is further reduced by 4 to 5, and dLIPS becomes

$$d\Phi(p_1, \dots, p_n) = \int_P \delta^4(P - \sum_{i=1}^n p_i) d\Phi(P; p_1, \dots, p_n)$$

which simplifies to the 5 parameter expression

$$d\Phi(E_1, E_3, \alpha, \beta, \gamma) = \frac{1}{8(2\pi)^5} dE_1 dE_3 d\alpha d(\cos\beta) d\gamma$$

where E_1, E_3 are the energies of two of the three particles and α, β, γ are the Euler angles that describe the plane of the final three particles. At-rest annihilation is not polarized, so there is no external orientation that affects the physics, so we integrate over the three Euler angles, reducing the parameters to only 2,

$$d\Phi(E_1, E_3) = \frac{1}{4(2\pi)^7} dE_1 dE_3.$$

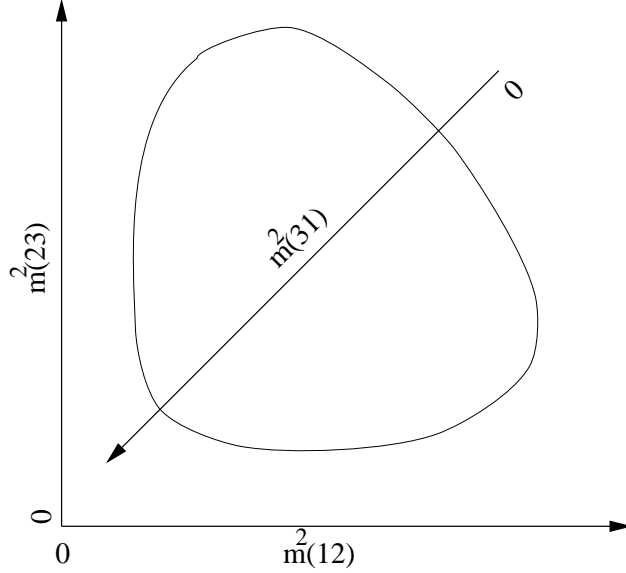


Figure 7.1: The Dalitz plot m^2 axes.

The energy values E_i are dependent on the total center-of-mass energy, but we prefer Lorentz invariant quantities. We note that in the center of mass system where $P = (\sqrt{s}; 0, 0, 0) = p_1 + p_2 + p_3$,

$$m_{12}^2 = (p_{12})^2 \quad (7.1)$$

$$= (P - p_3)^2 \quad (7.2)$$

$$= P^2 + p_3^2 - 2(E E_3) + 2\vec{P} \cdot \vec{p}_3 \quad (7.3)$$

$$= \sqrt{s}^2 + m_3^2 - 2(\sqrt{s} E_3) \quad (7.4)$$

$$d(m_{12}^2) = 0 + 0 - 2\sqrt{s} dE_3. \quad (7.5)$$

Thus we can substitute $dE_1 = -\frac{1}{2\sqrt{s}} m_{23}^2$ and $dE_3 = -\frac{1}{2\sqrt{s}} m_{12}^2$ and get

$$d\Phi(m_{12}^2, m_{23}^2) = \frac{1}{16(2\pi)^7 \sqrt{s}^2} dm_{12}^2 dm_{23}^2.$$

Then the rate of the process is just

$$\Gamma = \frac{(2\pi)^4}{2\sqrt{s}} |\mathcal{M}|^2 d\text{LIPS} \quad (7.6)$$

$$= \frac{1}{(2\pi)^3 32\sqrt{s}^3} |\mathcal{M}|^2 dm_{12}^2 dm_{23}^2 \quad (7.7)$$

where the coefficient is a constant over the Dalitz plot. This simple expression shows that the intensity of the Dalitz plot at a point (m_{12}^2, m_{23}^2) is directly proportional to the matrix element squared. There is no additional phase space term.

The particles are labeled in this fashion: 1=a= K_S , 2=b= π^\pm , 3=c= K^\pm . The Dalitz plot has two orthogonal axes, m_{12}^2 and m_{23}^2 ; the third axis m_{31}^2 is measured diagonally, starting with zero at upper-right and increasing while moving to the left and down, as seen in figure 7.1. In this Dalitz plot,

Axis	Equivalent	Example Isobar
m_{12}^2	$m^2(K_S \pi^\pm)$	$K^*(892)^\pm$
m_{23}^2	$m^2(K^\pm \pi^\mp)$	$K^*(892)^0$
m_{31}^2	$m^2(K_S K^\pm)$	$a_2(1320)^\pm$

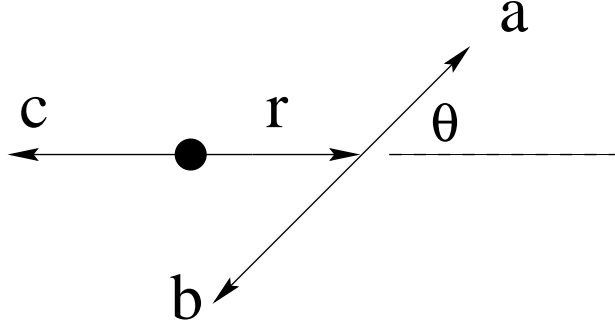


Figure 7.2: The isobar model showing $p\bar{p} \rightarrow r + c$, $r \rightarrow a + b$

7.2 The total intensity

As discussed in chapter 2, the different initial states of $p\bar{p}$ are produced incoherently. Thus each the contribution from each initial state is added incoherently. For a specific initial state, all amplitudes that produce the same final state are added coherently. The intensity of the Dalitz plot is calculated as

$$I(m_{ab}^2, m_{bc}^2) = \sum_{\text{initial states, } J_z} \left| \sum_{r,L,\text{axes}} A_r(\vec{J}, L, l, m_{ab}, m_{bc}) \right|^2 \quad (7.8)$$

The sum over axes represents the three pair-wise combinations of the final particles.

7.3 The matrix element

The matrix element A of the process (see figure 7.2)

$$p\bar{p} \rightarrow \begin{array}{l} r + c \\ \searrow \\ a + b \end{array}$$

is given by

$$A_r(\vec{J}, L, l, m_{ab}, m_{bc}) = Z(\vec{J}, L, l, \cos\theta) F_L(p_{rc}) \hat{T}_r(m_{ab}), \quad (7.9)$$

where

- r is the resonance particle
- a, b are the decay particles of the resonance r
- c is the spectator particle
- J is the total angular momentum of entire system ($p\bar{p}$ or rc)
- L is the orbital angular momentum between r and c
- l is the orbital angular momentum between a and b
- \vec{p}_{rc} is the break-up momentum in the $r - c$ system
- \vec{q}_{ab} is the break-up momentum in the $a - b$ system
- $\cos\theta_{ac}$ is the angle between \vec{p} and \vec{q} in the $a - b$ system.
- m_{ab} is the invariant mass of the $a - b$ system
- $Z()$ is the Zemach function which describes the angular distribution of the particles
- $F()$ is the Blatt-Weisskopf barrier factor for the production of $r - c$ with angular momentum L
- $\hat{T}_r()$ is the dynamical function describing the width of resonance r

Note that some of these parameters are redundant. $\cos\theta$ is derived from \vec{p} and \vec{q} , which are in turn derivable from m_{12}^2 and m_{23}^2 .

Rank (L)	N_F ($2L + 1$)	Tensor	$J = L \oplus l$	Coupled Tensor
0	1	$P = 1$	$0 = 0 \oplus 0$	$Z = PQ$
		$Q = 1$	$0 = 1 \oplus 1$	$Z = \overline{P}_i \overline{Q}_i$
			$0 = 2 \oplus 2$	$Z = \overline{P}_{ij} \overline{Q}_{ij}$
1	3	$\overline{P}_i = \hat{p}_i$	$1 = 0 \oplus 1$	$\overline{Z}_i = P \overline{Q}_i$
		$\overline{Q}_i = \hat{q}_i$	$1 = 1 \oplus 0$	$\overline{Z}_i = \overline{P}_i Q$
2	5	$\overline{P}_{ij} = \hat{p}_i \hat{p}_j - \frac{1}{3} \delta_{ij}$	$1 = 1 \oplus 1$	$\overline{Z}_i = \epsilon_{ijk} \overline{P}_j \overline{Q}_k$
		$\overline{Q}_{ij} = \hat{q}_i \hat{q}_j - \frac{1}{3} \delta_{ij}$	$1 = 2 \oplus 1$	$\overline{Z}_i = \overline{P}_{ij} \overline{Q}_j$
			$1 = 1 \oplus 2$	$\overline{Z}_i = \overline{P}_j \overline{Q}_{ji}$
			$2 = 0 \oplus 2$	$\overline{\overline{Z}}_{ij} = P \overline{\overline{Q}}_{ij}$
			$2 = 2 \oplus 0$	$\overline{\overline{Z}}_{ij} = \overline{P}_{ij} Q$
			$2 = 1 \oplus 2$	$\overline{\overline{Z}}_{ij} = T \cdot S(\epsilon_{ikl} \overline{P}_k \overline{\overline{Q}}_{lj})$
			$2 = 2 \oplus 1$	$\overline{\overline{Z}}_{ij} = T \cdot S(\epsilon_{jkl} \overline{P}_{ik} \overline{\overline{Q}}_l)$
			$2 = 2 \oplus 2$	$\overline{\overline{Z}}_{ij} = T \cdot S(\overline{P}_{ik} \overline{\overline{Q}}_{kj})$

Table 7.1: The definitions of the P and Q Zemach tensors (left) and the coupling of the P and Q tensors to form the Z tensor (right). $S()$ is the symmetrization operator $S(X_{ij}) = \frac{1}{2}(X_{ij} + X_{ji})$, and $T()$ is the trace-removing operator, $T(X_{ij}) = X_{ij} - \frac{1}{3}\delta_{ij}\text{Tr}(X)$

7.4 The Zemach formalism

The Zemach functions[48] are used to describe the angular distributions of the decays of the resonances. An unpolarized particle in free space decays uniformly. However, because of the coupling of the two orbital angular momenta L and l to J , certain magnetic sub-states are forbidden by the Clebsch-Gordan coefficients. For example, let us pick a reaction with $L = 1$ and \hat{z} defined along the direction of \vec{p} , the resonance momentum. Then

$$L_z = \hat{z} \cdot \vec{L} \sim \vec{p} \cdot (\vec{p} \times \vec{r}) = 0.$$

Then the state $|L L_z\rangle = |1 0\rangle$ is empty while the states $|1 \pm 1\rangle$ are not. This essentially polarizes the resonances along their momentum direction, and thus the decay pattern is governed by the shapes of the $Y_l^m(\theta, \phi)$ spherical harmonics. In general the magnetic states are populated symmetrically in m , so all distributions are symmetric in $\cos\theta$. In addition, because there is only one axis of polarization \hat{z} , the azimuthal decay distribution is flat. The distributions as calculated by Zemach are given in table 7.2 if one sets the relativistic correction parameter z to zero, see (7.10).

The formalism is based on the Wigner-Eckart theorem, which separates a matrix element into the angular part (which is the Zemach tensor) and into the reduced matrix element which does not depend on the orientation in space. The recipe for forming the Zemach tensor is as follows.

Construct a representation of the angular momentum group, and then form combinations of the elements that transform in the desired way. For instance, consider coupling $L = 1$ (quantized on the \hat{p} axis) with $L = 1$ (quantized on the \hat{q} axis to get $L = 0$ (on any axis). An $L = 1$ state transforms as a 3-component vector (e.g. Y_1^m with $m = -1, 0, +1$); let us choose the axis of quantization to represent it. The final $L = 0$ transforms as a scalar; $\hat{p} \cdot \hat{q} = \cos\theta$ also transforms as a scalar. Then the amplitude due to coupling transforms as that scalar, and the intensity $|A|^2$ transforms as $\cos^2\theta$, which is the right answer. An $L = 2$ state transforms as a 5-component tensor (e.g. Y_2^m with $m = -2, -1, 0, +1, +2$).

First construct the Zemach tensors for $L = 0, 1, 2$ and $l = 0, 1, 2$ (see table 7.1). Then contract the tensors together, using δ_{ij} or ϵ_{ijk} as necessary, to get a tensor with the proper rank of J . For rank-2 tensors, take linear combinations to verify that the final tensor is traceless and symmetric. This final tensor is

The components of the coupled tensor are amplitudes of each of the components of angular momentum J . Because the coherence between different $|J_z\rangle$ states of the same J is destroyed by the $p\bar{p}$ annihilation cascade, the amplitudes due to each state of J_z are summed incoherently.

State	J	L	l	Angular distribution	$z \neq 0 ?$	Isobars
1S_0	0	0	0	1		$K_0^* K, a_0 \pi$
	0	1	1	$\cos^2 \theta$		$K_1^* K, \rho \pi$
	0	2	2	$(\cos^2 \theta - \frac{1}{3})^2$		$K_2^* K, a_2 \pi$
3S_1	1	1	1	$\sin^2 \theta$		$K_1^* K, \rho \pi$
	1	2	2	$-(1+z^2) - 2 + 4z^4 \cos^4 \theta + 4z^2 \cos^2 \theta + (1+z^2)^2 + 16(1+z^2) \cos^2 \theta - 16(1+z^2)^2 \cos^4 \theta$ which simplifies to $(\cos \theta \sin \theta)^2$ if $z = 0$	•	$K_2^* K, a_2 \pi$
1P_1 and 3P_1	1	0	1	$1 + z^2 \cos^2 \theta$	•	$K_1^* K, \rho \pi$
	1	2	1	$1 + (3 + 4z^2) \cos^2 \theta$	•	-
	1	1	0	1		$K_0^* K, a_0 \pi$
	1	1	2	$(1+z^2) [\frac{1}{3} \cos^2 \theta + 3z^2 (\cos^2 \theta - \frac{1}{3})^2]$	•	$K_2^* K, a_2 \pi$

Table 7.2: Relativistic Zemach Angular distribution functions. Those which depend on z are marked with a bullet.

The Zemach formalism is restricted to reactions where a, b and c are spin-0 particles, which applies in this case. For final states with vector particles (ω, γ), the helicity formalism is needed.

Even though the Zemach formalism has been used successfully in $p\bar{p}$ annihilation analyses for thirty years, it is not covariant. A covariant form (the Rarita-Schwinger form) has been given by Filippini *et al.*[34]. The authors suggest that there can be significant differences for certain resonances in certain initial states due to the relativistic corrections. The fact there are non-uniform distributions at all is given by the fact that certain magnetic sub-states of the angular momentum are not populated evenly. The relativistic effect causes even more uneven population of the magnetic states because of the Lorentz boost.

The present analysis has been done using the non-relativistic Zemach functions. In table 7.2 we show the relativistic Zemach functions. They are functions of z ,

$$z = |p_{rc}|/m_r = \sqrt{\gamma^2 - 1} \quad (7.10)$$

In the non-relativistic limit of $\beta \rightarrow 0$ or $\gamma \rightarrow 1$, then $z = 0$. The largest z comes from the lightest and fastest moving resonances, i.e. the $K^*(892)$. The following table gives the z^2 values for the different spin-1 or spin-2 isobars. Spin-0 isobars always decay uniformly.

Intermediate	p	m range	z^2
$K_1^* K$	618	865 to 915	0.53 to 0.43
$a_2(1320)\pi$	458	1220 to 1420	0.19 to 0.07
$\rho(1450)\pi$	357	1350 to 1550	0.10 to 0.03
$K_2^* K$	0	1330 to 1430	0.02 to 0.00

Looking at table 7.2, one can see that there are *no* relativistic corrections for any state coming from 1S_0 . From 3S_1 annihilation there is only one function that is affected by the relativistic correction ($\langle J|L l \rangle = \langle 1|2 2 \rangle$). The $a_2(1320)\pi$ contribution from this initial state is about 2% according to the partial wave analysis, and the $z^2 \sim 0.13$ so this is a small effect.

In P -wave annihilation, only the $\rho(1450)\pi$ and $K_1^* K$ isobars have significant amplitude, and of these two only the $K_1^* K$ amplitude has a significant z factor for relativistic distortion of the angular amplitude, shown in figure 7.3. The non-relativistic flat distribution begins to look more like $\sim 1 + \cos^2 \theta$. Because the $K_1^* K$ also originates from 1S_0 and 3S_1 initial states, this error can be compensated in the fit by increasing the 1S_0 contribution.

In order to determine the impact on the $K_1^* K$ branching ratio, we have repeated the fit using *no* $K_1^*(892)K$ contribution from 1P_1 . The total branching ratio for the $K_1^*(892)K$ decreased by only 5%. Because the relativistic distortion effect is much smaller than total removal of the entire partial wave, we estimate that the error that the distortion brings to the branching ratio at less than 2%, which is smaller than the statistical error in table 8.2.

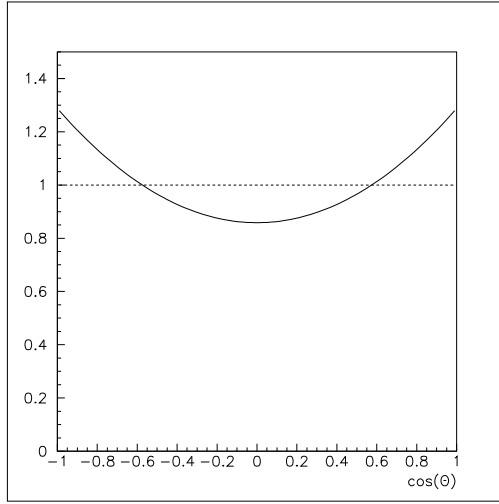


Figure 7.3: The decay distribution of the K^* from 1P_1 or 3P_1 , calculated non-relativistically (dotted line) and relativistically (solid line)

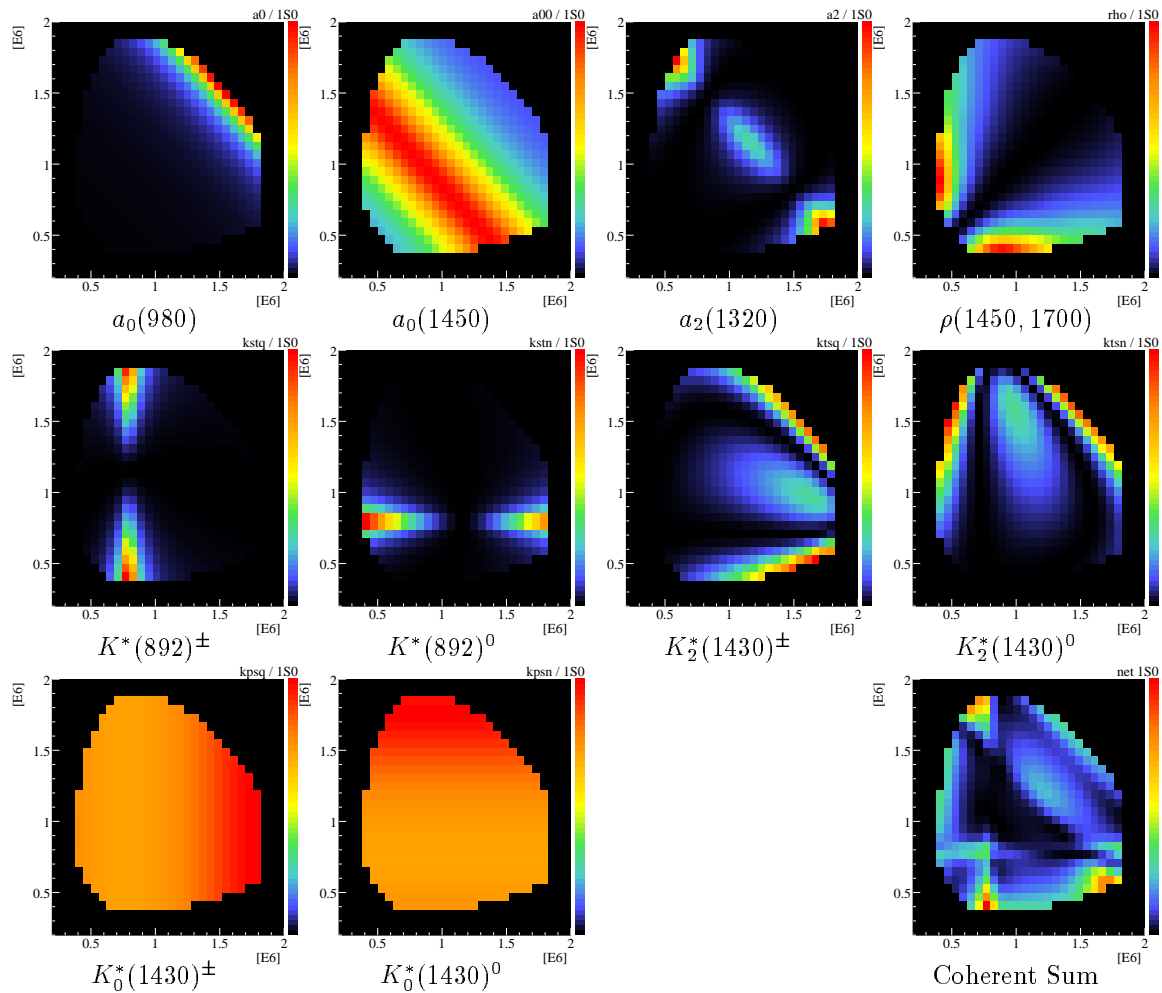


Figure 7.4: The 1S_0 Partial Waves

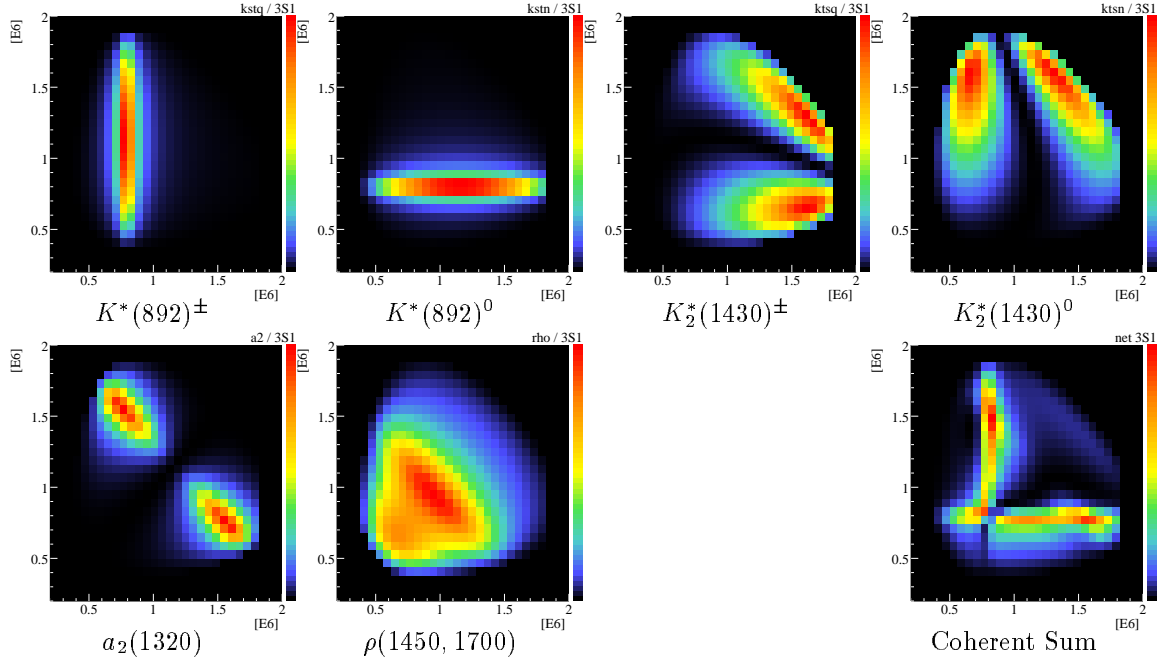


Figure 7.5: The 3S_1 Partial Waves

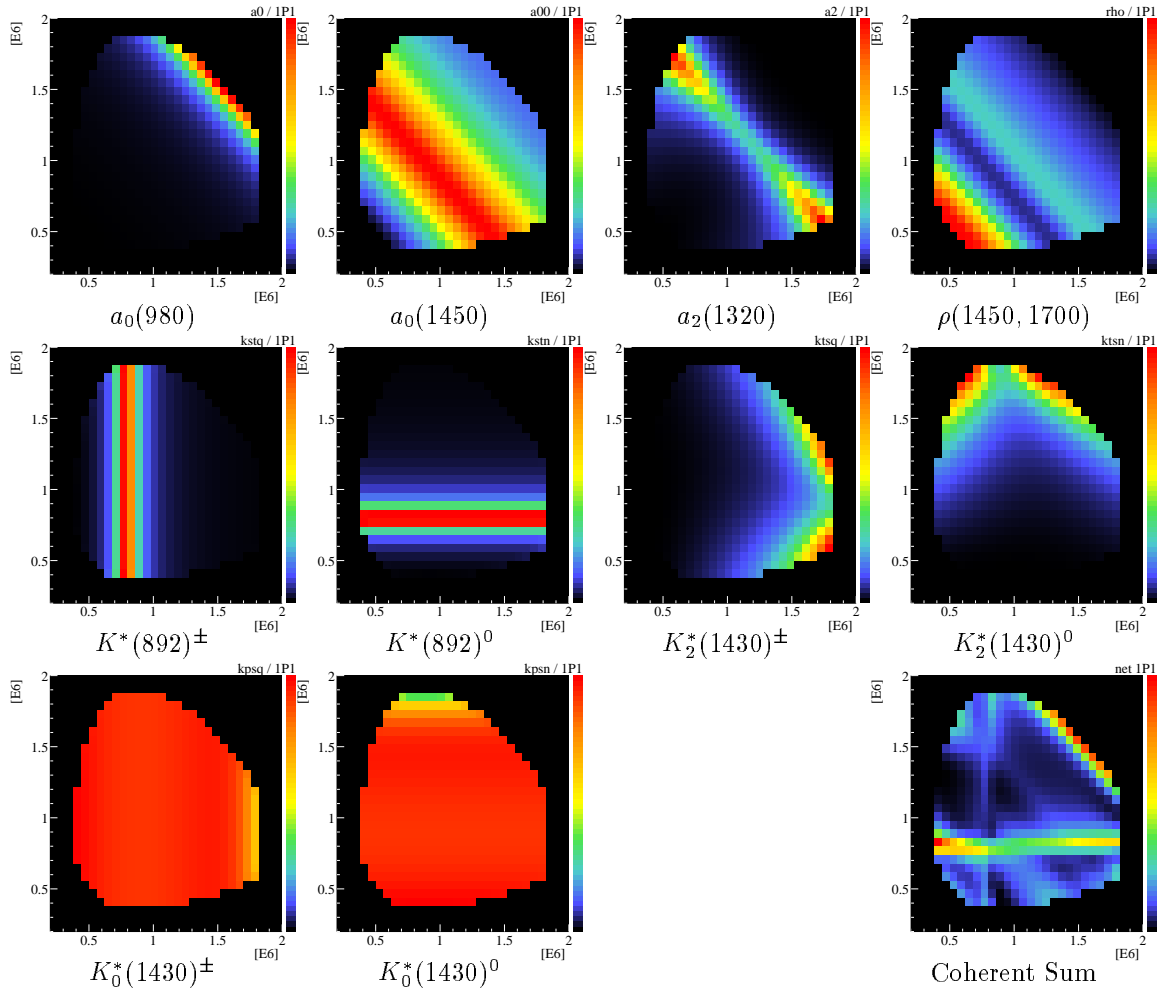


Figure 7.6: The 1P_1 and 3P_1 Partial Waves

7.5 Two-body breakup momentum and phase space

The breakup momentum for a system into two particles with masses m_a and m_b is

$$q_{ab} = \frac{\sqrt{[m_{ab}^2 - (m_a + m_b)^2][m_{ab}^2 - (m_a - m_b)^2]}}{2m_{ab}}$$

where m_{ab} is the invariant mass of the system.

The phase space of a two body decay is

$$\rho(m_{ab}) = \frac{2q_{ab}}{m_{ab}}.$$

7.6 Angular barrier factor

Because the strong force only works over small distances, i.e. 1 fm, the maximum angular momentum L possible in a strong decay is limited by the linear momentum p

$$\vec{L} = \vec{r} \times \vec{p} \quad (7.11)$$

$$L = (1 \text{ fm}) \cdot |p|. \quad (7.12)$$

In other words, decay particles moving very slowly with an impact parameter of order of the size of the resonance (i.e. 1 fm) can not generate enough angular momentum to conserve the spin of the resonance. The functions calculated by Blatt and Weisskopf[47] weight the reaction amplitudes to account for this spin-dependent effect. The functions $F_L(z)$ for resonances with $L = 0, 1, 2$ are

$$F_0(q) = 1 \quad (7.13)$$

$$F_1(q) = \sqrt{\frac{z}{z+1}} \quad (7.14)$$

$$F_2(q) = \sqrt{\frac{13z^2}{(z-3)^2 + 9z}} \quad (7.15)$$

where the unitless quantity $z = (qR)^2$ is in terms of the breakup momentum q and the range of the interaction, 1 fermi or $R = 1/200 \text{ MeV}^{-1}c$. See figure 7.7 for the shape of these functions.

It is convenient to define the normalized Blatt-Weisskopf functions

$$B^L(q, q_0) = \frac{F_L(q)}{F_L(q_0)} \quad (7.16)$$

where q_0 is the value of q on resonance.

These functions appear in two places. The first place is as a momentum-dependent correction to the “width” of a resonance Γ_0 . The second is as a momentum-dependent correction to the overall amplitude, which appears in the production factors.

7.7 Dynamical functions $\hat{T}_r(m)$

Nearly all resonances in $p\bar{p}$ physics are characterized by the complex energy poles (E_0) of the transition matrix \hat{T} ,

$$E_0 = m_0 - i\Gamma_0/2 \quad (7.17)$$

where the real part m_0 is the central resonance mass and the imaginary part $i\Gamma_0/2$ contains the defined width.

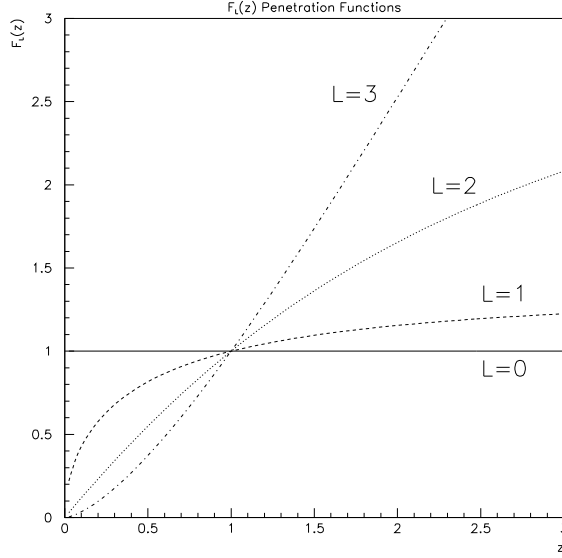


Figure 7.7: The Blatt-Weisskopf functions for $L = 0, 1, 2$

7.7.1 Breit-Wigner

One of the simplest forms for T is the Breit-Wigner form, which is derived from 2-particle partial wave scattering phenomenology for narrow resonances ($\Gamma \ll m_0$). Briefly, the elastic scattering amplitude (non-relativistic) is

$$f = \frac{1}{\cot \delta - i}$$

which has a maximum at $\delta = \pi/2$. If $\Gamma_0/m_0 \ll 1$, and defining $2/\Gamma = d \cot \delta / d m|_{m=m_0}$, this can be written as

$$f \approx \frac{\Gamma_0/2}{(m_0 - m) - i\Gamma_0/2}$$

where m is the invariant mass of the decay particle system, where Γ is defined in terms of a fast moving phase. Note the pole positions are in the correct place, as given by (7.17). The relativistic form is written as

$$f = \frac{\Gamma_0 m_0}{(m_0^2 - m^2) - im_0 \Gamma_0}, \quad (7.18)$$

again with the T pole position in the same spot (but only if $\Gamma_0 \ll m_0$).

Of course, since many resonances are wide, the assumption $\Gamma_0 \ll m_0$ does not hold well. This was first noted in the ρ -meson ($\Gamma_0/m_0 = 150/770 = 19\%$) where deviations from the Breit-Wigner are visually apparent. In this case, the Breit-Wigner is given a varying width, which is usually proportional to the phase-space of the decaying particles. In addition, resonances with spin have a dependence on momentum due to the centrifugal barriers (equation 7.16). Thus the improved Breit-Wigner looks like

$$f = \frac{\Gamma_0 m_0 B^l(q, q_0)}{(m_0^2 - m^2) - im_0 \Gamma_0 \left[\frac{\rho(m)}{\rho(m_0)} \right] [B^l(q, q_0)]^2} \quad (7.19)$$

where $\rho(m)$ is the phase space and $B^l(q, q_0)$ are the normalized Blatt-Weisskopf functions given in (7.16).

For this analysis, the Breit-Wigner function is used to parameterize all resonances except for the $a_0(980)$ which requires a Flatté distribution and for the $\rho(1450)$ and $\rho(1700)$ which require the K -matrix because of the proximity of the resonance poles.

A variation of the Breit-Wigner uses m instead of m_0 in the numerator and in the third term of the denominator. A refit of fit #81 using this hypothesis insignificantly changed the χ^2 by 1.99 less, and did

not change any of the branching ratios by more than $\sim 10\%$ except for the 1S_0 contribution from $a_2(1320)$ which decreased by 21%.

7.7.2 K -matrix

The K -matrix formalism is more general than that the Breit-Wigner function. It allows having more than one T matrix pole and coupled channels, while preserving unitarity. In fact, the Breit-Wigner function is equivalent to a one-pole, one-channel K -matrix and the Flatté function is equivalent to a one-pole, two-channel K -matrix. The derivation of the Flatté form from the K -matrix is given in [28]. Here we just give the 1×1 description of the K -matrix, which is used for the $K_0^*(1430)$ S-wave and the multiple pole ρ resonance.

In scattering applications, the T matrix looks like

$$\hat{T} = (1 - i\rho\hat{K})^{-1}\hat{K} \quad (7.20)$$

where the 1×1 K matrix is a summation of pole terms,

$$\hat{K} = \sum_{i=\text{poles}} \frac{(gB^L(q))^2}{m_i^2 - m^2} + c \quad (7.21)$$

where $g = \sqrt{m_i\Gamma_i/\rho}$, ρ is the decay phase space, $B^L(q)$ is the Blatt-Weisskopf factor, m_i is the resonance mass, m is the invariant mass of the system and c is an optional background term.

In production applications, such as in $p\bar{p}$ annihilation, the T matrix is written as

$$\hat{T} = (1 - i\rho\hat{K})^{-1}\hat{P}, \quad (7.22)$$

the only difference being the production vector P replacing the K matrix. The production vector is defined as

$$\hat{P} = \sum_{i=\text{poles}} \beta_i \frac{g^2 B^L(q)}{m_i^2 - m^2} + c \quad (7.23)$$

which is nearly the same as the K matrix, except there is a production coefficient β_i and one power of $B^L(q)$ is suppressed.

Flatté

The Flatté distribution is used to parameterize the $a_0(980)$. Because the a_0 's mass is on top of the KK threshold and it can also decay into $\pi^0\eta$, the shape is affected in a somewhat weird way. See the discussion around equation (2.18) for a description of the dynamical form,

$$\hat{F}(s) = \frac{g_1}{m_0^2 - m^2 - i(\rho_1 g_1^2 + \rho_2 g_2^2)}.$$

The ρ P-wave

The ρ is described by a two pole K -matrix, with

$$(m_1, \Gamma_1) = (1430, 170) \text{ MeV} \quad (7.24)$$

$$(m_2, \Gamma_2) = (1740, 190) \text{ MeV}, \quad (7.25)$$

the values taken from [4].

$K - \pi$ S-Wave

The LASS parameterization of the $K - \pi$ S-wave requires a broad background term c to be added to the pole term. The value of c in (7.21) and (7.23) is defined as

$$c = \frac{am}{2 + abq^2(m)}. \quad (7.26)$$

It turns out that the fit is not very sensitive to the exact parameterization of the background term. The negative log-likelihood actually drops slightly (by 15) if the background term is not included. The dynamical form is discussed in section 2.11.2.

Table 7.3: Results of every fit, with percentages of each resonance

7.8 Fit algorithm

In most analyses, the efficiency function is calculated from the Monte Carlo, and then held constant in the fits. In this analysis however, because the statistics of the data are much higher than the statistics of the Monte Carlo, the efficiency can be better determined by using the *data* rather than the Monte Carlo. Of course, the data reflects both the efficiency and the dynamics. For this reason, we simultaneously fit the Monte Carlo (for the efficiency) and the data (for the efficiency and the dynamics).

MINUIT was used to minimize our χ^2 value,

$$\chi^2 = \chi_{\text{mc}}^2 + \chi_{\text{data}}^2 \quad (7.27)$$

where

$$\chi_{\text{mc}}^2 = \sum_{b=\text{bins}} \chi^2(N_b^{\text{mc}}, \epsilon_b \cdot c) \quad (7.28)$$

and

$$\chi_{\text{data}}^2 = \sum_{b=\text{bins}} \chi^2(N_b^{\text{data}}, \epsilon_b \cdot I_b) \quad (7.29)$$

where b is the bin index, N_b is the number of events in bin b , ϵ_b is the net detector and reconstruction efficiency of bin b , c is an overall normalization constant and I_b is the total theoretical intensity of bin b . The χ^2 for binned Poisson data is the same as twice the negative log-likelihood,

$$\chi^2(N^{\text{obs}}, N^{\text{th}}) = -2LL = 2(N^{\text{th}} - N^{\text{obs}} + N^{\text{obs}} \ln(N^{\text{obs}}/N^{\text{th}})) \quad (7.30)$$

where N^{obs} is the observed integral number of events and N^{th} is the theoretically expected real number of events. If $N^{\text{obs}} = 0$, then the second term is zero.

Both ϵ_b and I_b are calculated at the phase-space center-of-gravity of each bin. For bins whose perimeter lies entirely within phase space, this point is simply the center of the square bin. For bins on the edge of the dalitz plot, this point is not at the center of the bin.

The efficiency function is described in chapter 5.

7.9 The reduced χ^2

Because the fits are done simultaneously on the data and the Monte Carlo, the total χ^2 is due to both sources. The best χ^2 fit to the Monte Carlo alone gives $\chi^2 = 438$, for 490 bins with 36 free parameters, or a reduced $\chi^2/N = 0.96$. To get the χ^2 due to the data alone, we subtract the expected contribution from the efficiency. Since the 36 efficiency parameters are shared between the data and the efficiency fit, we divide this count by 2, and then subtract from the number of bins to arrive at the expected contribution due to the efficiency alone, $490 - 36/2 = 472$. The degrees of freedom of the fit include all the dynamic parameters and half of the efficiency parameters, since again the later are shared with the pure efficiency fit.

$$\chi^2/N_{\text{dof}} = \frac{\chi^2 - 472}{472 - N_{\text{par}}} \quad (7.31)$$

where N_{par} are the number of free parameters in the theoretical dynamic function.

7.10 Results

The Dalitz plot has one obvious resonance, the $K^*(892)$, appearing as a horizontal and vertical band. Thus this resonance is in all fits. The other resonances are not so immediately evident, and we must develop an algorithm to discover the remaining resonances. First, we examine the $K\pi$ wave, then we examine the $K\bar{K}$ wave. For reference, for a fit to the data assuming a “phase space” hypothesis, that is the dynamical function

Resonance	Mass [MeV/c ²]	Width [MeV/c ²]
$K^*(892)^\pm$	891.921	54.7
$K^*(892)^0$	896.056	53.4
$K_0^*(1430)$	1342	400
$a_0(980)$	999	353,353 *
$a_0(1450)$	1489	265
$a_2(1320)$	1318.1	107
$\rho(1450)$	1430	170
$\rho(1700)$	1740	190

Table 7.4: The reference masses and widths of fit #81, taken from [4].

Fit	χ^2	χ^2/N_{dof}	$K^*(892)$	$K_2^*(1430)$	$K_0^*(1430)$	$K^*(1410)$
0/201	994	1.29	•	•	•	•
1/81	1032	1.34	•	•	•	
2/156	1112	1.53	•	•		
3/80	1290	1.91	•		•	
4/159	1547	2.45	•			
5/157	12800	28.7		•	•	
6/160	13000	28.8		•		
7/161	13300	29.1			•	

Table 7.5: The components of the $K\pi$ wave. See figure 7.8

is simply a constant, the $\chi^2 = 23924$ for 489 degrees of freedom, or a reduced $\chi^2/N_{\text{dof}} = 49$. This number is meant to set a scale for a “bad” fit, compared to 1.0 being a “good” fit.

We also attempted a fit without any interferences between the different resonances. This gave a totally unacceptable fit of $\chi^2/N \sim 10$; allowing some interference between the $K\bar{K}$ components improved the fit to a still unacceptable $\chi^2/N \sim 5$. Thus the interferences between the $K\pi$ and $K\bar{K}$ waves are a critical ingredient in the Dalitz plot. This also means that it is difficult to determine the branching ratios of individual components because there is so much interference.

For comparison purposes, the fits in table 7.5 were done with all masses and widths fixed to those of table 7.4, and the $K\bar{K}$ wave included all five resonances: $a_0(980)$, $a_2(1320)$, $a_0(1450)$, $\rho(1450)$, $\rho(1700)$. The fits in table 7.6 were done with all masses and widths free, except for those of the $K_0^*(1430)$ and $K_2^*(1430)$, and the $K\pi$ wave included all three resonances, $K^*(892)$, $K_2^*(1430)$ and $K_0^*(1430)$.

7.10.1 Standard Fit

The reference fit is fit # 81 in table 7.5 with a reduced $\chi^2/N = 1.34$. Releasing the masses and widths improves the fit to $\chi^2/N = 1.22$, in fit #144. The Dalitz plot of the theoretical fit and the projections of the Dalitz plot are shown in figure 7.10. The fit quality is visually excellent. The χ^2 plot, showing areas of bad fit, is given in figure 7.13.

Because the angular decay distributions of the 1P_1 and 3P_1 initial states are exactly the same for each final state, we use only 1P_1 in the fit for computational and convergence reasons. However, if the relative productions of each isobar is different from these two initial states, then there can be a net difference between 1P_1 and 3P_1 , but only due to the *interferences* between the isobars.

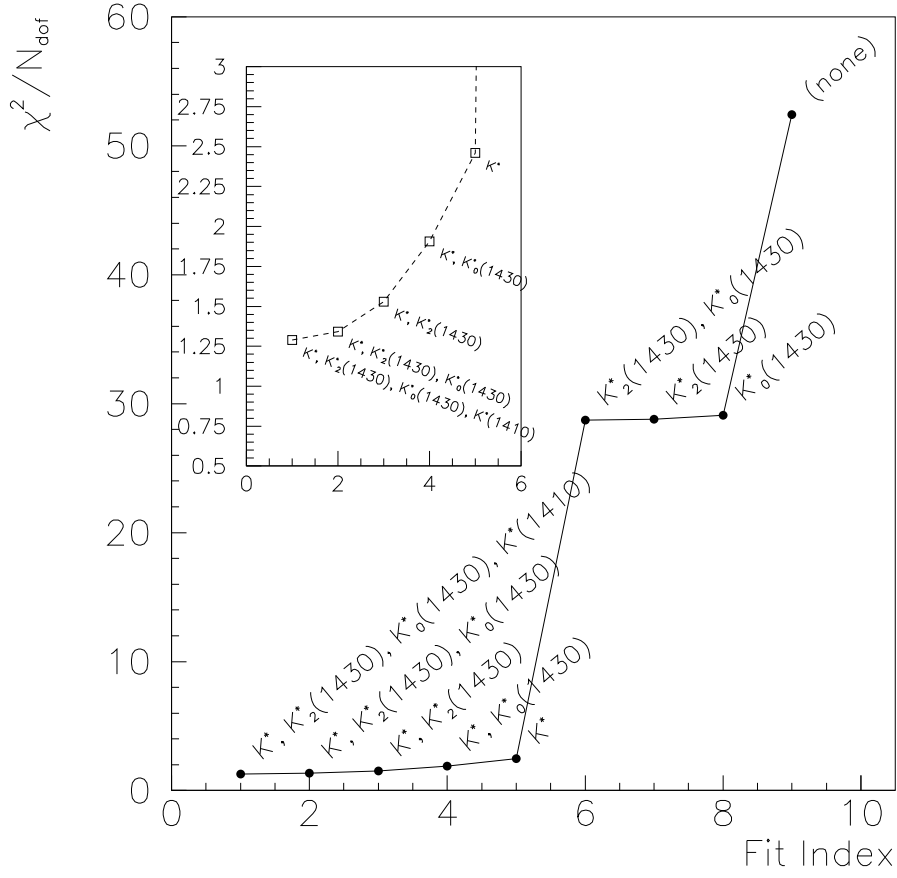


Figure 7.8: The fits of the $K\pi$ wave. See table 7.5

Fit	-LL	$a_0(980)$		$a_2(1320)$		$a_0(1450)$		$\rho(1450)$		$\rho(1700)$	
		m MeV/ c^2	$\begin{pmatrix} g_{K\bar{K}} \\ g_{\eta\pi} \end{pmatrix}$ MeV/ c^2	m MeV/ c^2	Γ MeV/ \hbar	m MeV/ c^2	Γ MeV/ \hbar	m MeV/ c^2	Γ MeV/ \hbar	m MeV/ c^2	Γ MeV/ \hbar
1/144	961	1004 ± 2	$\begin{pmatrix} 396 \pm 55 \\ 1.5 \pm 61 \end{pmatrix}$	1308 ± 3	112 ± 6	1488 ± 14	144 ± 30	1478 ± 17	277 ± 29	1701 ± 13	225 ± 24
2/145	973			1309 ± 3	109 ± 7	1481 ± 13	132 ± 30	1488 ± 17	258 ± 33	1705 ± 16	231 ± 31
3/89	974	1023 ± 21	$\begin{pmatrix} 300 \pm 80 \\ 480 \pm 60 \end{pmatrix}$	1308 ± 3	102 ± 7			1438 ± 24	222 ± 26	1668 ± 15	177 ± 20
4/141	987	919 ± 22	$\begin{pmatrix} 73 \pm 8 \\ 0.1 \pm 440 \end{pmatrix}$	1312 ± 3	112 ± 8	1472 ± 15	204 ± 40			1624 ± 7	140 ± 14
5/146	997			1308 ± 3	105 ± 6			1452 ± 18	203 ± 24	1669 ± 13	179 ± 22
6/147	1000			1314 ± 3	107 ± 7	1491 ± 12	122 ± 27			1634 ± 10	174 ± 21
7/96	1025	1042 ± 13	$\begin{pmatrix} 683 \pm 75 \\ 11 \pm 307 \end{pmatrix}$	1311 ± 3	106 ± 6					1625 ± 6	176 ± 15
8/148	1048			1315 ± 3	109 ± 6					1633 ± 9	226 ± 30
9/155	1190			1304 ± 3	98 ± 6	1553 ± 12	258 ± 21				
10/151	1364			1302 ± 3	83 ± 6						
11/149	1471							1319 ± 5	88 ± 7		
12/152	1725					1593 ± 7	182 ± 13				
13/150	1924										
PDG		983.4 ± 0.9	n/a	1318.1 ± 0.6	107 ± 5	1474 ± 19	265 ± 13	1465 ± 25	310 ± 60	1700 ± 20	240 ± 60

Table 7.6: The components of the $K\bar{K}$ wave. Blank entries mean that that resonance was not used in the fit. See figure 7.9.

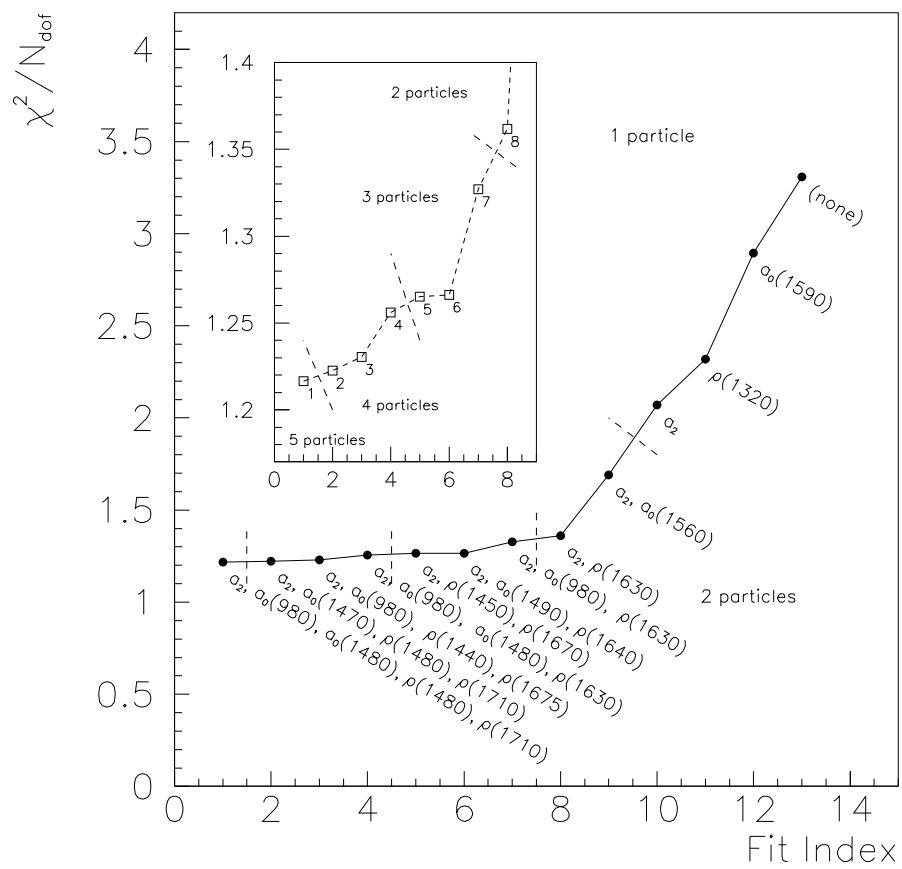


Figure 7.9: A graphical display of table 7.6.

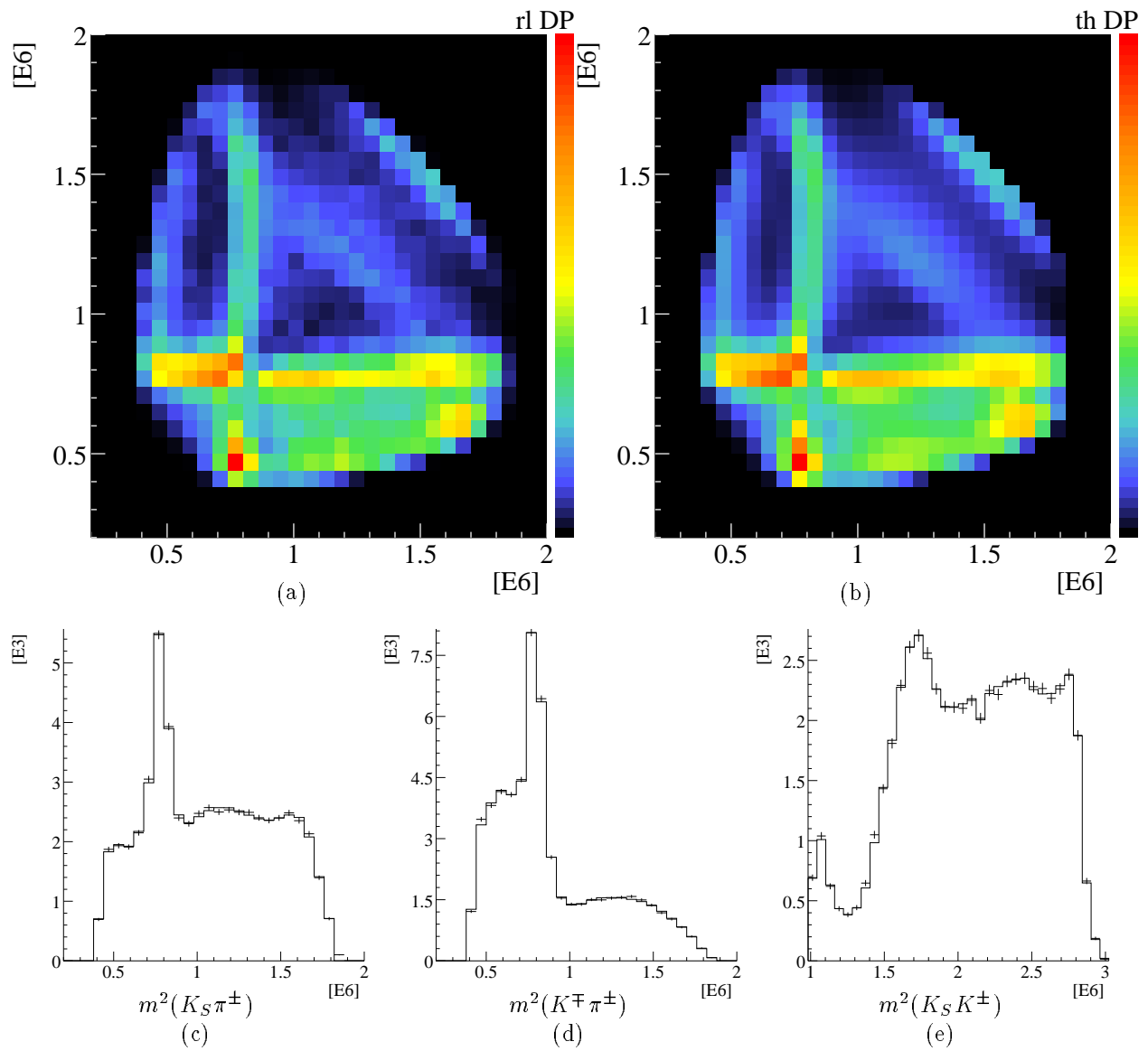


Figure 7.10: Fit 144, the standard fit. (a) Data Dalitz plot, (b) Fitted Dalitz plot, (c,d,e) The projections of the Dalitz plot. The solid line is the fitted function and the error bars are the data.

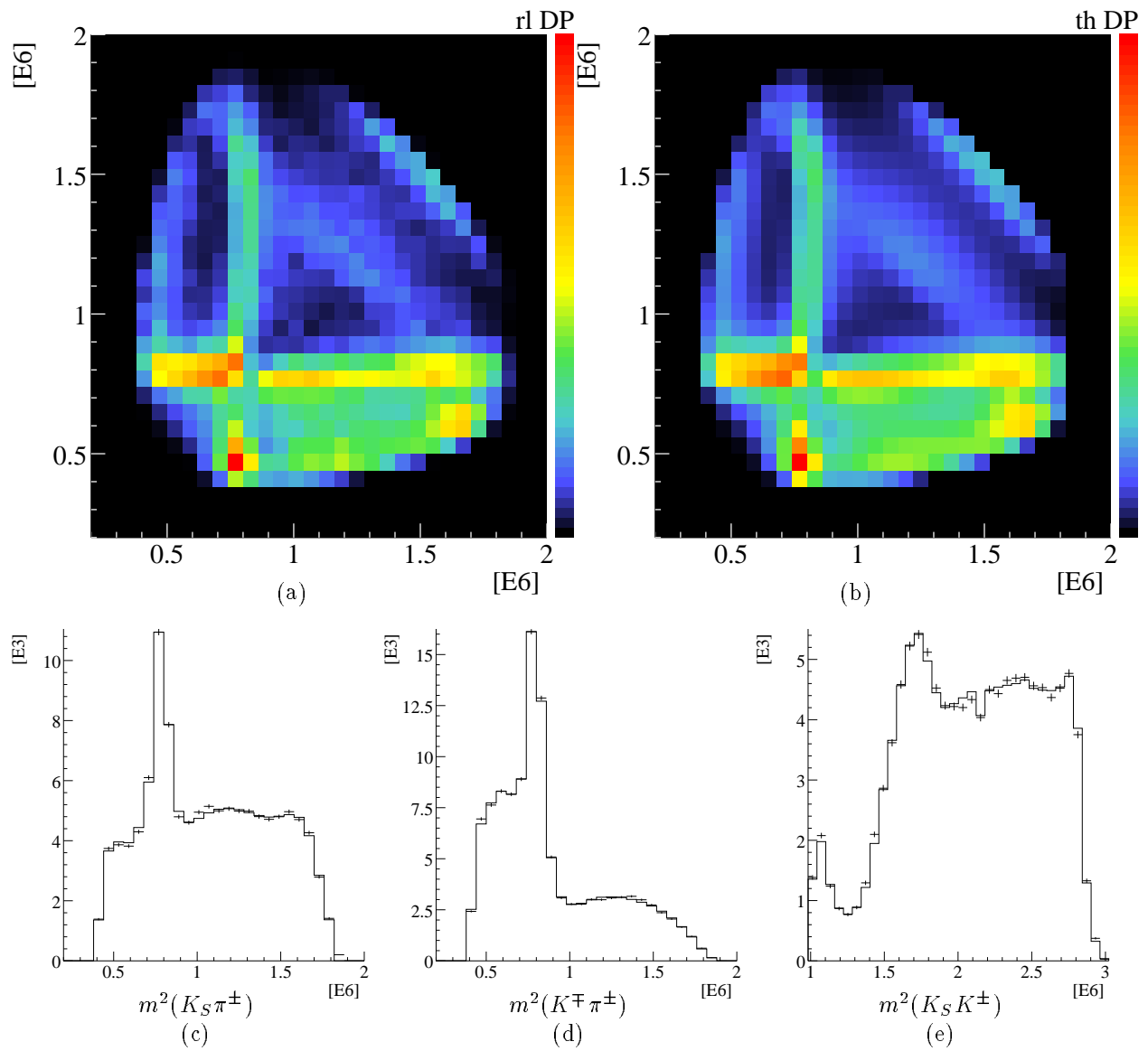


Figure 7.11: Fit 148, the minimal fit. (a) Data Dalitz plot, (b) Fitted Dalitz plot, (c,d,e) The projections of the Dalitz plot. The solid line is the fitted function and the error bars are the data.

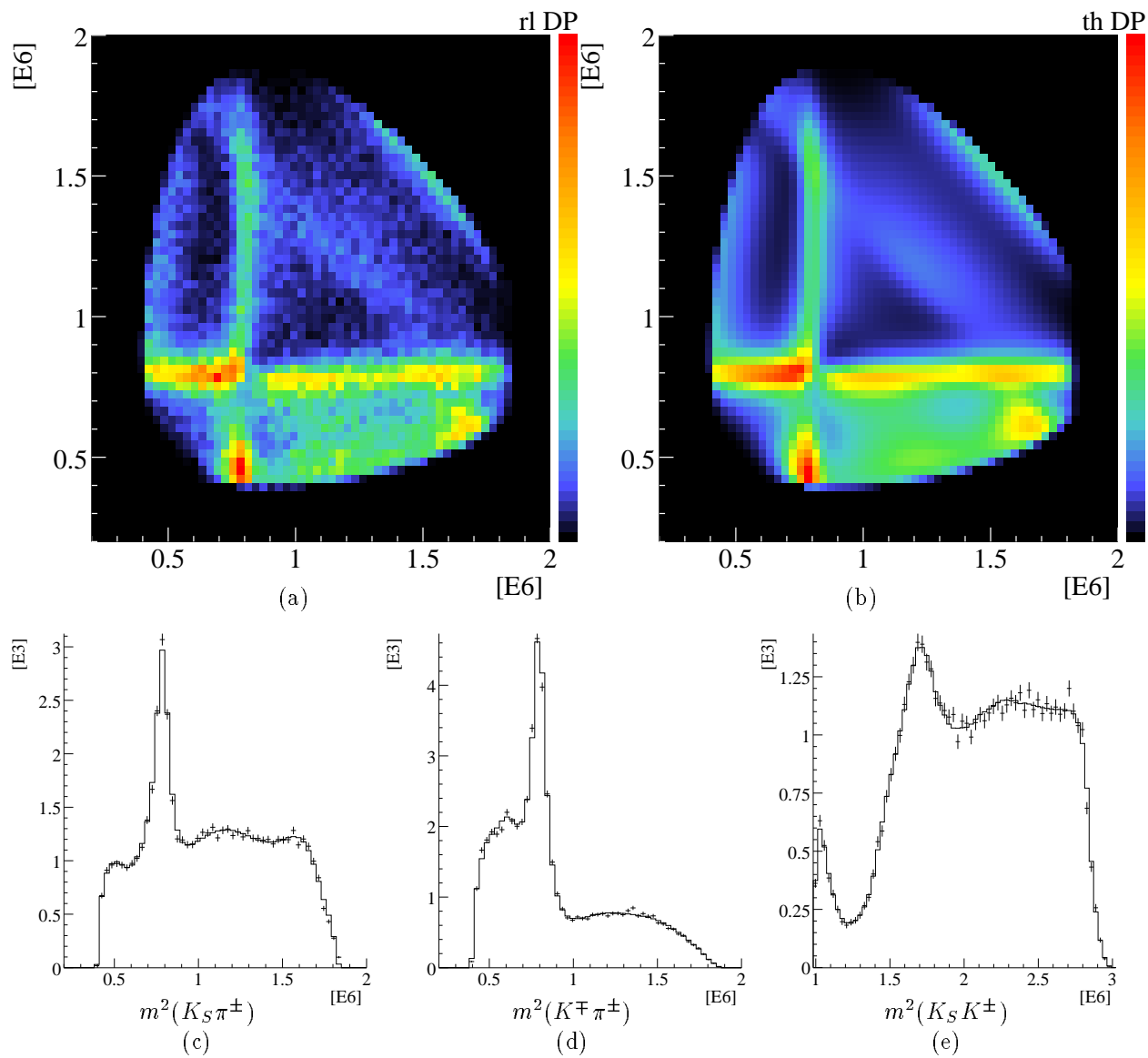


Figure 7.12: Fit 123, the fit without the $a_0(980)$ on a fine grid. (a) Data Dalitz plot, (b) Fitted Dalitz plot, (c,d,e) The projections of the Dalitz plot. The solid line is the fitted function and the error bars are the data.

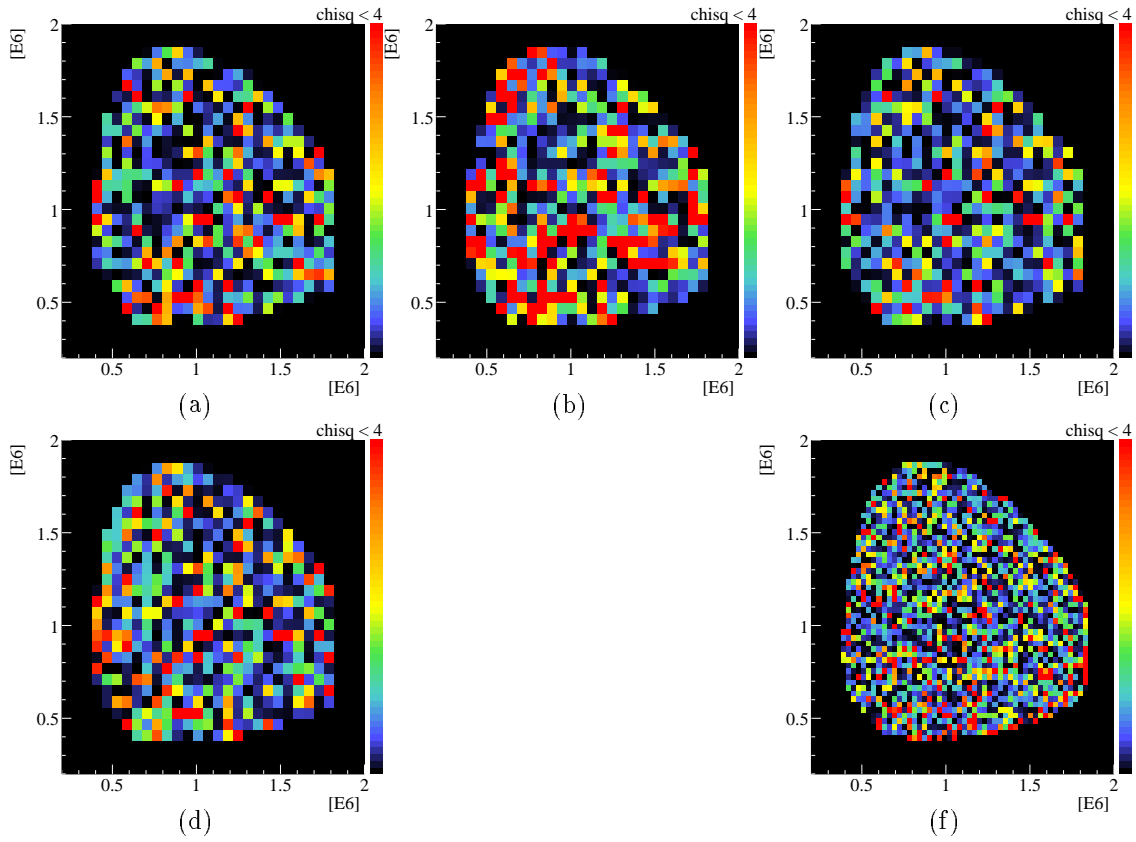


Figure 7.13: The χ^2 plot for (a) the standard fit # 81, (b) fit #87 with no P -wave or $K_2^*(1430)$, (c) the standard fit # 144, (d) the minimal fit # 148, (e) fit #123, without any $a_0(980)$ on a fine grid. Values of $\chi^2 > 4.0$ are truncated to 4.0, shown in red.

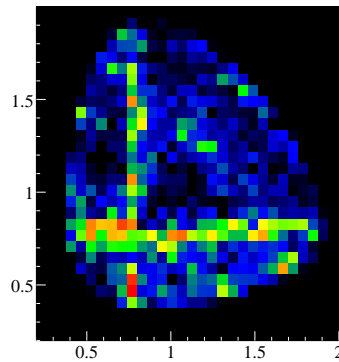


Figure 7.14: The $K_S K^\pm \pi^\pm$ Dalitz plot, taken at the Saclay 81 cm bubble chamber in the 1960's [31]. The data is not acceptance corrected, but the acceptance is nearly flat for the bubble chamber. The units of the axes are GeV^2/c^4

Chapter 8

Discussion

8.1 Systematic errors

8.1.1 Masses and widths

For the masses of resonances, we assign 2 MeV of systematic error based on the comparison of the $K^*(892)$ mass in section 8.2.1. For the widths, we subtract 30 MeV in quadrature from the fitted widths and assign 8 MeV of systematic error, also based on the result for the $K^*(892)$.

8.1.2 Goodness of fit

The best fit (fit #144) to the data has $\chi^2/N = (961 - 472)/(490 - 88) = 1.22$. An ideal fit would have given a reduced $\chi^2/N = 1$, so this fit is still not ideal. A toy Monte Carlo fit (see next subsection) shows that a fit to ideal data does indeed return a reduced $\chi^2/N = 1.0$. The additional χ^2 in our best fit should be due to one of the following reasons:

1. There is something wrong with the data, i.e. a background that has not been subtracted.
2. There is another isobar that needs to be put in the fit.
3. The isobar model has limited accuracy.
4. The detector resolution is not convoluted with the theoretical shape.
5. The theoretical intensity is not adequately linear across a single bin, so there is a second order error induced when the intensity is only calculated at the center of the bin.

We have attempted to eliminate item 1, by the careful checking of the data. We do not see any obvious clustering of the χ^2 across the Dalitz plot, so there doesn't seem to be any localized background.

Item 2 is unlikely, because we have tried all well known resonances and the incremental improvement in the fit is small, indicating that adding more resonances is not going to help the fit.

Item 3 is a definite possibility. The isobar model does not take into account final state interactions. There are limitations to the accuracy of the Breit-Wigners used, especially in the width characterization.

Item 4 should only apply to the narrow $K^*(892)$ and its interferences, but because this isobar is strong, it could account for a large part of the additional χ^2 . We have noted that some of the detector resolution is compensated for by the widening of the $K^*(892)$. However, this is not equivalent to detector resolution convolution, because widening the physical width changes the interference with other resonances, while simple Gaussian blurring does not. It is not a big effect, since the fitted width is only 8 MeV larger than the physical width.

Item 5 can be addressed by smaller binning. We have repeated the fit using a smaller binning, with bins of size $(0.03 \text{ MeV}^2/c^4)^2$ instead of $(0.06 \text{ MeV}^2/c^4)^2$ which were used in all the other fits. The result is $\chi^2/N = (2645 - 472)/(1924 - 88) = 1.18$, which is indeed better than the coarse binned fit. The fine binning is computationally expensive, so we could not use this for all the fits and scans. If we naively interpolate to zero bin size, we still are left with a $\chi^2/N \sim 1.14$.

In our opinion, the poor fit is due primarily to the limitation of the isobar model and the parameterization of broad resonances. We note that other Crystal Barrel analyses have similarly high χ^2/N with similar statistics to this analysis of 57 Kevents, with Abele[2] having a final fit of $\chi^2/N = 1.32$ with 37 Kevents, Aker[7] having $\chi^2/N = 1.27$ with 55 Kevents, Amsler[10] having $\chi^2/N = 1.15$ with 22.5 Kevents.

8.1.3 Toy Monte Carlo and branching ratios

To test the reproducibility of the fit, we took the theoretical Dalitz plot of standard fit #81, smeared each bin using a Poisson distribution, and refit the smeared theoretical data. The χ^2 before minimization was 418 for 417 degrees of freedom, which is exactly what it should be since that was what was generated. This proves that the χ^2 is correctly calculated and that it can be used as a goodness of fit estimate. However, the χ^2 could be further minimized considerably. Holding the efficiency function fixed, the fit found $\chi^2/N = 373/417 = 0.89$, or a change of 45 units of χ^2 .

Since we know what ingredients went into the fit, we can see how well the fit extracts those values. In table 8.1, we show the generated (input) Dalitz plot contributions and the fitted (output) Dalitz plot contributions.

It is clear that it is difficult to accurately measure the branching ratios when there are so many interfering amplitudes. We estimate the error for the total branching ratios (summed over initial states), is about 25%. The errors for the branching ratios of individual initial states is realistically about 50%.

In order to get a better constraint on the branching ratios, we have tried an additional symmetry, described in section 8.2.4.

8.2 The $K\pi$ wave

8.2.1 The $K\pi$ wave: The strange vector $K^*(892)$

The strange vector $K^*(892)$ is the most important resonance in this analysis. In a fit with all resonances *except* the $K^*(892)$ gives a humorous $\chi^2/N \sim 29$; that the $K^*(892)$ exists is obvious by inspection of the Dalitz plot.

The $p\bar{p}$ annihilation branching ratio is determined to be (see table 8.2)

$$\text{BR}(p\bar{p} \rightarrow K\bar{K}^*(892)) = (4.4 \pm 0.3) \times 10^{-3} \quad (8.1)$$

when the interference at the band crossing is assumed to integrate to zero. We compare this to Conforto[31], again assuming the interference between $I=0$ and $I=1$ integrates to zero, which found $\text{BR}(p\bar{p} \rightarrow K\bar{K}^*(892)) = (3.5 \pm 0.3) \times 10^{-3}$. This is somewhat smaller, but may be due to the following reasons. The bubble chamber analysis assumed no P -wave annihilation, but we see that $\sim 30\%$ of our branching ratio comes from P -wave. This will change the interference pattern significantly. Also, the $K^*(892)$ was parameterized via $I = 0$ and $I = 1$ in the previous analysis, while it was parameterized via horizontal and vertical bands in our analysis. There is a clear strong interference effect at the crossing of the bands, which may explain the difference in branching ratios if the integrated interference is not zero.

From the best fit (#144) with the masses and widths of all resonances freely varying in the fit (except the broad K_2^* and K_0^*), we find (quoting statistical errors only)

$$\begin{aligned} m(K^*(892)^\pm) &= 890.0 \pm 0.8 & \Gamma(K^*(892)^\pm) &= 56 \pm 2 \\ m(K^*(892)^0) &= 894.0 \pm 0.6 & \Gamma(K^*(892)^0) &= 60 \pm 2. \end{aligned} \quad (8.2)$$

The Particle Data Group[36] reports the mass and width of the $K^*(892)$ as $m(K^*(892)^\pm) = 891.66 \pm 0.26$ MeV/ c^2 , $m(K^*(892)^0) = 896.10 \pm 0.28$ MeV/ c^2 and $\Gamma(K^*(892)) = 50.6 \pm 0.5$ MeV/ c^2 (charge independent).

Our measurements of masses are 1.7 and 2.1 MeV/ c^2 lower, respectively, in the masses. The mass difference is not surprising, because the binning in the histogram is rather coarse, (0.06 GeV²/ c^4), which corresponds to a mass range of $\delta m \sim 33$ MeV/ c^2 at the $K^*(892)$ mass. Because the theoretical intensity is calculated only at the center of a bin, there is a significant undersampling of the theoretical shape over a single bin. But rather than assign a $\pm 33/2$ MeV/ c^2 error to the result, we see that the systematic error of the coarse binning is only about ± 2 MeV/ c^2 . This testifies to the influence of the K^* on the entire Dalitz plot far beyond the narrow peak region. We assign a systematic error of 2 MeV/ c^2 in mass to all other mass measurements.

$^{2s+1}L_J$	Isobar	% of Dalitz plot		Change	
		Before Fit	After Fit	Relative	Absolute
1S_0	$K^*(892)^\pm K^\mp$	4.2	4.0	-5%	-0.2
	$K^*(892)^0 K^0$	6.9	5.8	-16%	-1.1
	$K_0^*(1430)^\pm K^\mp$	0.2	1.4	+500%	+1.2
	$K_0^*(1430)^0 K^0$	6.3	5.0	-21%	-1.3
	$a_0(980)\pi$	1.4	0.9	-36%	-0.5
	$a_0(1450)\pi$	0.9	1.1	+22%	+0.2
	$a_2(1320)\pi$	22.8	22.2	-3%	-0.6
	$\rho\pi$	9.5	7.1	-25%	-1.4
	$K_2^*(1430)^\pm K^\mp$	1.6	1.7	+6%	+0.1
	$K_2^*(1430)^0 K^0$	7.2	6.9	-4%	-0.3
	3S_1	$K^*(892)^\pm K^\mp$	14.8	15.9	+7%
$K^*(892)^0 K^0$		11.8	12.3	+4%	+0.5
$a_2(1320)\pi$		2.2	1.9	-14%	-0.3
$\rho\pi$		2.6	2.8	+8%	+0.2
$K_2^*(1430)^\pm K^\mp$		1.6	1.7	+6%	+0.1
$K_2^*(1430)^0 K^0$		0.4	0.7	+75%	+0.3
1P_1	$K^*(892)^\pm K^\mp$	1.4	2.0	+43%	+0.6
3P_1	$K^*(892)^0 K^0$	9.1	10.8	+13%	+1.7
	$K_0^*(1430)^\pm K^\mp$	17.3	19.6	-3%	-2.3
	$K_0^*(1430)^0 K^0$	6.9	4.3	-38%	-2.6
	$a_0(980)\pi$	5.7	4.8	-16%	-0.9
	$a_0(1450)\pi$	0.2	0.1	-50%	-0.1
	$a_2(1320)\pi$	0.5	1.1	+120%	+0.6
	$\rho\pi$	17.8	21.5	+21%	+3.7
	$K_2^*(1430)^\pm K^\mp$	1.6	1.2	-25%	-0.4
	$K_2^*(1430)^0 K^0$	1.4	2.5	+79%	+1.1
	Sum	$K^*(892)^\pm K^\mp$	20.4	21.9	+4%
$K^*(892)^0 K^0$		27.8	28.9	+4%	+1.1
$K_0^*(1430)^\pm K^\mp$		17.5	21.0	+20%	+3.5
$K_0^*(1430)^0 K^0$		13.2	9.3	-30%	-3.9
$a_0(980)\pi$		7.1	5.7	-20%	-1.4
$a_0(1450)\pi$		1.1	1.2	+9%	+0.1
$a_2(1320)\pi$		25.5	25.2	-1%	-0.3
$\rho\pi$		29.9	31.4	+5%	+1.5
$K_2^*(1430)^\pm K^\mp$		4.8	4.6	-4%	-0.2
$K_2^*(1430)^0 K^0$		9.0	10.1	+12%	+1.1

Table 8.1: The Toy MC, before and after fitting

The measured width is about 8 MeV higher than the Particle Data Group's value, and this is simply a result of the fact that the theoretical intensity is not convoluted with the detector resolution. Doing so requires an inordinate amount of computational time, and we can see that the error is only 8 MeV for the narrowest resonances, so the effect is even smaller for all the other much wider resonances. The 8 MeV net difference implies a detector resolution of $\sqrt{58^2 - 50^2} \sim 30\text{ MeV}$, which is about 3% of the K^* mass. We thus subtract (in quadrature) 30 MeV from all fitted widths to remove the detector resolution, and assign 8 MeV of systematic error to all measured widths.

We attempted adding a second pole to the strange vector wave, the $K^*(1410)$ with a mass of $1414\text{ MeV}/c^2$ and a width of $232\text{ MeV}/c^2$. The χ^2 dropped by 37 with 12 extra free parameters, meaning that this is a $\sqrt{37-12} = 5\sigma$ effect. Because this particle is well established by the Particle Data Group, this result is not surprising. However, the additional calculational overhead has meant that we refrained from using it in other fits.

8.2.2 The $K\pi$ wave: The strange tensor $K_2^*(1430)$

To our knowledge, the $K_2^*(1430)$ has not been used before in any $p\bar{p} \rightarrow KK\pi$ (at rest) analysis. This is due, presumably, because the mass of $1430\text{ MeV}/c^2$ is higher than the edge of the Dalitz plot, $1240\text{ MeV}/c^2$ and its width of $100\text{ MeV}/c^2$ seems narrow. However, the tails of a Breit-Wigner are very long and do not drop rapidly after going beyond one standard width. Of course to be significant, the resonance needs to be very strong so that the tails have any significant intensity.

The LASS spectrometer at SLAC[18] studied $K\pi$ scattering at energies from threshold to 4 GeV. They noted two very strong resonances, the $K^*(892)$ and the $K_2^*(1430)$, as well as the next three higher excited ($L = 3, 4, 5$) states of the K^* . The $K^-\pi^+$ invariant mass distribution is shown in figure 8.1a. The height of the $K^*(892)$ and $K_2^*(1430)$ peaks are in a ratio of 1:0.63, while the ratio of widths is 50.8:116.5. This means that the ratio of events due to the tensor to events due to the vector is about 1.44; in other words, the tensor intensity is *greater* than the vector; since the vector is the most visible component of the Dalitz plot, the tensor *must* have a significant contribution, even though the mean lies outside of phase space.

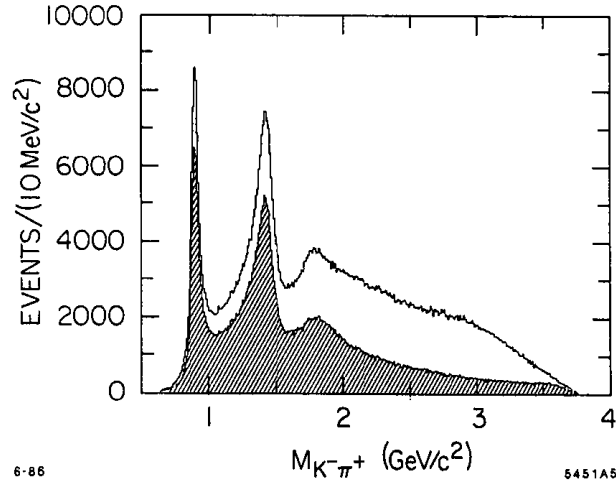
The actual contribution of the tensor in the $p\bar{p} \rightarrow KK\pi$ Dalitz plot is smaller than the vector, of course, because it is outside of phase space and along the edge of phase space, the angular momentum barrier causes production of $p\bar{p} \rightarrow KK_2^*(1430)$ to be suppressed. This is why the $K_2^*(1430)$ is not immediately obvious by eye in the Dalitz plot as vertical and horizontal bands. However, there are visible effects that are due to interference effects of the $K_2^*(1430)$ with other resonances in the Dalitz plot, for example the KK threshold enhancement in the upper-right part of the Dalitz plot, which is discussed below.

However, we can remove the phase space restriction and angular barrier from the partial-wave analysis and simply plot the Breit-Wigners of the $K^*(892)$ and $K_2^*(1430)$ using the production amplitudes. We can then compare this plot with the LASS data which is essentially not limited by phase space or angular momentum. The plot of

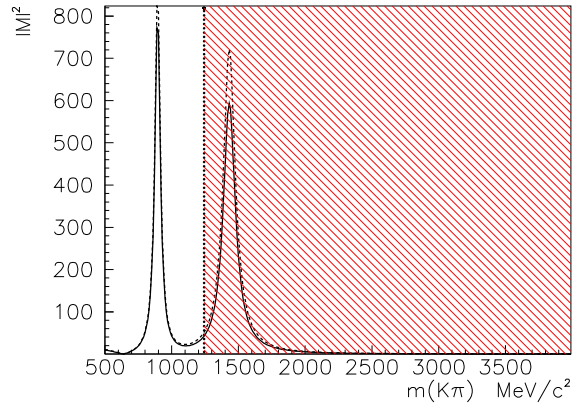
$$|M(m)|^2 = \sum_{i=^1S_0, ^3S_1, (^1P_1 \text{ and } ^3P_1)} \left| \beta_i^{K^*(892)} BW^{K^*(892)}(m) + \beta_i^{K_2^*(1430)} BW^{K_2^*(1430)}(m) \right|^2 \quad (8.3)$$

is shown in figure 8.1b, where β_i is the fitted production amplitude in the i -th initial state (taken from fit #130), $BW(m)$ is the relativistic Breit-Wigner used in the PWA, and m is the invariant mass of the $K\pi$ system. The dashed line is drawn with all the $\beta_i^{K_2^*(1430)}$ set to their $+1\sigma$ upper limits, while the solid line is drawn with all the $\beta_i^{K_2^*(1430)}$ set to their -1σ lower limits. The ratio of peak heights [$K^*(892) : K_2^*(1430)$] is 0.83 ± 0.12 , which is in reasonable agreement with the LASS data, which found a ratio of 0.63 ± 0.03 . Note that our fit is only sensitive to the region *within* phase space ($m(K\pi) < 1242\text{ MeV}/c^2$), which is the unhatched region in the figure. The peak height ratio agreement is amazing since it is extrapolated from just the small portion within phase space.

The χ^2/N drops from 1.91 to 1.34 when the $K_2^*(1430)$ is introduced (compare fit #80 and #81 in table 7.5). In fact, the tensor $K_2^*(1430)$ is more important than the scalar $K_0^*(1430)$, as seen in the table. This, in addition to excellent agreement with the LASS $K\pi$ scattering data, proves that the $K_2^*(1430)$ is vital in a description of the $KK\pi$ system at rest.



(a)



(b)

Figure 8.1: (a) the $K\pi$ invariant mass distribution seen in the LASS experiment (taken from [18], figure 3), for events with $|t'| \leq 1.0 \text{ GeV}/c^2$. The shaded region contains events with $n\pi^+$ mass greater than $1.7 \text{ GeV}/c^2$ (the difference between the shaded and unshaded regions is unimportant for the purposes of this comparison). (b) the fitted $K\pi$ invariant mass distribution as seen in this analysis, when phase space and angular barrier functions are *not* included. The two curves are the $\pm 1\sigma$ limits of the fitted values. The hatched region is outside of the $KK\pi$ at-rest phase space.

8.2.3 The $K\pi$ wave: The scalar $K_0^*(1430)$

The $K_0^*(1430)$ resonance (with the additional background term) is not as significant as the $K^*(892)$ or the $K_2^*(1430)$. This can be expected from the results of the LASS experiment[18] which saw much more evidence for the later two resonances than this scalar. However, the fit is still significantly improved by including this resonance, by dropping the χ^2/N from 1.53 (fit # 156) to 1.34 (fit# 81) in table 7.5.

8.2.4 Ratio of charged to neutral strange resonances

As can be seen by scanning table 8.1, the percentage attributed to charged or neutral ($K\pi$) resonances seems to vary in a random pattern. In some cases the intensity of the charged resonance exceeds that of the neutral resonance, and in other cases, the reverse is true. This variation changes from fit to fit.

We have hypothesized that there may be an additional constraint we can impose in the fit. We have imposed a fixed ratio on the production amplitudes of the neutral $K\pi$ waves to the charged $K\pi$ waves. This ratio was then allowed to vary. This removes 8 degrees of freedom (now all the $(K\pi)^\pm$ and $(K\pi)^0$ waves are in a fixed ratio), and added one (the ratio). The phase of each production amplitude is still a free parameter in the fit.

The result of the fit # 202 (see table 8.2 for the full results) is an intensity ratio

$$\left| \frac{\beta[(K\pi)^0]}{\beta[(K\pi)^\pm]} \right|^2 = 1.39 \pm 0.14. \quad (8.4)$$

The χ^2 increases by 17 units after the removal of 7 parameters, so the significance of this is $\sqrt{17-7} \sim 3\sigma$. Because the branching ratios from each initial state vary considerably if this constraint is not imposed, we use this fit to give the values of the branching ratios, in table 8.2.

Conforto[31] found a charge asymmetry of $(500 \pm 50) : (300 \pm 30) = 1.67 \pm 0.24$ between $K^{*0}(892)K^0$ and $K^{*\pm}(892)K^\mp$. Our result is consistent with this, even though we have introduced P -wave, the tensor $K_2^*(1430)$ and the $a_0(1450)$.

8.3 The $K\bar{K}$ wave

There are five candidate resonances in the $K\bar{K}$ wave, which are given in the heading of table 7.6. To determine which of these particles is required requires testing all combinations. The table gives nearly all combinations of 0,1,2,3,4 or 5 resonances; because the $a_2(1320)$ is clearly needed, some combinations without the $a_2(1320)$ are omitted for clarity. The fits are sorted in order of increasing χ^2 . In all fits, the masses and widths of the $K\bar{K}$ resonances were allowed to vary freely, in addition to the masses and widths of the $K^*(892)^\pm$ and $K^*(892)^0$. The remaining resonances: $K_0^*(1430)$ and $K_2^*(1430)$ are too broad to allow to vary.

At the bottom of table 7.6 are the values from the Particle Data Group[36]. The g widths for the $a_0(980)$ are not applicable, because they are model dependent. The mass and width of the ρ 's are for their decays into non- $K\bar{K}$ channels. In the figure 7.9, the same data is displayed graphically, where the reduced χ^2 is displayed, as defined in (7.31).

In figure 7.9, one can clearly see that there is a knee in the χ^2 plot at fit #8/148, which requires simply two resonances, the $a_2(1320)$ and a $\rho(1630)$. This is our minimal fit, which is shown in figure 7.11. This fit is acceptable, with no clustering of χ^2 over the Dalitz plot (shown in figure 7.11), but further improvements can be made.

We first attempt to add one extra resonance, shown in fits #5, #6 and #7. There is not a significant difference between fit #5 (which added the $\rho(1450)$) and #6 (which added the $a_0(1450)$), but the improvement over fit #8 is significant. Adding both $a_0(1450)$ and $\rho(1450)$ simultaneously again improves the χ^2 in fit #2, favoring them over the $a_0(980)$ as the fourth particle. However, adding the $a_0(980)$ to the other four does not significantly change the χ^2 in fit #1. It is our opinion that while the $a_0(980)$ has been seen in decays to $\eta\pi$, the decay into $K\bar{K}$ could be much smaller than previously believed.

In defense of the $a_0(980)$ and its wild variations in mass and g couplings as seen in the table, the shape in this analysis is dictated primarily by the opening of phase space, and not the Flatté formula. The coupling $g_{K\bar{K}}$ is almost entirely independent of the data, so the values of -1 are not surprising. The coupling value essential gets absorbed into the production amplitude, so the sign of -1 reflects simply an arbitrary change of phase of the amplitude.

The $a_2(1650)$ resonance was attempted, but gave absolutely no improvement in the fit.

8.3.1 Is there an second isovector? Is there *any* isovector?

One of the main goals of this analysis is to find the isovector member of the $q\bar{q}$ scalar nonet. There are now three candidates for this position, the $a_0(980)$, the $a_0(1300)$ and the $a_0(1450)$. Because the $a_0(980)$ has other weird properties, many believe it is not the isovector member. The OBELIX favors the $a_0(1300)$ while the Crystal Barrel favors the $a_0(1450)$.

The first question is, is this isovector statistically significant? We attempt to answer this question in this section. The second question is why do we get a different result from OBELIX and from the previous Crystal Barrel analysis, the second question is, what are the pole parameters? We attempt to answer the first question in this section, and the second question in section 8.3.2.

Our fits offer the surprising conclusion that *there may not be any isovector contribution at all* to the $KK\pi$ Dalitz plot. The minimal fit requires only a $a_2(1320)$ and a single vector $\rho(1670)$ in the $K\bar{K}$ wave to get a reasonable reduced $\chi^2/N = 1.27$. Adding one particle to this favors another vector ρ over a scalar a_0 , with a change in $\delta\chi^2 = -51$ for 8 extra free parameters. The significance of this is $\sqrt{63-8} \sim 6.6\sigma$.

The (masses,widths) of these two ρ 's are $(1452 \pm 18, 204 \pm 24)$ and $(1669 \pm 13, 170 \pm 22)$ MeV/ c^2 , respectively, consistent with the Particle Data Group's values of $(1465 \pm 25, 310 \pm 60)$ and $(1700 \pm 20, 240 \pm 60)$ MeV/ c^2 , respectively. The change in χ^2 and confirmation by the PDG of the masses speaks for inclusion of two vector resonances in the $K\bar{K}$ wave. We emphasize the statement that the $K\bar{K}$ wave favors two vector ρ poles rather than one vector ρ pole and one scalar a_0 pole.

We then proceeded to add a scalar resonance (an a_0) and the fit found an improvement of $\delta\chi^2 = -25$ with 6 extra parameters. Thus the χ^2 drops by an additional 19 units over statistics alone, which is roughly a $\sqrt{19} = 4.4\sigma$ effect. The range of 3 to 5 σ 's is traditionally a gray area of acceptance, and this result is thus gray. The parameters for the mass are relatively stable (ranging from 1472 to 1488 MeV/ c^2 over fits 1-8 which returned a statistical error of about 10 MeV/ c^2) but the width is not stable, varying from 100 to 250 MeV/ c^2 with only a maximum change in χ^2 of 10, as can be seen in figure 8.3. In any case, here are the pole position parameters, the average of fits 1/144, 2/145, 4,/141 and 6/147 in table 7.6 followed by the corrections discussed in section 8.1.

$$m(a_0(1450)) = 1481 \pm 17 \text{ MeV}/c^2 \qquad \Gamma(a_0(1450)) = 100 \text{ to } 250 \text{ MeV}/c^2 \qquad (8.5)$$

The much heralded $a_0(980)$ is the weakest resonance in the entire Dalitz plot, with no statistical significance at all based on the change of χ^2 . The reduced χ^2/N (fit #144) is 1.216 with the $a_0(980)$ and 1.222 without. The raw χ^2 drops by 11 with the addition of 7 extra parameters, thus only $\delta\chi^2 = 4$ can be attributed to the significance of the $a_0(980)$. This change of 4 is about a 2 σ effect, assuming perfect statistics.

In the previous Crystal Barrel result, a fit with the double-pole ρ alone (not $a_0(1450)$) was not reported. The ρ poles were added to the fit after the $a_0(1450)$, thus it is not clear if the net improvement in the fit was due mostly due to the ρ poles *helping* the $a_0(1450)$ or *replacing* the $a_0(1450)$. In the OBELIX result, only a single pole ρ was used with the a_0 . However, we have shown that a two pole ρ is favored over a single pole ρ and a_0 .

We summarize in saying that the fit does not require any $a_0(980)$, but is consistent with an $a_0(1450)$ although it is not inconsistent either.

8.3.2 Where is the second isovector, $a_0(1450)$?

We now ask why this analysis, with a factor of 5-6 more statistics than either previous analysis, finds less statistic significance for the $a_0(1450)$ than they did. The answer is that the previous analyses did not use the $K_2^*(1430)$ in the fits. In this section, we will show that the inclusion of this tensor resonance affects the results of the $a_0(1450)$.

8.3.3 The Crystal Barrel Analysis of $K_L K^\pm \pi^\mp$

In Abele[4], the Crystal Barrel collaboration found evidence for a second isovector with $m = 1480 \pm 30$ MeV/ c^2 and $\Gamma = 265 \pm 15$ MeV/ c^2 . The analysis claimed that the mass was not very sensitive to the χ^2 , that the mass could be varied between 1450 and 1510 MeV/ c^2 with a maximum change in χ^2 of 20.

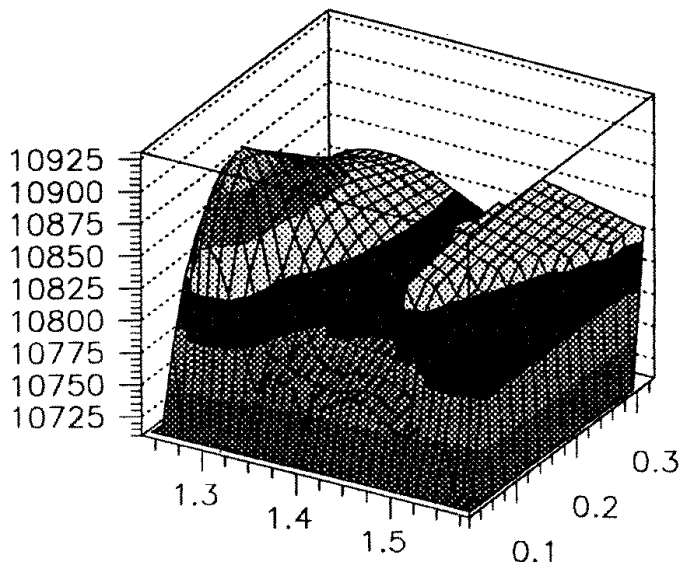


Figure 8.2: OBELIX: Likelihood scan over mass (1200→1600 MeV) and width (0→300 MeV) of second isovector, reproduced from OBELIX[23] (units are in GeV).

8.3.4 The OBELIX Analysis

The conclusion of the OBELIX collaboration in [23] is that there is a new isovector with $m = 1290 \pm 10$ MeV/ c^2 and $\Gamma = 80 \pm 5$ MeV/ \hbar , which they call the $a_0(1300)$. They note that this is not consistent with the Crystal Barrel result.

In order to disentangle this problem, the OBELIX analysis scanned the mass from 1200 to 1600 MeV/ c^2 and the width from 40 to 320 MeV/ c^2 of the isovector (see figure 8.2). They found two solutions. Solution 1 has $m_1 = 1290 \pm 10$ MeV, $\Gamma_1 = 90 \pm 10$ MeV, $LL_1 = 10910$, and solution 2 has $m_2 = 1480 \pm 40$, $\Gamma = 200 \pm 60$ MeV, $LL_2 = 10845$. They point out that solution one has a better Log-Likelihood and the shape of the likelihood curve is better behaved at solution 1. In their plot of the Log-Likelihood scan, there is a valley of about -100 LL between the two solutions.

We note that the shape of the second solution is not a good parabolic log-likelihood surface, but features a sharp discontinuity at 1480 MeV/ c^2 . We fear that this is not a physical maximum in the likelihood but a *gestalt* change in choice of solutions. We believe that this cliff in likelihood is an artifact of the direction of the scanning of mass (from small mass to large mass, rather than from large mass to small mass). This is demonstrated in figure 8.4 and 8.6.

8.3.5 Comparisons to $K_L K^\pm \pi^\mp$ and OBELIX

We have repeated the same mass and width scan for four different hypotheses. The first hypothesis includes P -wave annihilation and the $K_2^*(1430)$ in the fit. This scan is shown in figure 8.3. This hypothesis results in our best fit. The second hypothesis includes P -wave annihilation, but no $K_2^*(1430)$, which is the hypothesis used in the OBELIX analysis. This scan is shown in figure 8.4. The third hypothesis is the complement of the latter, with no P -wave annihilation but with $K_2^*(1430)$. This hypothesis was done for completeness, and is shown in figure 8.5. The fourth and final hypothesis contains no P -wave and no $K_2^*(1430)$, shown in figure 8.6. This is the hypothesis of the previous Crystal Barrel analysis.

The masses of all other resonances (which include $a_2(1320)$, $\rho(1630)$, $K^*(890)$, $K_2^*(1430)$ and $K_0^*(1430)$) were kept fixed. The $a_0(980)$ was not used in the fit with the $K_2^*(1430)$ and P -wave annihilation. The efficiency function was fixed to the best fit to just Monte Carlo data and not varied as in other fits for faster fitting. Because it was fixed, the absolute χ^2 's of these scans are somewhat higher and can not be compared to the fits in tables 7.5 and 7.6. Also, relative differences of less than ~ 50 units of χ^2 are not likely not to

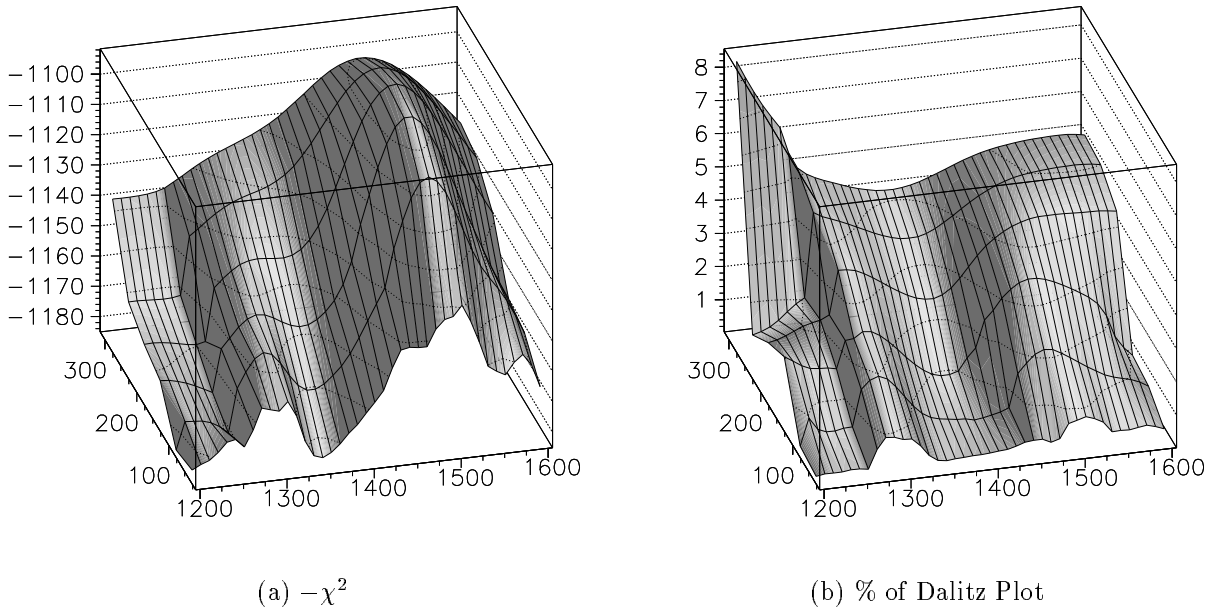


Figure 8.3: A scan over the mass and width of a second isovector, assuming P -wave annihilation and $K_2^*(1430)$ contributions. (a) $-\chi^2$ from this analysis (b) percentage of Dalitz plot due to isovector. Horizontal axes units are MeV/c^2 .

be statistically significant, as we see for the case of no P -wave and no $K_2^*(1430)$ at the end of this section.

In our scan including the $K_2^*(1430)$ and P -wave annihilation, we see one solution at $m = 1490 \pm 10 \text{ MeV}/c^2$ and $\Gamma = 240 \pm 50 \text{ MeV}/\hbar$. (We note that this is not our final solution of the mass and width, because the masses and widths of the other $K\bar{K}$ resonances were not allowed to vary. However, the pole position in this scanned solution is similar to that of our best fit). There is a ridge at $m = 1300 \pm 10$ at $\Gamma = 90 \text{ MeV}/c^2$, but the ridge disappears into the global maximum. If we examine the percentage of the isovector contribution to the Dalitz plot, we see that there is a two ridge structure, with one around $m = 1290 \text{ MeV}/c^2$ and one around $m = 1500 \text{ MeV}/c^2$.

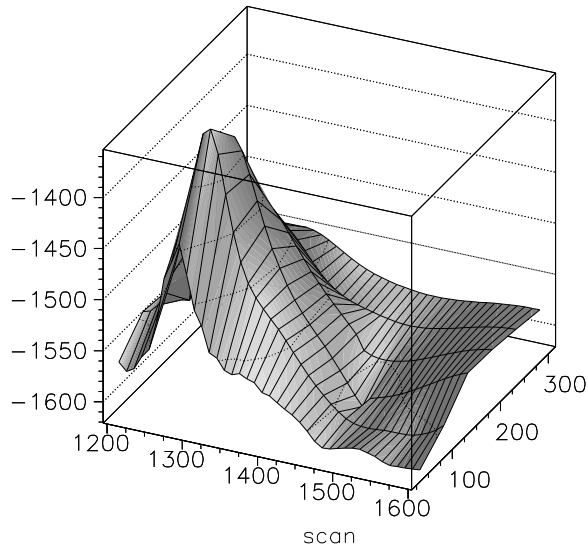
In our scan including the $K_2^*(1430)$ and but with no P -wave annihilation (figure 8.5), we see a very broad minimum in the χ^2 , roughly centered at $m = 1450 \text{ MeV}/c^2$ and $\Gamma = 190 \text{ MeV}/c^2$. This solution is consistent with the best fit, albeit the χ^2 is worse by +270.

In our scan which mimics the OBELIX analysis, using P -wave but no $K_2^*(1430)$, we get a very clear minimum of the χ^2 at $m = 1285 \pm 15 \text{ MeV}/c^2$ and $\Gamma = 90 \pm 20 \text{ MeV}/c^2$ (see figure 8.5). This is in perfect agreement with the OBELIX analysis. However, we do not see the secondary solution at $m = 1480$ that they report. We postulate in subsection 8.3.6 that the secondary solution in OBELIX is an artifact of the fit procedure, and not a physical minima.

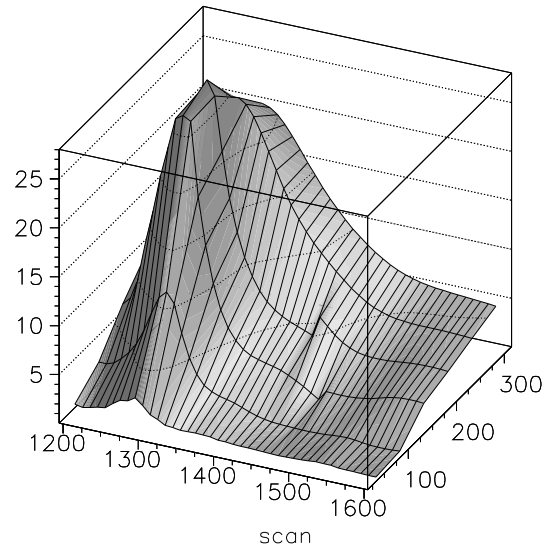
Finally, in our scan which mimics the previous Crystal Barrel analysis, using no P -wave annihilation and not any $K_2^*(1430)$, we get a first solution at $m = 1300 \pm 10 \text{ MeV}/c^2$ and $\Gamma = 90 \pm 20 \text{ MeV}/c^2$ at $\chi^2 = 2458$. There is second solution at $m = 1450 \text{ MeV}/c^2$ and $\Gamma = 240 \text{ MeV}/c^2$ with $\chi^2 = 2495$. The difference in these two solutions is 37, which is not very significant. In fact, we have repeated the fits at these two solution positions, except with a freely varying efficiency function. The results are $\chi_1^2 = 1954$ and $\chi_2^2 = 1863$, respectively; the second solution is now better than the first by $\delta\chi^2 = 91$.

8.3.6 Two solutions, One χ^2 Minimum

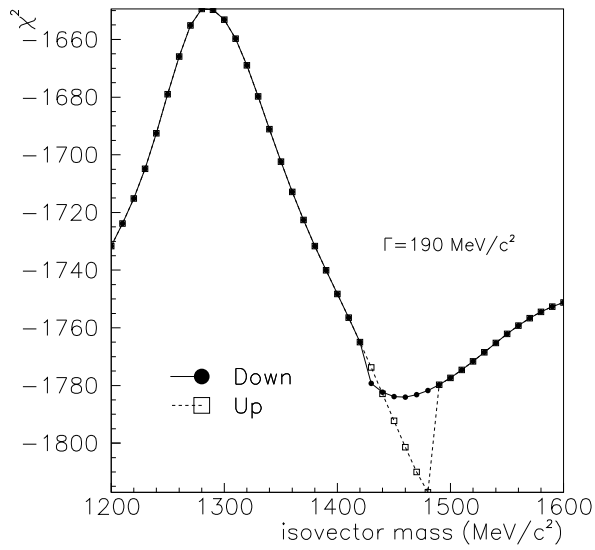
A local minimum in the χ^2 may be simply a manifestation of a discontinuity in the χ^2 surface, causing a “fake” local minimum. There may be two very different solutions to the fit, but which have similar χ^2 values. If the fit gets “caught” in one solution, it may not find the other solution because the χ^2 barrier between the two solutions is too high, even though the other solution may be a better solution. In a scan of a parameter,



(a) $-\chi^2$



(b) % of Dalitz Plot



(c)

Figure 8.4: A scan over the mass and width of a second isovector, assuming P -wave annihilation but no $K_2^*(1430)$ contributions. (a) $-\chi^2$ from this analysis (b) percentage of Dalitz plot due to isovector. Horizontal axes units are MeV/c^2 . (c) Discontinuity in χ^2 , depending on scan direction, along $\Gamma = 190 \text{ MeV}/c^2$.

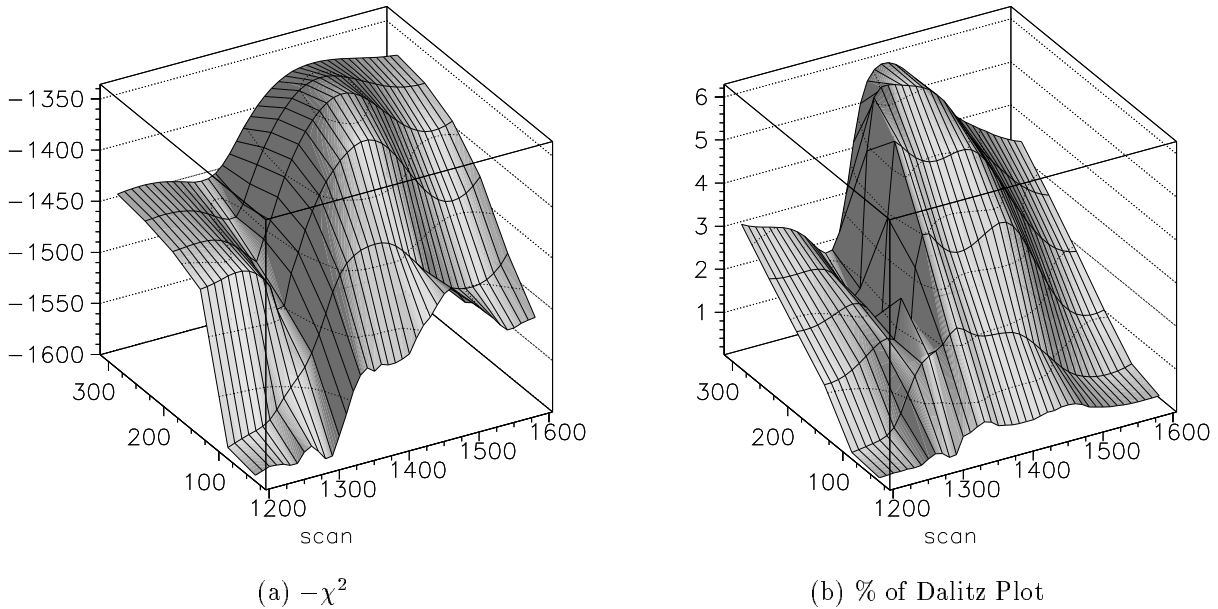


Figure 8.5: A scan over the mass and width of a second isovector, assuming $K_2^*(1430)$ but no P -wave annihilation contribution. (a) $-\chi^2$ from this analysis (b) percentage of Dalitz plot due to isovector. Horizontal axes units are MeV/c^2 .

the fit might need to jump from one solution to the other as the parameter is changed. However, if the parameter is varied slowly from a to b , this jump may not happen until the parameter goes far enough to make the barrier small. At this point, the change in χ^2 may be very dramatic. If the scan of the parameter is reversed back towards a , the new minimum may be continue to be a better solution than the previous solution. Thus it is important to be aware of sharp discontinuities in the χ^2 surface and reverse the direction of the scan of the parameter if such a discontinuity is seen, to see if the discontinuity will go away.

In fact, we see just such a discontinuity as a scan of the mass of the isovector passes through $m \sim 1480 \text{ MeV}/c^2$. This discontinuity can be seen in figures 8.4 and 8.6, where the tensor $K_2^*(1430)$ has been omitted from the fit. In all these cases, a dramatic drop in χ^2 occurs when the mass steps from 1480 to 1490, but there is no drop in χ^2 when then mass steps from 1490 to 1480.

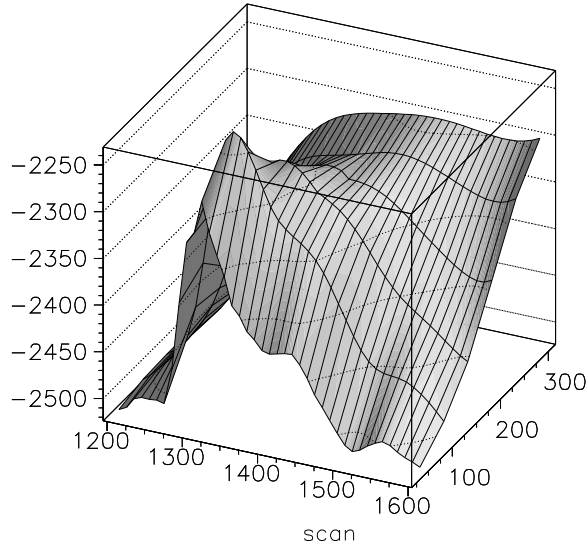
This discontinuity seems to shown in the OBELIX scan of mass too, in figure 8.2 at $m \sim 1480 \text{ MeV}/c^2$. We believe that the OBELIX scan was done sequentially with increasing mass, i.e. in steps of $\delta m = +10 \text{ MeV}/c^2$, and that they encountered the same discontinuity in the fit. If that is what they observed, then the second solution that they propose is just an artifact of the fit procedure, and there is only one solution at $m = 1290 \text{ MeV}/c^2$.

Thus to summarize, we observe an unphysical discontinuity at $m \sim 1480 \text{ MeV}/c^2$ in fits with and without P -wave annihilation, OBELIX shows a χ^2 surface with a discontinuity at the same place, and the Crystal Barrel previously declared a resonance at the same place as the discontinuity. These observations suggest that the solution at $m \sim 1480 \text{ MeV}/c^2$ is due to the same systematic effect, which is unphysical. However, there is something interesting going on at $m = 1480$ which causes the *gestalt* shift in the fit.

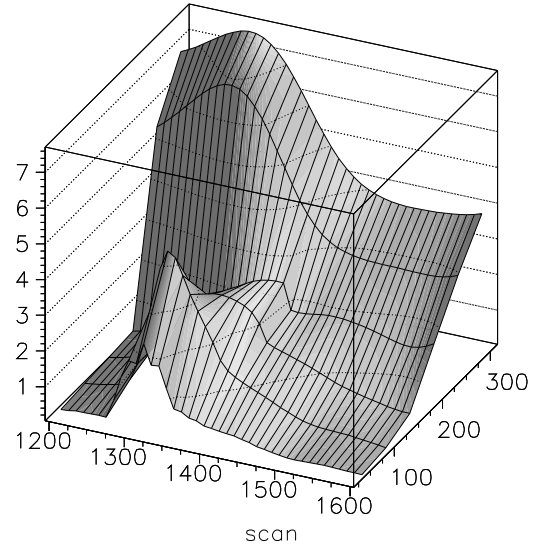
We note, perhaps as a curiosity, that the discontinuity only occurs if the $K_2^*(1430)$ is omitted from the fit; it is not seen in figures 8.3 and 8.5, where the $K_2^*(1430)$ is included in the fit.

8.3.7 3S_1 versus 1S_0

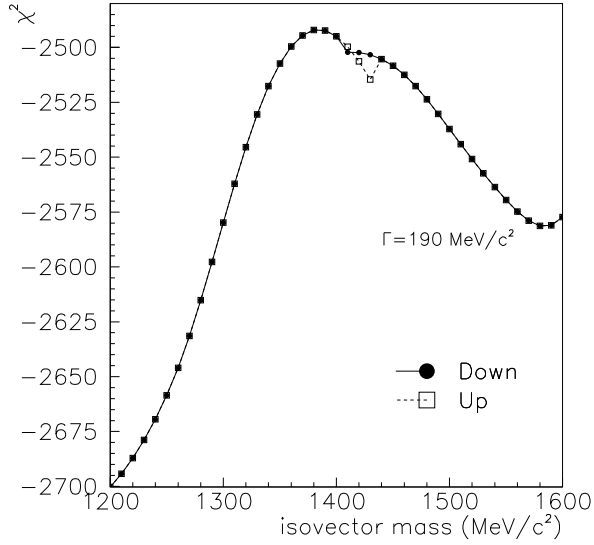
We get about 42% annihilation from 1S_0 , 27% from 3S_1 and 31% from 1P_1 and 3P_1 . The ratio of 1S_0 to 3S_1 is 1.56, in good agreement with 1.5 seen in [4]. The relative production of $K^*(892)K$ between the two initial states, 3S_1 to 1S_0 is 1.9 ± 1.0 , in agreement with 2.4 ± 0.5 from Bettini[24], 2.6 ± 0.5 from Conforto[31] and 3.0 ± 0.6 from Abele[4]. The relative production of $a_2(1320)\pi$ from 3S_1 to 1S_0 is 0.05 ± 0.02 , compared to



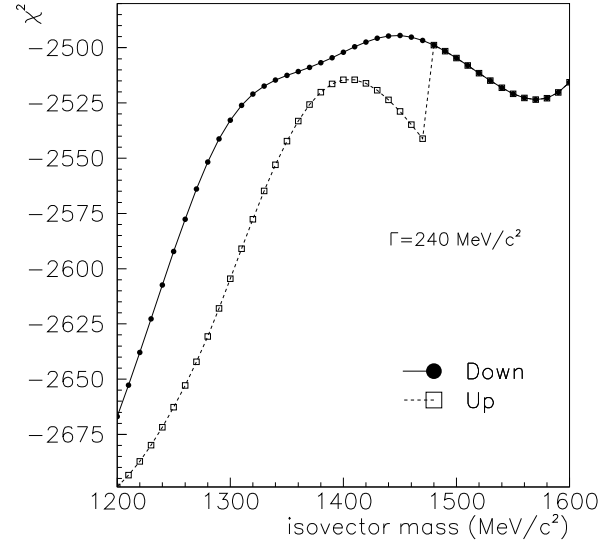
(a) $-\chi^2$



(b) % of Dalitz Plot



(c)



(d)

Figure 8.6: A scan over the mass and width of a second isovector, assuming no P -wave annihilation nor $K_2^*(1430)$ contributions. (a) $-\chi^2$ from this analysis (b) percentage of Dalitz plot due to isovector. Horizontal axes units are MeV/c^2 . (c,d) Discontinuity in χ^2 , depending on scan direction, along $\Gamma = 190, 240 \text{ MeV}/c^2$ respectively.

0.14 ± 0.06 (Bettini), 0.12 ± 0.05 (Conforto) and 0.24 ± 0.09 (Abele). This lower ratio is partially explained by transfer of intensity to the P -wave component, which was not used in the fits of these comparison papers. If we take the ratio of everything but 1S_0 to 1S_0 , we get 0.12 ± 0.03 .

8.3.8 $a_2(1320)$

We find

$$\text{BR}(p\bar{p} \rightarrow a_2(1320)\pi, a_2(1320) \rightarrow K\bar{K}) = (1.73 \pm 0.10_{\text{stat}} \pm 0.50_{\text{sys}}) \times 10^{-3} \quad (8.6)$$

which is higher than Bettini[24] which found $(1.24 \pm 0.19) \times 10^{-3}$, higher than Conforto[31] which found $(1.3 \pm 0.4) \times 10^{-3}$ ¹ and slightly higher than [4] which found $(1.49 \pm 0.19) \times 10^{-3}$. The statistical error given in (8.6) is simply the statistical error from fit # 202 (6%). The standard deviation among different reasonable fit hypotheses, that is $\Delta\chi^2 < +30$ from the reference fit, is 17%. When we change the parameterization of the Breit-Wigner to include additional kinematic factors (see section 7.7.1), we see the branching ratio drop by 21%. We add these last two systematic errors in quadrature to arrive at the total systematic error, which dominates the total error.

In a Crystal Barrel coupled-channel analysis of $\pi^0\pi^0\pi^0$, $\pi^0\pi^0\eta$, and $\pi^0\eta\eta$ [12], the value $\text{BR}(p\bar{p} \rightarrow a_2(1320)^0\pi^0, a_2(1320)^0 \rightarrow \pi^0\eta) = (2.05 \pm 0.40) \times 10^{-3}$ was determined. If we divide by (8.6) and by 3 because only π^0 was seen in [12], we find the ratio

$$r_1 = \frac{\text{BR}(a_2 \rightarrow K\bar{K})}{\text{BR}(a_2 \rightarrow \pi\eta)} = 0.29 \pm 0.10 \quad (8.7)$$

which agrees well with the Particle Data Group, $r_1(a_2(1320)) = 0.34 \pm 0.06$ [36]. A similar exercise can be done using the $p\bar{p} \rightarrow \pi^0\pi^0\eta$ result [11], looking only at singlet S-wave annihilation. We found in this analysis $\text{BR}(p\bar{p}(^1S_0) \rightarrow a_2(1320)^0\pi^0, a_2(1320)^0 \rightarrow \pi^0\eta) = (1.9 \pm 0.3) \times 10^{-3}$. From table 8.2 we find the value for $\text{BR}(p\bar{p}(^1S_0) \rightarrow a_2(1320)\pi, a_2(1320) \rightarrow K\bar{K})$ (with a 50% systematic uncertainty). We find the ratio (noting a hidden factor of 3 in the denominator to remove the charge dependence of [11])

$$r_2 = \frac{\text{BR}(p\bar{p}(^1S_0) \rightarrow a_2\pi, a_2 \rightarrow K\bar{K})}{\text{BR}(p\bar{p}(^1S_0) \rightarrow a_2\pi, a_2 \rightarrow \pi\eta)} = 0.26 \pm 0.13 \quad (8.8)$$

which also agrees well with the PDG.

8.3.9 The Branching ratio of $a_0(980) \rightarrow K\bar{K}$

The $K_2^*(1430)$, being a tensor resonance, has a complicated dynamical shape. In the 1S_0 initial state, it has a characteristic ‘‘W’’ shape in its angular projection of the Dalitz plot. It is the tail of each ‘‘W’’ from the charge and neutral $K_2^*(1430)$ that overlap along the $K\bar{K}$ threshold, forming an even sharper peak because of constructive interference. This interesting structure is seen in figures 7.4 and 7.6. This edge enhancement is seen in 1S_0 and 1P_1 initial states.

This threshold enhancement fits the data perfectly, obviating the need for the $a_0(980)$ which requires a more complicated coupled-channel (Flatté) description in order to get the shape correct. In fact, the χ^2 only increases by +2.87 when the $a_0(980)$ is removed, when it should increase by about +4 because four free parameters are removed. A scan of χ^2 versus the $a_0(980)$ contribution to the Dalitz plot is given in figure 8.7. Note that the change in χ^2 is very small over the range 0 to 10% of the Dalitz plot. Figure 7.12 shows the fit result also, but on a fine 60x60 grid. The edge enhancement is very well described *without* the $a_0(980)$.

The $a_0(980)$ is prominently seen in its decay to $\pi\eta$. Amsler[14] sees the characteristic cusp shape predicted by the Flatté formula with very high statistics in $\pi^0\pi^0\eta$. However, the decay into $K\bar{K}$ is not as prominent. In fact, nearly every measurement of the $K\bar{K}$ decay channel could have been contaminated in the same way by the $K_2^*(1430)$, because nearly all of them are measuring the 3-body system $K\bar{K}\pi$. A search of the literature could not find any evidence for $a_0(980) \rightarrow K\bar{K}$ without a π spectator or without a possible contribution from $I = 0$ $f_0(980) \rightarrow K\bar{K}$.

The $K_2^*(1430)$ phenomenon may explain one of the big puzzles associated with the $a_0(980)$. Cahn and Landshoff[27] note the puzzling situation that the relative branching ratio of $a_0(980)$ into $K\bar{K}$ versus into $\eta\pi$ varies by an order of magnitude, depending on whether the $a_0(980)$ was produced from $\eta(1440)$ or $f_1(1285)$.

¹The value on page 495 was corrected to be independent of charge

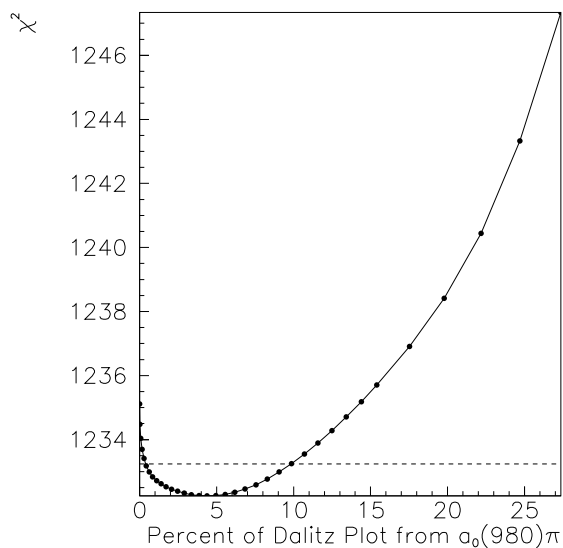


Figure 8.7: χ^2 versus the percentage contribution of $a_0(980)$ to the Dalitz plot. The dashed line is $\Delta\chi^2 = +1$ above the minimum.

If the $a_0(980)$ branching ratios are to be believed when produced in $f_1(1285)$, then they claim that the large $K\bar{K}$ threshold enhancement in $\eta(1440) \rightarrow K\bar{K}\pi$ “cannot be ascribed to the $[a_0(980)]^2$ ” Our explanation agrees with this assessment, that the “ $a_0(980)$ ” seen in the $\eta(1440)$ decays is not due to the $a_0(980)$ at all, but due to the tails of the $K_2^*(1430)$. This is the same effect seen here in this analysis in $p\bar{p} \rightarrow K\bar{K}\pi$. Because the $\eta(1440)$ has higher mass than the $f_1(1285)$, there will be more $K_2^*(1430)$ in the $\eta(1440)$ decay than in the $f_1(1285)$.

In figure 8.7, we see that the $a_0(980)$ contribution to the Dalitz plot can take on the range of 0.5 to 10%, with 4% preferred. Since 0% contribution is statistically allowed, we take the 10% contribution as the upper limit at 85% confidence level. At this point, the fit reports 2.0% from 1S_0 and 7.9% from 1P_1 . The branching ratio is then

$$\text{BR}(p\bar{p} \rightarrow a_0(980)\pi, a_0(980) \rightarrow K\bar{K}) = 0.3_{-0.3}^{+0.4} \times 10^{-3} \quad (8.9)$$

Using the branching ratio $\text{BR}(p\bar{p} \rightarrow a_0(980)\pi, a_0(980) \rightarrow \pi\eta) = (2.6 \pm 0.5) \times 10^{-3}$ [11], we find

$$\frac{\text{BR}(a_0(980) \rightarrow K\bar{K})}{\text{BR}(a_0(980) \rightarrow \pi\eta)} = 0.12_{-0.12}^{+0.15}. \quad (8.10)$$

Teige[45] calculates the $K\bar{K}$ coupling based on a fit to the Flatté line shape of the $\eta\pi$ channel measured by the E852 collaboration, and finds that the branching ratio $\text{BR}(a_0(980) \rightarrow K\bar{K}) = 0.14 \pm 0.02$. If we assume that the $\eta\pi$ and $K\bar{K}$ modes are the dominant decay modes of the $a_0(980)$, we get $\text{BR}(a_0(980) \rightarrow K\bar{K}) = 0.11_{-0.11}^{+0.10}$, in agreement with Teige.

We also attempted to see if the $K\bar{K}$ threshold enhancement could be faked by a suitable combination of the rest of the other resonances. Fit #126 without the $a_0(980)$ and without $K_2^*(1430)$ is unacceptable, with an increase of negative log-likelihood of 635.

In fits where the mass and two width parameters of the $a_0(980)$ were freed, the results did not settle on values compatible with previous analyses or with each other (see table 7.6). This is not surprising, since we have shown that the $K_2^*(1430)$ can entirely replace the $K\bar{K}$ threshold enhancement. The fit is not very sensitive to the $g_{K\bar{K}}$ coupling, so the enormous variation in the fit result is not surprising.

²The official names of the particles have changed since 1986. The $a_0(980)$ was previously the δ , the ι is now the $\eta(1440)$ and the $D(1285)$ is now the $f_1(1285)$.

Channel $p\bar{p} \rightarrow X$	1S_0		3S_1		1P_1 and 3P_1		Total BR $p\bar{p} \rightarrow X \rightarrow K\bar{K}\pi$ [10^{-3}]
	% DP	BR [10^{-4}]	% DP	BR [10^{-4}]	% DP	BR [10^{-4}]	
$K^*(890)K$	5.6	10.5 ± 1.0	10.7	20.0 ± 1.2	6.3	11.9 ± 2.7	4.2 ± 0.3
	7.4		14.2		8.4		
$K_0^*(1430)K$	2.9	5.5 ± 0.8	–	–	13.5	25.6 ± 5.0	3.1 ± 0.5
	3.9		18.5				
$K_2^*(1430)K$	2.9	5.9 ± 0.8	0.3	0.5 ± 0.4	2.0	4.0 ± 1.7	1.04 ± 0.2
	4.5		0.4		3.0		
$a_0(980)\pi$	3.9	3.1 ± 0.9	–	–	9.3	6.2 ± 2.2	0.9 ± 0.2
$a_0(1450)\pi$	1.0	0.8 ± 0.3	–	–	2.6	1.7 ± 1.1	0.25 ± 0.11
$a_2(1320)\pi$	19.1	15.4 ± 0.9	1.5	0.8 ± 0.2	1.6	1.1 ± 0.5	1.73 ± 0.10
$\rho(1450, 1700)\pi$	6.8	3.6 ± 0.7	4.5	3.6 ± 0.7	8.1	5.4 ± 2.4	1.3 ± 0.3
Coh. Total	42		27		31		–
Incoh. Total	58		32		73		–

Table 8.2: The fit results of fit # 202. The percentages of the Dalitz plot are given and the branching ratios from $p\bar{p}$ are given. When two percentages are given, the upper value is for $K^{*\pm}K^\mp$ and the lower for $K^{*0}\bar{K}^0$, in a ratio of 1:1.39 (see section 8.2.4). The total branching ratio is corrected by charge multiplicity factors (see text). The errors given are statistical only; the systematic error is estimated to be 50%.

8.4 Branching Ratios from $p\bar{p}$

To calculate the branching ratio, three values are needed. First, the total branching ratio was calculated in (6.7), being

$$\text{BR}(K_S K^\pm \pi^\pm) = (2.68 \pm 0.14) \times 10^{-3}.$$

Second, since we are interested in the branching ratios into the strong eigenstates, regardless of charge, i.e. “ $K^{\pm 0} K^{\pm 0} \pi^{\pm 0}$ ”, we require the BR scaling factors given in table 2.3, which account for unobserved final states and the CG decomposition of the weak states, K_S and K_L , into the strong states, K^0 and \bar{K}^0 . Third, we require the percentage of the Dalitz plot returned by the fit due to each channel. This is simply a defined quantity, the integral of the particular wave intensity divided by the number of events of the whole Dalitz plot. Because this ignores interferences, the sum of all contributions will be not equal to 100%.

The calculated branching ratios are summarized in table 8.2. For the channels with two charge variations i.e. $K^{*\pm}K^\mp$ and $K^{*0}K^0$, both percentages of the Dalitz plot are given, with the charged value above the neutral value. These values come from fit #202, which provided an additional hypothetical constraint on the fit, as described in section 8.2.4. From the discussion on the toy Monte Carlo fits (see table 8.1), the systematic errors are very large, estimated to be about 50%.

This large fluctuation is caused by the way amplitudes are added. The contribution of one wave can dramatically drop if another interfering wave’s contribution increases only slightly. Let us consider a single bin with 2 resonances coherently contributing to 121 events. Let A be the background amplitude, $A = 1$, and B be the signal amplitude, $B = 10$, so that the total intensity is

$$|A + B|^2 = |1 + 10|^2 = 121.$$

The number of events attributed to the background is $|A|^2 = 1$, and the number attributed to the signal is $|B|^2 = 100$. Now let us attribute 2 events to the background, so $|A|^2 = \sqrt{2}$. If the two channels were added incoherently, this additional event added to the background would take one event from the signal. But since they add coherently, we must decrease the signal amplitude to $B = 11 - \sqrt{2}$, which give $|B|^2 = 91.9$, or a loss of 9.1 events. Thus a gain of 1 event in the background gets magnified to loss of 9 events in the signal. This situation becomes even more unstable when adding 11 amplitudes (in the case of 1S_0 for example). That is why the toy MC shows such large variations in branching ratio measurements, and why we assign 50% systematic error to all branching ratio measurements from particular initial states.

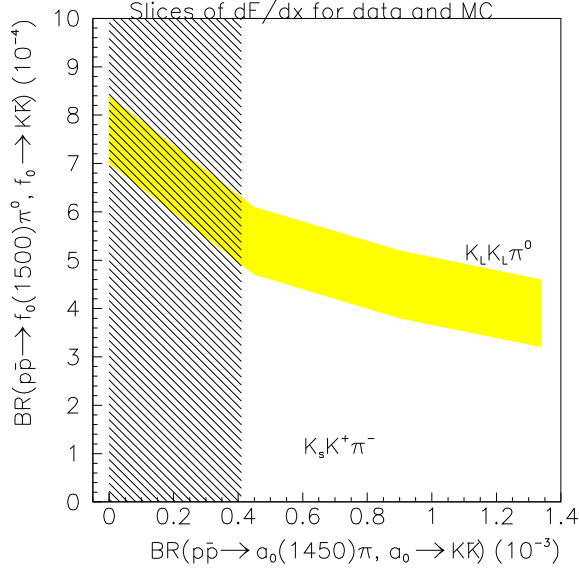


Figure 8.8: Determination of the branching ratio of $f_0(1500)$ in the reaction $p\bar{p} \rightarrow K_L K_L \pi^0$. The light shaded region was determined in [2], while the dark region was determined in the present analysis.

The total branching ratio values given in table 8.2 should be not be taken too seriously, because of massive amounts of interference. For example, the sum of all the P wave components is 73% of the Dalitz plot, but the total P wave contribution is only 31%. This means that the interference terms are greater than the direct terms! A more reasonable number would be the coupling constants, which relate directly to the interesting physics, but these have not been calculated.

8.4.1 Determination of $f_0(1500) \rightarrow K\bar{K}$

In a previous Crystal Barrel analysis, the components of $f_0(1500)$ and $a_0(1450)$ were measured in $p\bar{p} \rightarrow K_L K_L \pi^0$. Because of the similar masses and the same spin, the results were correlated. This is shown in figure 8.8. By intersecting the present result for $a_0(1450)$, the branching ratio for f_0 is constrained. We do not believe there is convincing evidence for the existence of the $a_0(1450)$, but if we include the resonance, we get a branching ratio of $(0.25 \pm 0.13) \times 10^{-3}$. Thus we take the region from zero to the upper limit of this value as the possible range for the branching ratio. From the figure, we see that the intersection region gives

$$\text{BR}(p\bar{p} \rightarrow f_0(1500)\pi^0, f_0(1500) \rightarrow K\bar{K}) = (5.0 \text{ to } 8.4) \times 10^{-4} \quad (8.11)$$

With $\text{BR}(p\bar{p} \rightarrow f_0(1500)\pi^0, f_0(1500) \rightarrow \pi^0\pi^0) = (8.1 \pm 2.8) \times 10^{-4}$ from Ref. [13], we calculate

$$r = \frac{\text{BR}(f_0(1500) \rightarrow K\bar{K})}{3 \cdot \text{BR}(f_0(1500) \rightarrow \pi^0\pi^0)} \frac{\rho(f_0(1500) \rightarrow \pi^0\pi^0)}{\rho(f_0(1500) \rightarrow K\bar{K})} = 0.27 \text{ to } 0.45 \quad (8.12)$$

SU(3) flavor symmetry predicts a coupling ratio $r = 1/3$ for a $(u\bar{u} + d\bar{d})$ state and $r = \infty$ for a $s\bar{s}$ state. This highly favors a $(u\bar{u} + d\bar{d})$ interpretation over a $s\bar{s}$ interpretation, the same conclusion of Abele[4]. Because the 0^{++} nonet already appears to have the $(u\bar{u} + d\bar{d})$ state occupied by the $f_0(1370)$, the $f_0(1500)$ is supernumerary, making it a likely glueball or other non- $q\bar{q}$ state.

8.4.2 Absence of 3P_2

The fit does not apparently want any annihilation from the 3P_2 initial state. When it is added to the reference fit (# 81), the negative log-likelihood only drops by 10 units. This is not significant after the addition of 13 extra parameters. It takes on $(4 \pm 2)\%$ of the total Dalitz plot, where the 1P_1 and 3P_1 contribution is 21.9%,

for a total of about 26%. In fit #142, which imposes charge symmetry for $K\pi$, the contribution from 3P_2 is $(2 \pm 2)\%$, consistent with zero, and the contribution from 1P_1 is about 33%.

This is in marked contrast to the OBELIX analysis[23], which found that 3P_2 accounted for $(5 \pm 1)\%$ of the Dalitz plot while 1P_1 accounted for only $(8 \pm 1)\%$.

If the 1P_1 initial state is removed from the fit and the 3P_2 is kept (fit #143), then the negative log-likelihood rises by 172 compared to fit # 142 which used both P -waves. Thus the fit clearly demands 1P_1 and does not demand any 3P_2 .

8.5 Comparison to earlier Crystal Barrel Fit

The $K_L K^\pm \pi^\mp$ Dalitz plot should be very similar to this Dalitz plot. In [4], only S -wave annihilation was used and the $K_2^*(1430)$ was not used. This hypothesis was used in fit #87, with very poor results. The χ^2 increased by 622 with $980 - 62$ degrees of freedom. The χ^2 plot, showing areas of bad fit, is given in figure 7.13. Adding only P -wave or only $K_2^*(1430)$ to the fit improves things (Fits #80 and #84), but the χ^2 is still poor, with increases in +194 and +304 respectively. The data clearly demands both at least 1P_1 or 3P_1 initial state annihilation and the $K_2^*(1430)$ resonance.

Chapter 9

Conclusion

We summarize the results of the analysis of the $K_S K^\pm \pi^\mp$ Dalitz plot.

1. The $K_S K^\pm \pi^\pm$ Dalitz plot requires the following resonances to minimally fit the data: $K^*(892)$, $K_2^*(1430)$, $K_0^*(1430)$, $a_2(1320)$, and $\rho(1650)$, originating from 1S_0 , 3S_1 , 1P_1 and 3P_1 initial states. There is some additional evidence for two ρ resonances, $\rho(1450)$ and $\rho(1700)$, which would replace the $\rho(1650)$. There is minimal evidence for the $a_0(1450)$. There is some evidence for the $K^*(1410)$. There is no evidence for the $a_0(980)$ nor for the $a_2(1620)$.
2. The $K_2^*(1430)K$ wave is an important part of $p\bar{p}$ annihilation at rest, and it creates the $K\bar{K}$ edge enhancement.
3. The decays of the $f_0(1500)$ are not consistent with an $s\bar{s}$ interpretation, and thus it is not the $s\bar{s}$ member of the $0^{++} q\bar{q}$ nonet.
4. The $a_0(980)$ branching ratio into $K\bar{K}$ is consistent with zero, but is also consistent with that determined by the E852 collaboration based on the line shape of the $\eta\pi$ decay channel.

We are not able to accurately determine the branching ratios of many of the resonances from different initial states, because there are not enough constraints in the fits. To determine the branching ratios more accurately, a coupled channel analysis using other reactions not included in this thesis (*e.g.* $p\bar{p} \rightarrow K_S K_S \pi^0$) must be done. This will be done by the author and other collaborators in the near future.

Chapter 10

Appendix Kinematic Fitting

10.0.1 Introduction

A new kinematic fitter was written for the hypothesis, $p\bar{p} \rightarrow K^\pm \pi^\mp K_S$, because the standard Crystal Barrel software (CBKFIT) does not support this hypothesis. Because it worked very well and is easier to use than CBKFIT, we used it also on this analysis. The software is object-oriented, making it easy to add new constraints. Currently, the constraints are three-momentum conservation and mass conservation at the decay vertices. Any event with 6 or less final state particles can be fitted. (This restraint is imposed by CLHEP, but could be easier expanded if necessary).

There are many new C++ classes.

1. **KinFit** - This is the master class container of the hypotheses. It contains a list of hypotheses.
2. **KinFitHypothesis** - This contains the hypothesis and is a container for the permutations. The fit generates a list of good permutations for each hypothesis for each event. This list is sorted in order of χ^2 .
3. **KinFitPermutation** - This contains the permutation of particles. After the fit is done, only valid permutations with valid χ^2 are kept.
4. **KinFitParticle** - A subclass of Particle, contain information about the pulls and also some mechanism for locking the particles when making combinations. These are made in KinFitHypothesis for use in KinFitPermutation. The final answer is in terms of these.

10.0.2 KinFitHypothesis

The Hypothesis class generates the permutations. The problem is to assign the n measured tracks/PEDs to the n final state particles in the predefined hypothesis.

The user initializes the hypothesis with a KinFitParticle, which is a description of the initial state and the immediate daughter particles. Each daughter particle can have further daughters, forming a hierarchy. For instance, the initial state is a $p\bar{p}$ pseudo-particle, with K^\pm , π^\mp , and K_S as the daughters. The K_S is defined with π^+, π^- as its two daughters.

First the given measured tracks/PEDs are assigned to 3 lists: charged “+”, charged “-” and neutral. The final state particles in the hypothesis are symbolically linked to the corresponding lists. The next higher resonances are created using existing resonances; the new resonances are then added to the database to be used for the next iteration of resonance building. Resonances can require certain things about their daughters. For instance, a K_S can require that the two daughter pions came from the same vertex.

When all resonances are built (ending with the $p\bar{p}$ root particle), each instance in the root particle list is copied to a KinFitPermutation. Each permutation is then fitted, and those permutations that fail the fit are deleted. At the end, the remaining permutations are sorted in increasing χ^2 .

10.0.3 KinFitPermutation, description of fitting algorithm

The user submits a selected hypothesis, and the software returns a list of possible permutations that minimally satisfy it. If the list is zero, then no permutation worked. The minimum condition of satisfaction is

that the total $\chi^2/N < 5.0$. The list is ordered, so the user typically only examines the first element of the list. The user can then extract the new fitted values of 4-momenta and the pulls from the permutation.

There are three momentum constraints ($\vec{p}_{\text{tot}} = 0$) and m mass constraints, which are explicitly

$$f_i^{\text{momentum}} = \sum_{j=1}^n P_i^j \{i = x, y, z\} \quad (10.1)$$

$$f_k^{\text{mass}} = \frac{(m(\text{theory})_k^2 - m(\text{exp})_k^2)}{m(\text{theory})} \{k = 1..m\} \quad (10.2)$$

This gives a total of

$$c = 3 + m$$

constraints. The nominal phase space fit contains only one resonance (one mass constraint), the initial state ($p\bar{p}$), so has $3 + 1 = 4$ constraints as expected.

The measured values of momenta are written as a vector

$$\eta = (p_x^1, p_y^1, p_z^1, p_x^2, p_y^2, p_z^2, \dots, p_z^n)$$

And the $3n$ by $3n$ block-diagonal symmetric error matrix is written as,

$$\mathcal{G}_\eta^{-1} = \begin{pmatrix} S_1 & & & \\ & S_2 & & \\ & & \ddots & \\ & & & S_n \end{pmatrix}$$

where the individual tracks have error matrices,

$$S_i = \begin{pmatrix} \sigma_{xx} & \sigma_{xy} & \sigma_{xz} \\ \sigma_{yx} & \sigma_{yy} & \sigma_{yz} \\ \sigma_{zx} & \sigma_{zy} & \sigma_{zz} \end{pmatrix}.$$

We then calculate the derivative matrix,

$$\mathcal{B} = \begin{pmatrix} \frac{\partial f_1}{\partial \eta_1} & \dots & \frac{\partial f_1}{\partial \eta_{3n}} \\ \vdots & \ddots & \vdots \\ \frac{\partial f_c}{\partial \eta_1} & \dots & \frac{\partial f_c}{\partial \eta_{3n}} \end{pmatrix}.$$

In this case,

$$\mathcal{B} = \begin{pmatrix} \begin{pmatrix} 1 & 0 & 0 \\ 0 & 1 & 0 \\ 0 & 0 & 1 \end{pmatrix} & \begin{pmatrix} 1 & 0 & 0 \\ 0 & 1 & 0 \\ 0 & 0 & 1 \end{pmatrix} & \dots & \begin{pmatrix} 1 & 0 & 0 \\ 0 & 1 & 0 \\ 0 & 0 & 1 \end{pmatrix} \\ (\vec{F}_1^1)^T & (\vec{F}_1^2)^T & \dots & (\vec{F}_1^n)^T \\ (\vec{F}_2^1)^T & (\vec{F}_2^2)^T & \dots & (\vec{F}_2^n)^T \\ \vdots & & & \\ (\vec{F}_m^1)^T & (\vec{F}_m^2)^T & \dots & (\vec{F}_m^n)^T \end{pmatrix}$$

where

$$\vec{F}_j^i = \frac{E_j \cdot \vec{\beta}^i - \vec{p}_j}{m(\text{theory})_j}$$

where E_j, \vec{p}_j, m_j is the energy/momentum/mass of the j^{th} resonances, and $\vec{\beta}^i$ is the velocity of the i^{th} track/PED.

We calculate the covariance matrix, in the constraint basis,

$$\mathcal{G}_\mathcal{B} = (\mathcal{B}\mathcal{G}_\eta^{-1}\mathcal{B}^T)^{-1}$$

and then the improvements to the measured values,

$$\delta\eta = \mathcal{G}_\eta^{-1} \mathcal{B}^T \mathcal{G}_B \mathbf{f}$$

where are iteratively subtracted from the measured values

$$\eta := \eta - \delta\eta$$

The fit desires to make $\mathbf{f} = \mathbf{0}$, so on each calculation,

$$d^2 = \mathbf{f}^T \mathcal{G}_B \mathbf{f}$$

is calculated, and the iterations stop if any of the following conditions is met:

1. The value of d^2 is sufficiently close to zero, which is a successful fit.
2. The value of d^2 is higher than an allowed maximum, and the fit fails.
3. The number of iterations is too high, so the fit fails.
4. An internal error happens, such as inversion of a singular matrix, where the fit of course fails.

At the end of the fit, the χ^2 of the change in the measurements ($\epsilon = \eta - \eta_0$) is calculated,

$$\chi^2 = (\mathcal{B}\epsilon)^T \mathcal{G}_B (\mathcal{B}\epsilon)$$

where the degrees of freedom of the fit are simply the number of constraints, since there are no free parameters,

$$N_{\text{dof}} = 3 + m$$

The reduced χ^2 value is required to be

$$\frac{\chi^2}{N_{\text{dof}}} < 5.0$$

or else the permutation is deleted from the hypothesis.

10.0.4 Final Errors and pulls

In this notation, η = estimates of best values, \mathbf{y} = original data values, \mathbf{x} = parameters of fit. The normal kinematic fit has no free parameters, so \mathbf{x} is not used.

The final errors are calculated using this formula

$$\mathcal{G}_\eta^{-1} = \mathcal{G}_\mathbf{y}^{-1} - \mathcal{G}_\mathbf{y}^{-1} B^T \mathcal{G}_B B \mathcal{G}_\mathbf{y}^{-1} + \mathcal{G}_\mathbf{y}^{-1} B^T \mathcal{G}_B A (A^T \mathcal{G}_B A)^{-1} A^T \mathcal{G}_B B \mathcal{G}_\mathbf{y}^{-1}$$

Note again, that if there are no free parameters, then $A = 0$ as well as $\mathbf{x} = 0$. If a special fit is added, for example the neutral decay position of the $K_S \rightarrow \pi^0 \pi^0$ then this will need to be used.

A pull is a measure of the displacement of the measured values to the fitted values. They are constructed so that a valid distribution of pulls will form a normal distribution with width 1 and mean 0. A pull of the observable λ is defined as

$$P = \frac{\lambda_f - \lambda_i}{\sqrt{\sigma(\lambda_i)^2 - \sigma(\lambda_f)^2}},$$

where i denotes value before fitting and f denotes value after fitting. The $\sigma(\lambda_f)$ comes from \mathcal{G}_η^{-1} , while the $\sigma(\lambda_i)$ are estimates supplied to the software. Note that the denominator really contains a subtraction and not an addition as might naively be thought. This is because the denominator describes just the statistical uncertainty of the measurement, which can be thought of the difference between the total measured uncertainty and the systematically fitted uncertainty. This also implies that the fitted errors must be always smaller (usually much smaller) than the original errors.

The pulls are a very sensitive measure of the goodness of the fit. If the mean of the pull distribution is not zero, then the data is biased for some reason. This bias could be background, or it could be a detector bias. For example the z -position of the neutral vertex shifts the distribution of the pull of θ_{PED} . If the width is not one, then usually the initial errors are not as good as they could have been. It is usual practice to globally scale the measured initial errors by a factor of order unity in order to force the pull distributions to have a width of one.

10.0.5 Conversion of Rectangular to Helix Parameters

Because the internal calculations are done in rectangular coordinate, the measured parameters of the tracks must be converted from helical coordinates. The conversion of the error matrices is a little more work. To calculate the pulls in the original basis, the internal values need to be converted back too.

$$\begin{aligned} P_{\perp} &= 1/\alpha \\ \vec{P} &= P_{\perp}(\cos \psi, \sin \psi, \tan \lambda) \end{aligned} \quad (10.3)$$

$$P_{\perp} = \sqrt{P_x^2 + P_y^2} \quad (10.4)$$

$$\alpha = 1/P_{\perp} \quad (10.5)$$

$$\psi = \text{ATAN2}(P_y, P_x) \quad (10.6)$$

$$\tan \lambda = P_z/P_{\perp} \quad (10.7)$$

$$\frac{\partial \vec{P}}{\partial \alpha} = P_{\perp}^2(-\cos \psi, -\sin \psi, \tan \lambda) \quad (10.8)$$

$$\frac{\partial \vec{P}}{\partial \tan \lambda} = (0, 0, P_{\perp}) \quad (10.9)$$

$$\frac{\partial \vec{P}}{\partial \psi} = P_{\perp}(-\sin \psi, \cos \psi, 0) \quad (10.10)$$

$$\frac{\partial \alpha}{\partial \vec{P}} = \frac{1}{P_{\perp}^3}(-P_x, -P_y, 0) \quad (10.11)$$

$$\frac{\partial \tan \lambda}{\partial \vec{P}} = \frac{1}{P_{\perp}^3}(-P_x P_z, -P_y P_z, P_{\perp}^2) \quad (10.12)$$

$$\frac{\partial \psi}{\partial \vec{P}} = \frac{1}{P_{\perp}^2}(-P_y, P_x, 0) \quad (10.13)$$

10.0.6 PED parameters to Rectangular

Because the internal calculations are done in rectangular coordinate, the measured parameters of the PEDs must be converted from spherical coordinates. The conversion of the error matrices is a little more work. To calculate the pulls in the original basis, the internal values need to be converted back too.

$$\vec{P} = (\sqrt{E})^2(\cos \phi \sin \theta, \sin \phi \sin \theta, \cos \theta) \quad (10.14)$$

$$P_{\perp} = \sqrt{P_x^2 + P_y^2} \quad (10.15)$$

$$P = \sqrt{P_x^2 + P_y^2 + P_z^2} \quad (10.16)$$

$$\phi = \text{ATAN2}(P_y, P_x) \quad (10.17)$$

$$\theta = \arccos(P_z/P) \quad (10.18)$$

$$\sqrt{E} = \sqrt{P}$$

$$\frac{\partial \vec{P}}{\partial \phi} = (\sqrt{E})^2(-\sin \phi \sin \theta, \cos \phi \sin \theta, 0) \quad (10.19)$$

$$\frac{\partial \vec{P}}{\partial \theta} = (\sqrt{E})^2 (\cos \phi \cos \theta, \sin \phi \cos \theta, -\sin \theta) \quad (10.20)$$

$$\frac{\partial \vec{P}}{\partial \sqrt{e}} = 2(\sqrt{E}) (\cos \phi \sin \theta, \sin \phi \sin \theta, \cos \theta)$$

$$\frac{\partial \phi}{\partial \vec{P}} = \frac{1}{P_{\perp}^2} (-P_y, P_x, 0) \quad (10.21)$$

$$\frac{\partial \theta}{\partial \vec{P}} = \frac{1}{P^2} \left(\frac{P_x P_z}{P_{\perp}}, \frac{P_y P_z}{P_{\perp}}, -P_{\perp} \right) \quad (10.22)$$

$$\frac{\partial \sqrt{E}}{\partial \vec{P}} = \frac{1}{2P^{3/2}} (P_x, P_y, P_z) \quad (10.23)$$

Chapter 11

Appendix Steering Cards

```
WRIT 4  
FZIN 'XT'  
FZOU 'XT'  
CHAM 'TRAK' 'RAWS' 'GPWC' 'PATT' 'CIRC' 'HELX'  
XTAL 'TRAK' 'DECF' 'DECL' 'ALCE' 'CLST' 'PEDS' 'PDRG'  
GLOB 'TRAK' 'MTCH'  
BANK 'GLOB'
```

Table 11.1: First pass reconstruction steering cards for CBOFF, Fortran Unit 99

```

WRIT 4
FZIN 'XT'
FZOU 'XT'
CHAM 'NONE'
XTAL 'NONE'
GLOB 'NONE'
BANK 'GLOB'

```

Table 11.2: Second pass steering cards for energy and momentum selection for CBOFF, Fortran Unit 99

```

WRIT 4
FZIN 'XT'
CHAM 'TRAK' 'RTRK' 'RAWS' 'GVTX' 'PATT' 'CIRC' 'HELX' 'VERT'
XTAL 'TRAK' 'RTRK' 'DECF' 'DECL' 'ALCE' 'CLST' 'PEDS' 'PDRG'
GLOB 'TRAK' 'RTRK' 'MTCH'

VERT 3
VFIT 2
VHER 0.8

```

Table 11.3: Third pass steering cards for vertex fitting, with CBOFF unit 99 at top and Locator unit 81 at bottom

```

WRIT 4
FZIN 'XT'
CHAM 'NONE'
XTAL 'NONE'
GLOB 'NONE'

```

Table 11.4: Fourth pass steering cards for kinematic fitting for CBOFF unit 99

Chapter 12

Appendix Data

A recordable Compact Disc is enclosed. The data format is the standard ISO-9660 format, which is readable on every popular computer of 1998. Hopefully this standard will be around for the next hundred years. The lifetime of recordable CDs is estimated to be at least 100 years based on accelerated aging tests. The CDROM contains the following data. Consult the `README.TXT` file for the latest information.

1. The thesis in postscript format
2. The thesis \LaTeX and `.eps` source files.
3. Source code for `AWP`.
4. Compiled version for Solaris 2.5.
5. Example steering files.
6. Histograms, in 30x30 binning and 60x60 binning.
 - (a) All Data
 - (b) $K_S K^+ \pi^-$ Data
 - (c) $K_S K^- \pi^+$ Data
 - (d) All Monte Carlo Data
 - (e) $K_S K^+ \pi^-$ Monte Carlo
 - (f) $K_S K^- \pi^+$ Monte Carlo
7. All Data, event by event, with the following format (ASCII text). Each event is written as 25 numeric fields, each separated by one character of white space (0x20) and followed by the newline character (0x0A) at the end. Integer fields are formed from the digits '0' (0x30) to '9' (0x39) and an optional minus sign '-' (0x2d). Real fields are formed from the digits '0' (0x30) to '9' (0x39), a period '.' (0x2e), signs '+' (0x2b) or '-' (0x2d) and an optional 'e' (0x65) for floating point notation. Examples of floating point are

```
1.1e+06
9.16515
-1.3e-12
```

Field	Real/Integer	Description
0	I	Run Number
1	I	Event Number
2	R	χ^2 of Kinematic Fit to $K_S K^\pm \pi^\pm$
3	R	$m^2(K_S \pi^\pm)$
4	R	$m^2(\pi^\mp K^\pm)$
5	R	$m^2(K^\pm K_S)$
6	R	x position of V0
7	R	y position of V0
8	R	z position of V0
9	R	x position of V1
10	R	y position of V1
11	R	z position of V1
12	R	p_x of kaon at V0
13	R	p_y of kaon at V0
14	R	p_z of kaon at V0
15	R	p_x of pion at V0
16	R	p_y of pion at V0
17	R	p_z of pion at V0
18	R	p_x of pion at V1 (+ charge)
19	R	p_y of pion at V1 (+ charge)
20	R	p_z of pion at V1 (+ charge)
21	R	p_x of pion at V1 (- charge)
22	R	p_y of pion at V1 (- charge)
23	R	p_z of pion at V1 (- charge)
24	I	Charge of kaon

Bibliography

- [1] A. Abele et al. Further analysis of $\bar{p}p \rightarrow 3\pi^0, \eta\eta\pi^0$ and $\eta\pi^0\pi^0$ at rest. *Nuclear Physics*, A609:562–584, 1996.
- [2] A. Abele et al. Observation of $f_0(1500)$ decay into $K_L K_L$. *Physics Letters*, B385:425, 1996.
- [3] A. Abele et al. Study of the $\pi^0\pi^0\eta'$ final state in antiproton proton annihilations at rest. *Physics Letters*, B404:179, 1997.
- [4] A. Abele et al. Antiproton-proton annihilation at rest into $K_L K^\pm \pi^\mp$. *Physics Review*, D57:3860, 1998.
- [5] A. Abele et al. Exotic $\eta\pi$ state in antiproton-deuterium annihilation at rest into $\pi^-\pi^0\eta$ spectator. *Physics Letters*, B423:175, 1998.
- [6] A.J.Noble. The release of CBGEANT 5.00. Technical Report CBNote 264, Crystal Barrel Collaboration, 1994.
- [7] E. Aker et al. Observation of a 2^{++} resonance at 1515 MeV in proton antiproton annihilations into $\pi^0\pi^0\pi^0$. *Physics Letters*, B260:249, 1991.
- [8] E. Aker et al. The Crystal Barrel detector at LEAR. *Nuclear Instruments and Methods*, A321:69, 1992. CERN-PPE/92-126.
- [9] C. Amsler and F. Close. Is $f_0(1500)$ a scalar glueball? *Physics Review*, D53:295, 1996.
- [10] C. Amsler et al. Proton-antiproton annihilations into $\eta\eta\pi^0$ - observation of a scalar resonance decaying into $\eta\eta$. *Physics Letters*, B291:347, 1992. CERN-PPE/92-114.
- [11] C. Amsler et al. Observation of a new $I^G J^{PC} = 1^- 0^{++}$ resonance at 1450 MeV. *Physics Letters*, B333:277, 1994.
- [12] C. Amsler et al. Coupled channel analysis of antiproton proton annihilation into $\pi^0\pi^0\pi^0$, $\pi^0\eta\eta$ and $\pi^0\pi^0\eta$. *Physics Letters*, B355:425, 1995.
- [13] C. Amsler et al. A high-statistics study of $f_0(1500)$ decay into $\pi^0\pi^0$. *Physics Letters*, B342:433, 1995.
- [14] C. Amsler et al. High statistics study of the $f_0(1500)$ decay into $\eta\eta$. *Physics Letters*, B353:571, 1995.
- [15] C. Amsler and F. Myhrer. Low energy antiproton physics. *Annu. Rev. Nucl. Part. Sci.*, 41:219–267, 1991.
- [16] R. Armenteros et al. Experimental results on the annihilation $p\bar{p} \rightarrow K\bar{K}\pi$ at rest; K^* production. *Physics Letters*, 17:170, 1965.
- [17] G. Ascoli et al. Partial-wave analysis of the deck amplitude for $\pi N \rightarrow \pi\pi\pi N^*$. *Physics Review*, D8:3894, 1973.
- [18] Aston et al. A study of $K^-\pi^+\pi^+$ scattering in the reaction $K^-p \rightarrow K^-\pi^+n$ at 11 GeV/c. *Nuclear Physics*, B296:493–526, 1988.
- [19] A.M. Badalyan et al. Resonances in coupled channels in nuclear and particle physics. *Physics Reports*, 82(2):31–177, 1982.

- [20] G.S. Bali et al. a comprehensive lattice study of SU(3) glueballs. *Physics Letters*, B309:378, 1993.
- [21] Barash. Antiproton annihilation in hydrogen at rest. I. reaction $p\bar{p}\rightarrow K\bar{K}\pi$. *Physics Review*, 139B:1659, 1965.
- [22] C. J. Batty. S- and P-state annihilation in anti-p p interactions at rest. *Nuclear Physics*, A601:425–444, 1996.
- [23] A. Bertin et al. Study of the isovector scalar mesons in the channel $p\bar{p}\rightarrow K^\pm K_S\pi^\mp$ at rest with initial angular momentum state selection. *Physics Letters*, B434:180–188, 1998.
- [24] A. Bettini et al. The annihilation at rest $\bar{n}n\rightarrow K\bar{K}\pi$. *Nuovo Cimento*, 63A:1199, 1969.
- [25] Boutemeur. unknown. In Suk urk Chung, editor, *Glueballs, Hybrids, and Exotic Hadrons: Proceedings*, page 185. American Institute of Physics, Aug 29 - Sep 1 1989. QCD161:B58:1988.
- [26] Rene Brun, F. Bruyant, M. Maire, A.C. McPherson, and P. Zanmarini. GEANT. Technical Report DD/EE/81-1, CERN Program Library, 1987.
- [27] R.N. Cahn and P.V. Landshoff. Mystery of the $\delta(980)$ [ed: now called $a_0(980)$]. *Nuclear Physics*, B266:451–467, 1986.
- [28] S.U Chung et al. Partial wave analysis in the K -matrix formalism. *Ann. Physik*, 4:404, 1995.
- [29] W. Cleland et al. Resonance production in the reaction $\pi^\pm p \rightarrow K_S K^\pm p$ at 30 GeV/c and 50 GeV/c. *Nuclear Physics*, B208:228, 1982.
- [30] Frank Close. *An Introduction to Quarks and Partons*. Academic, New York, 1979.
- [31] B. Conforto and other. Experimental results on the $(K\bar{K})$ and (Kp) systems as observed in the annihilations $p\bar{p}\rightarrow K\bar{K}pi$ at rest. *Nuclear Physics*, B3:469–503, 1967.
- [32] T. DeGrand et al. Masses and other parameters of the light hadrons. *Physics Review*, D12:2060, 1975.
- [33] A. Donacchie and Clegg. The decays of the ρ' and ω' mesons. *Zeitschrift für Physik*, C51:689, 1991.
- [34] V. Filippini et al. Covariant spin tensors in meson spectroscopy. *Physics Review*, D51:2247, 1995.
- [35] S.M. Flatteé. Coupled-channel analysis of the $\pi\eta$ and $K\bar{K}$ systems near $K\bar{K}$ threshold. *Physics Letters*, B63:224, 1976.
- [36] Particle Data Group. Review of particle physics. *European Physical Journal*, C3:1–794, 1998.
- [37] J.D. Hansen et al. Formalism and assumptions involved in partial wave analysis of three - meson systems. *Nuclear Physics*, B81:403, 1974.
- [38] N. Isgur and G. Karl. P wave baryons in the quark model. *Physics Review*, D18:4187, 1978.
- [39] N. Isgur and G. Karl. Positive parity excited baryons in a quark model with hyperfine interactions. *Physics Review*, D19:2653, 1979.
- [40] Fred James. Minuit function minimization and error analysis reference manual. Technical report, CERN Program Library, 1992. D506 V92.1.
- [41] E. Klempt. The scalar meson nonet and the glueball ground state. *Nuclear Physics*, A629:131–140, 1998.
- [42] Mark Lakata. A new multi-vertex fitter and updated vertex-locater information. Technical report, Crystal Barrel, 1995. CB Note 285.
- [43] J.C. Sexton et al. numerical evidence for the observation of a scalar glueball. *Physics Review Letters*, 75:4563, 1995.
- [44] Stefan Spanier. Crystal barrel results on two body decays of the scalar glueball. In S. Narison, editor, *QCD96, Proceedings of the Conference*, volume 54A, page 362, France, 1997. Nucl. Phys B. Proc. Suppl.

- [45] S. Teige et al. Properties of the $a_0(980)$ meson. *hep-ex*, 960817:1, 1996.
- [46] G. Usai. Study of the isovector scalar mesons in the channel $p\bar{p} \rightarrow K^\pm K_S \pi^\mp$ at three hydrogen target densities. In Suh-Urk Chung and Hans J. Willutzki, editors, *Hadron Spectroscopy, 7th International Conference*, page 108. OBELIX collaboration, American Institute of Physics, August 1997.
- [47] Frank von Hippel and C. Quigg. Centrifugal-barrier effects in resonance partial decay widths, shape, and production amplitudes. *Physics Review*, D5:624–638, 1972.
- [48] Charles Zemach. Use of angular-momentum tensors. *Physics Review*, 140B:97–109, 1965.